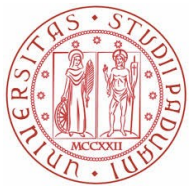

UNIVERSITÀ DEGLI STUDI DI PADOVA

DIPARTIMENTO DI SCIENZE CHIMICHE

CORSO DI LAUREA MAGISTRALE IN CHIMICA INDUSTRIALE

TESI DI LAUREA MAGISTRALE

ENERGY CONVERSION AND STORAGE BY MEANS OF CO_2 AND H_2O MIXTURES: DEVELOPMENT AND OPTIMIZATION OF REVERSIBLE SOLID OXIDE CELLS (r-SOCs)

Relatore: Chiar.ma Prof. Antonella Glisenti

Controrelatore: Chiar.mo Prof. Moreno Meneghetti

Laureando: Matilde Castagna

Matricola 2089680

ANNO ACCADEMICO 2023/2024

INDEX

ABBREVIATIONS

Symbol	Meaning	Common Units
FC	Fuel Cell	-
SOFCs	Solid Oxide Fuel Cells	-
PEMFC	Proton Exchanger Membrane Fuel Cell	-
PAFC	Phosphoric Acid Fuel Cell	-
AFC	Alkaline Fuel Cell	-
DMFC	Direct Methanol Fuel Cell	-
MCFC	Molten Carbonates Fuel Cell	
SOECs	Solid Oxide Electrolyser Cells	-
AEL	Alkaline Electrolyser	-
PEMEL	Proton Exchange Membrane Electrolyser	-
AEMEL	Anion Exchange Membrane Electrolyser	-
r-SOC	Reverse Solid Oxide Cell	-
TPB	Triple Phase Boundary	-
LHV	Lower Heating Value	MJ/kg
HHV	High Heating Value	MJ/kg
CAGR	Compound Annual Growth Rate	-
OER	Oxygen Evolution Reaction	-
RWGS	Reverse Water Gas Shift Reaction	-
GHG	Greenhouse Gas Emissions	-
OCV	Open Circuit Voltage	V
sccm	Standard Cubic Centimetres per Minute	Cm^3/min
TEC	Thermal Expansion Coefficient	$°C^{-1}$
ASR	Area-Specific Resistance	$\Omega \cdot cm^2$
TPB	Triple Phase Boundary	-
SAS	Specific Surface Area	Cm^2/g
PSD	Pore Size Distribution	-

ABSTRACT

The reduction of pollutants and the use of renewable energy sources are central themes in the historical period we are currently living through. However, some of these sources, such as solar and wind, are intermittent and therefore not always available. In this context, the development of methodologies for converting CO_2 and H_2O into fuels, such as H_2 and hydrocarbons, could be a smart methodology for energy storage and transportation. The possibility to convert carbon dioxide into fuels, helps in reducing the impact of many industrial activities. Reversible solid oxide cells are devices capable of operating both as Fuel Cells and as Electrolytic Cells. They would drive the co-electrolysis of CO_2 and H_2O in syngas ($CO+H_2$) while working in Electrolysis mode, and then lead the conversion of the chemical energy into electrical energy by operating in SOFC mode, a particular sub-group of Fuel Cell that will be explained in a dedicated chapter (*Chapter 1*). The design, synthesis, and characterization of electrode materials capable of operating in a reversible cell is necessary from this perspective (*Chapter 4*). However, the reversibility of the material requires the development of highly performing electrode materials in both oxidizing and reducing environments. This thesis focuses on the development and optimization of robust and sustainable electrodes and the creation of a reversible device. As an electrode, a Fe-doped Strontium Molybdate-based perovskite is used comparing two different stoichiometries (Sr_2FeMoO_6 and $Sr_2Fe_{1.5}Mo_{0.5}O_6$); this is a material that in recent years has gained much interest, as it can be tuneable according to the material's needs and required properties. The synthesis is carried out through the Pechini process (a water-based wet chemistry method) to achieve high purity and controlled insertion of cations into the perovskite structure. The obtained products are characterized using X-Ray Diffraction (XRD), X-Ray Photoelectron Spectroscopy (XPS), Scanning Electron Microscopy (SEM), Energy Dispersive X-Ray Spectroscopy (EDX), BET specific surface area, Temperature Programmed Reduction (TPR) techniques. To evaluate their stability and reactivity under the operating conditions, thermocatalytic tests have been carried out in a quartz reactor (equipped with a Gas Chromatograph - GC) to test the behaviour in the Reverse Water Gas

Shift (RWGS) reaction (*Chapter 5*). Finally, the Solid Oxide Cell was realized selecting the best electrolyte, and the more adequate electrode ink (*Chapter 6*) and the electrochemical activity of the obtained lab-scale device was tested using EIS measurements (*Chapter 7*). The outcomes are promising and interesting differences have been observed between the two compositions.

INTRODUCTION

"*The widespread use of fossil fuels is considered as one of the largest sources of CO_2 emissions, which is argued to cause global warming and climate change* "[1] is a sentence that we have heard several times in our lives, especially lately, but are we conscious of what does this truly mean?

We have noticed a difference in the climatic conditions and we know that it is caused by climate changes, but what brings us to that situation?

Greenhouse gases, such as carbon dioxide, methane, nitrous oxide, and certain synthetic chemicals, play an important role in that. They are both fundamental, as they trap some of the Earth's outgoing energy, thus retaining heat in the atmosphere, and problematic. In fact, the heat trapping causes changes in the radiative balance of the Earth—the balance between energy received from the sun and emitted from Earth—that alter climate and weather patterns at global and regional scales.

Natural factors, such as variations in the sun's output, volcanic activity, the Earth's orbit, the carbon cycle and others, also affect Earth's radiative balance. However, since the First Industrial Revolution in the late 1700s, the net global effect of human activities has resulted in a continuous increase in greenhouse gas concentrations (*Figure 0.1)*.

As reported by the U.S. Environmental Protection Agency (EPA)[2], CO_2 is considered as the most important anthropogenic greenhouse gas because is currently accounts for the greatest portion of the warming associated with human activities, through combustion of fossil fuels and other emissions sources, as it can be clearly seen in the following image.

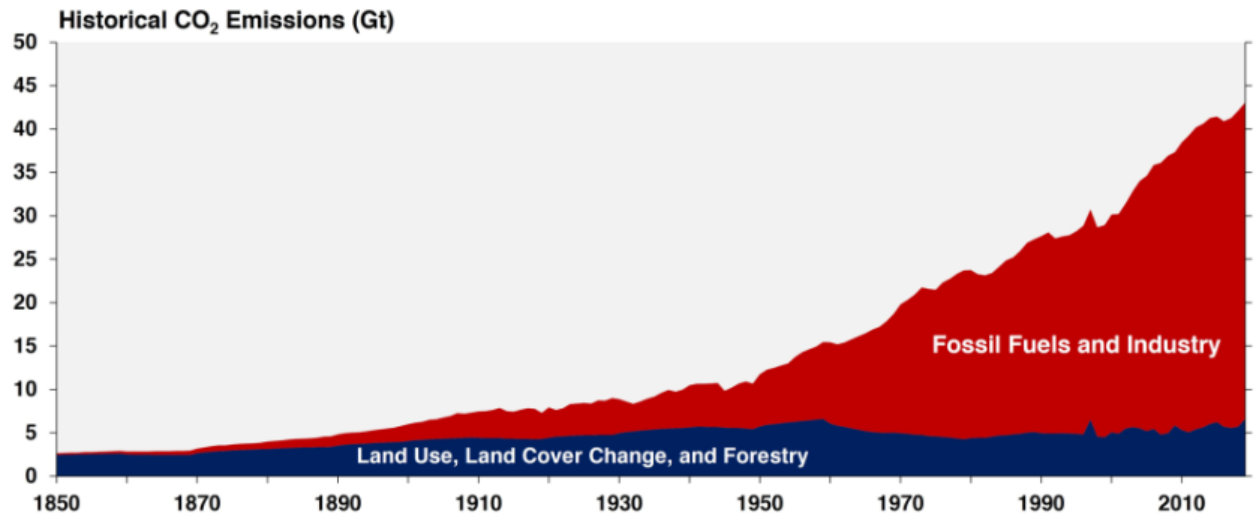

Figure 0.1: Historical CO_2 emissions from pre-industrial times till now [3]

This change in concentrations causes warming and is affecting various aspects of climate, including surface air and ocean temperatures, precipitation, and sea levels. Human health, agriculture, water resources, forests, wildlife, and coastal areas are all vulnerable to climate change.

It has been of crucial importance, on one hand, to find a way to diminish the amount of CO_2 produced by human activities. On the other hand, but linking to it, to exploit other sources, which can lead to the development of greener technologies, mainly based on friendly alternatives to fossil fuels (e.g., wind or solar): the renewable energies.[4] They are sometimes criticized for not providing the necessary security of supply because the production cannot be tuned to fit the consumers' needs. [1] In fact, they are intermittent in nature, meaning that they are not always usable.[5] For example, the availability of the hydropower is not even over the year. Biomass is a sustainable-energy source that is steadily available, but it cannot provide enough energy for the world because most of the fertile land area is needed for food production. [6]

The necessity of transitioning from non-renewable to renewable energy is driven not only by environmental factors but also by the actions of organizations and governments. For example, the 7th goal of Agenda 2030 is "Affordable and clean energy". In particular, in the report drew up by UN (United Nations) is highlight how about 660 million people will still lack access to electricity and close to 2 billion people will still rely on polluting fuels and

technologies for cooking by 2030. This phenomenon is particularly focused on developed countries, especially sub-Saharan Africa, where the number of people without access to electricity has remained stubbornly stagnant since 2010, leaving 567 million without access to electricity and 0.9 billion without access to safe and efficient cooking systems (*Figure 0.2*).[7]

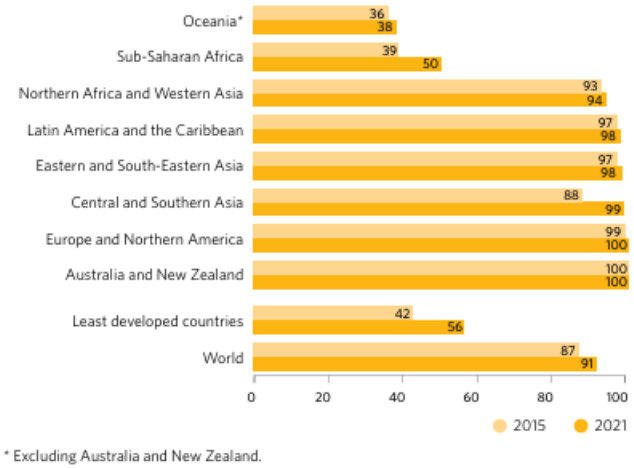

Figure 0.2: Proportion of population with access to electricity, 2015 and 2021 (percentage) [7]

Another point emphasized by Agenda 2030 is how the renewable energy use is growing in the electricity sector, but limited in heating and transport. Over the period 2015-2020, total renewable energy consumption increased by 16 per cent. Traditional uses of biomass- such as the burning of wood in open stoves or fireplaces- still represented over a third of total renewable energy use in 2020. The electricity sector shows the largest share of renewables in total final energy consumption (28.2 per cent in 2020). However, progress in the heating and transport sectors has been limited over the past decade, as upward trends in demand have outpaced the deployment of renewables. [7]

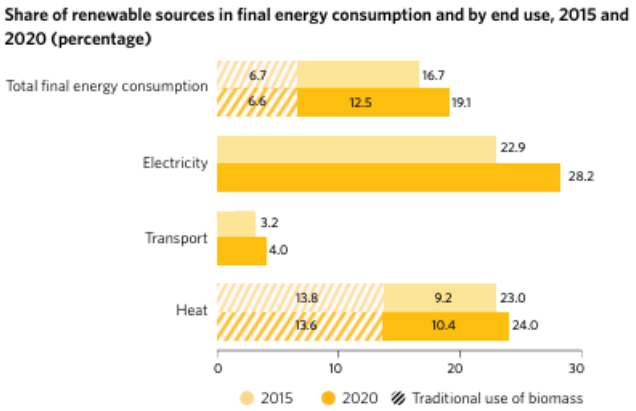

Figure 0.3: The use of renewable sources in final energy consumption and by end use, 2015 and 2020 (percentage) [7]

One of the proposal made for the abatement of Greenhouse Gas Emissions (GHG) regards the theme of decarbonisation; which is deeply analysed in relation to select sectors, in particular Iron and steel, Chemicals, Heavy-duty trucks, Shipping, Aviation, in 'Decarbonising hard-to-abate sectors with renewables' report, edited by IRENA (Internation Renewable Energy Agency) [8].

In 2023, 89% of new electricity capacity additions globally were renewable – up from 53% in 2013. Something similar is happening with passenger transport, where battery electric vehicle adoption is rising exponentially, some 13.6 million electric passenger cars were sold in 2023 alone – roughly 15% of total global automobile sales and a 425% increase since 2020. Some industrial and transport sub-sectors are substantial GHG emitters and are harder to decarbonise due to their physical, technological or market particularities. [8]

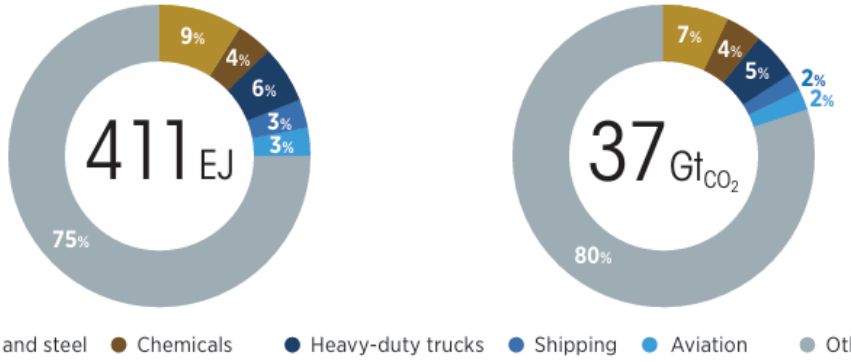

2022	Heavy-duty tracks	Shipping	Aviation	Iron and steel	Chemicals and petrochemicals
Activity	30 trillion tkm	110 trillion tkm	6 trillion pkm 220 billion tkm	1.8 billion tonnes	719 million tonnes
Energy consumption [EJ/year]	26.8	11.2	11	35	16
CO_2 emissions [Gt]	1.8	0.86	0.8	2.8	1.3

Source: (ICAO, 2023a; IEA, 2023a, 2023b; UNCTAD, 2022).
Note: EJ = exajoules; Gt = gigatonnes; tkm = tonne kilometre; pkm = passenger kilometre.

Figure 0.4: Energy consumption, CO_2 emissions, activity metrics for selected hard-to-abate sectors, 2022 [8]

That said, it appears clear that the 'typical' sources are not enough to support the world's energy demand (World's Total Primary Energy Supply), which the Internal Energy Agency (IEA)'s estimate of being 73761 Mtoe (million tons of oil equivalent), corresponding to 18.3 TWy (terawatt years) in 2016.

In order to produce 18.3 TWy electrical energy from photovoltaic cells with conservative 10% efficiency, we need solar irradiation of 183 TW electrical power on average over the year. The average influx of energy from the Sun (corrected for scattering in the atmosphere and absorption by clouds) to the land area between the polar circles corresponds to 21 000 TW average electrical power calculated from data from Tsao et al., i.e. 115 times more than we need. Actually, it takes only a small fraction of the world's deserts to supply all the

necessary energy to the world. The drawbacks concern the necessity to have huge conversion and storage capacity in order to have a continuous reliable energy supply and that these sources should be sold at similar prices to fossil fuels in order to be competitive to them.

Thus, to cover the world's energy demand, it takes efficient and inexpensive energy-conversion and storage systems in order to fully utilize the intermittent solar and wind energy as well as varying hydropower. There are a number of such conversion and storage technologies available, but none of them is suitable for seasonal storage and they are not suited for heavy transport such as trucks, ships and aeroplanes. Therefore, fuels like hydrogen, CO_2-neutral carbon-based fuels and/or ammonia produced from sustainable energy are interesting for chemical-energy storage and energy transportation. Conversion technologies that can produce such fuels from sustainable energy need electrolysis to convert renewable electrical energy into hydrogen (H_2) from water and carbon monoxide (CO) from carbon dioxide (CO_2). Hydrogen offers significant promise as a basis for a future energy technology, and is argued to be the most versatile, efficient and environmentally friendly fuel, although handling of H_2 may be problematic. In fact, it can be produced from fossil fuels (with some disadvantages, as the environmental problems associated with natural gas production, emission of CO_2, and the purity of the produced hydrogen), via biological processes, photochemical processes and electrolysis. Hydrogen produced via electrolysis, even at higher production prices, may sound interesting because of the high purity of H_2 produced.

Through the electrolyser, the device that guide the electrolysis, it is used electricity to split water or other components into their constituent elements, a mixture of H_2O and CO_2 can be electrolyzed to produce synthesis gas, or syngas (a mixture of H_2 and CO), via a combination of Eq. 1 and 2 to yield both H_2 and CO.

$$H_2O \ + \ electric\ energy\ (\Delta G) \ + \ heat\ (T\Delta S) \ \rightarrow \ H_2 + \frac{1}{2}O_2$$

Equation 1

$$CO_2 + \ electric\ energy\ (\Delta G)\ +\ heat\ (T\Delta S)\ \rightarrow\ CO\ +\ \frac{1}{2}O_2$$

Equation 2

Syngas can be converted into various types of synthetic fuels, of which methane, methanol, and dimethyl ether are the simplest and cheapest to produce, through the Fischer–Tropsch process. [1,6]

Hydrogen will work as energy carrier, as soon as electrolysis modality is reached, and could be stored in the device until the production of electricity is needed. After, fuel cell procedure takes place, in which the electricity is produced through the oxidation of H_2 to H_2O.

$$H_2\ +\ \frac{1}{2}O_2 \rightarrow\ H_2O\ +\ \ electric\ energy\ (\Delta G) + heat\ (T\Delta S)$$

Equation 3

A device which can operate in both modality is so called reverse Solid Oxide Cells (r-SOCs, described in *Section 1.7*). This means that the same cell can interchangeably be used in both modes. The overall principle is sketched in *Figure 0.5*.

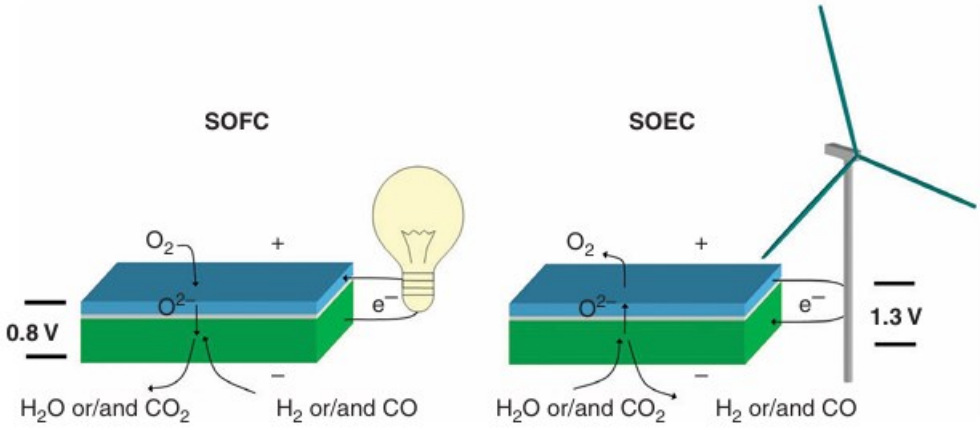

Figure 0.5: Sketch of the principle of SOCs in SOFC and SOEC modes of operation. The blue top layer illustrates the oxygen electrode, the white the electrolyte and the green layer illustrates the fuel electrode [6]

1. FUEL CELLS and ELECTROLYSERS

1.1. Fuel Cells introduction

Fuel Cells (FC) are electrochemical devices able to convert chemical energy (in form of fuels) in electrical energy with high efficiency and low environmental impact. Their working principle is based on a series of redox reactions between a fuel (usually hydrogen), that needs to be oxidized, and an oxidizing agent (usually air). In short, a fuel cell may be simply defined as an energy conversion device for power generation, similar to batteries and heat engines. The main difference between fuel cells and batteries is that FCs will continue to churn out product (electricity) as long as raw material (fuel) is supplied.

In a fuel cell, the hydrogen combustion reaction is split into two electrochemical half reactions:

$$H_2 \rightleftharpoons 2H^+ + 2e^-$$

Equation 4

$$\frac{1}{2}O_2 + 2H^+ + 2e^- \rightleftharpoons H_2O$$

Equation 5

By spatially separating these reactions, the electrons transferred from the fuel are forced to flow through an external circuit (thus constituting an electric current) and do useful work before they can complete the reaction, otherwise H^+ and e^- will recombine without the flowing of electricity.

Spatial separation is accomplished by employing an electrolyte.

Talking about advantages of FC, they are often far more efficient than combustion engines, as they produce electricity directly from chemical energy and are not limited by the Carnot efficiency. Then, the lack of moving parts, leads to highly reliable, long-lasting and silent systems.

Unlike batteries, fuel cells allow easy independent scaling between power (determined by the FC size) and capacity (determined by the fuel reservoir size). FCs offer potentially higher energy densities than batteries and can be quickly recharged by refuelling, whereas batteries must be thrown away or plugged in for a time-consuming recharge.

While FCs present intriguing advantages, they also possess some serious disadvantages. Cost represents a major barrier to fuel cell implementation. Power density -which is how much power a FC can produce per unit volume or per unit mass- is another significant limitation. Combustion engines and batteries generally outperform fuel cells on a volumetric power density basis; on a gravimetric power density basis, the race is much closer.[9] Another drawback is the difficulties that rely on hydrogen gas, which is the fuel that work best on FC. H_2 is not a widely available, has a low volumetric energy density, and is difficult to store. A possible answer to these problems, however, is the use of High Temperature Fuel Cells, where hydrogen can be produced and used in situ by internal reforming. A further solution could be the use of reversible SOFC (r-SOFC) devices, that can operate following two paths: the first ensures the production of energy from fuels (through SOFC modality), the second permits the production of hydrogen operating the inverse process (through SOEC modality, with electric energy produced from renewable sources, for example).

Although fuel cells are not a widespread technology, in the recent few years the energy production deriving from these devices has seen an important increase. As reported by ERM (Environmental Resources Management), 85% of shipments (2.113 MW) of fuel cells around the world are used for mobility, primarily cars, in 2022. The major fuel cell car companies are Hyundai and Toyota, the next main contributor to vehicle shipments is China, with a record 3.789 units (buses and trucks) being shipped in 2022. Fuel cells for ships and for aviation remains exploratory.

Larger, fuel cells for prime power and for industrial CHP (stands for Combined Heat and Power, also known as cogeneration, a technology that produces electricity and thermal energy at high efficiencies) continue to grow slowly overall, with 325 MW shipped in 2022, compared to 297 MW in 2021.

Aside from telecoms backup (the largest historic application), there is now a growing emphasis on large mobile systems for events and for construction works. These are ported systems, not hand portable, requiring wheels or lift hoists.

Shipments of portable fuel cells (including smaller Auxiliary Power Units, APUs, less than 20 kW) showed an increase, from just over 6,000 units in 2021, to nearly 8,000 units in 2022. These are supplied globally, but most feed into European and North American industrial and consumer markets. [10]

The following two graphs sum up all the data just cited.

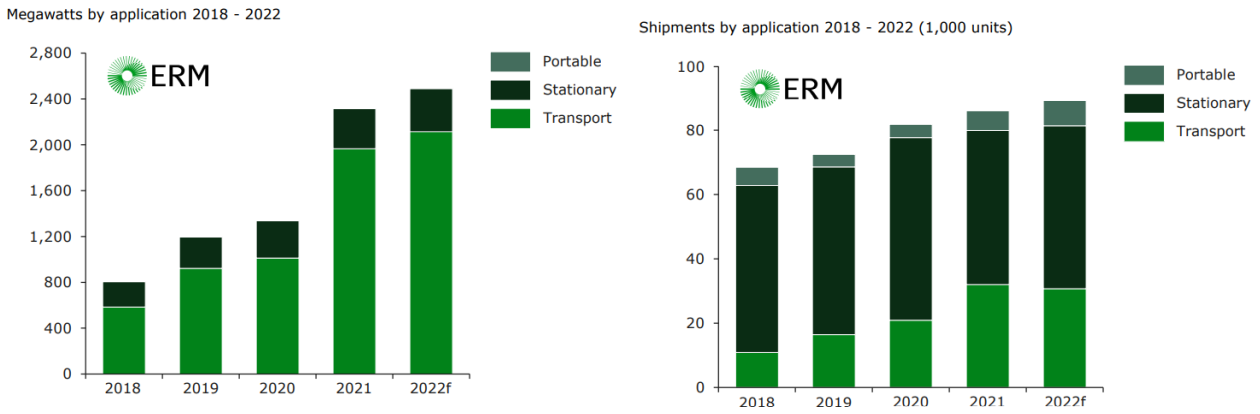

Figure 1.1: on the left the graph of the megawatts produced by the fuel cell by application, on the right the shipments of fuel cell by application, 2018-2022 [10]

1.1.1. Fuel Cells efficiency

Even if fuel cells present a higher efficiency compared to traditional combustion-based devices, there are some limitations that are not possible to overcome.

The total energy produced is:

$$W_e = \eta_T \cdot W_c$$

Equation 6

where η_T is the total efficiency and W_C the total chemical energy supplied by the fuel. The chemical energy that is not used to produce electrical energy can be evaluated by the efficiency of fuel use (η_C), by the Gibbs efficiency (η_G) and by the electrical efficiency (η_V). The efficiency of fuel use (η_C) is the quantity of fuel that is consumed with relation to the quantity that was supplied and depends on the kinetics of the process and on its parameters (temperature, catalytic activity of materials, geometry of the cell). It is calculated as following:

$$\eta_C = \frac{(H_2)_{in} - (H_2)_{out}}{(H_2)_{in}}$$

Equation 7

The Gibbs efficiency (η_G) is the ratio between the Gibbs free energy and the enthalpy of the chemical reaction involved in the cell:

$$\eta_G = \frac{\Delta_r G}{\Delta_r H} = \frac{(\Delta_r H - T\Delta_r S)}{\Delta_r H} = 1 - \frac{T\Delta_r S}{\Delta_r H}$$

Equation 8

ΔrS represents the chemical energy fraction that is dissipated as heat and it is the parameter on which the lower yield depends on.

Moreover,

$$\Delta \mathrm{rH} = \left(\left(\frac{\partial \Delta_r H^0}{\partial T} \right)_p = \Delta_r C_p \right)$$

Equation 9

can be considered independent from T because ΔrCp is usually very small and can be approximated to zero.

It is then possible, to identify η_G, linking it to the fact that only the chemical energy quantity defined by ΔrG can be turned into useful work. Even with this limitation, fuel cells have a better efficiency (at low T) than a combustion-based device, because there are not the limitations imposed by the Carnot cycle for the conversion of heat into useful work.

The electrical efficiency (ηv) is the ratio between the effective cell potential and the theoretical thermodynamic value calculated as follows:

$$\eta_V = \frac{V}{\Delta E_{rev}} = \frac{\Delta E_{rev} - R_{tot} \cdot I}{\Delta E_{rev}}$$

Equation 10

Where the electromotive force (ΔE_{rev}) is calculable from the Gibbs free energy:

$$\Delta Erev = -\Delta rGF$$

Equation 11

The electrical efficiency is due to the cell internal ohmic losses. They can be dependent on the current flow ($R(i)$, polarization, electronic transfer, etc.) or independent from it (R_0, ohmic resistance of the materials). It follows:

$$R_{tot} = R_o + R(i)$$

Equation 12

when $R(i) \ll R_0$, that is usually verified, the electrical efficiency can be linearized, assuming $R_{tot} = R_0$:

$$\eta_V = \frac{V}{\Delta E_{rev}} = \frac{\Delta E_{rev} - R_0 \cdot I}{\Delta E_{rev}} = 1 - \frac{R_0 \cdot I}{\Delta E_{rev}}$$

Equation 13

The internal resistance $R(i)$ is not always negligible. In those cases, the main contribute is the activation overpotential of the electrode processes that happens in the cell.

The overall efficiency is then: $\eta_T = \eta_C \cdot \eta_G \cdot \eta_V$

Equation 14

It follows: $W_e = \eta C \cdot \eta G \cdot \eta V \cdot W_c$

Equation 15

1.2. Fuel Cell typologies

Fuel cells classification is based on their electrolyte, fuel and working temperature, as it can be seen in *Figure 1.2*.

Thus, it is possible to differentiate the devices in two categories:

Low temperature Fuel Cells (50-250°C):

- Proton Exchange Membrane Fuel Cells (PEM)
- Phosphoric Acid Fuel Cells (PAFC)
- Alkaline Fuel Cells (AFC)

High temperature Fuel Cells (600-1000°C):

- Direct Methanol Fuel Cells (DMFC)
- Molten Carbonates Fuel Cells (MCFC)
- Solid Oxide Fuel Cells (SOFC)

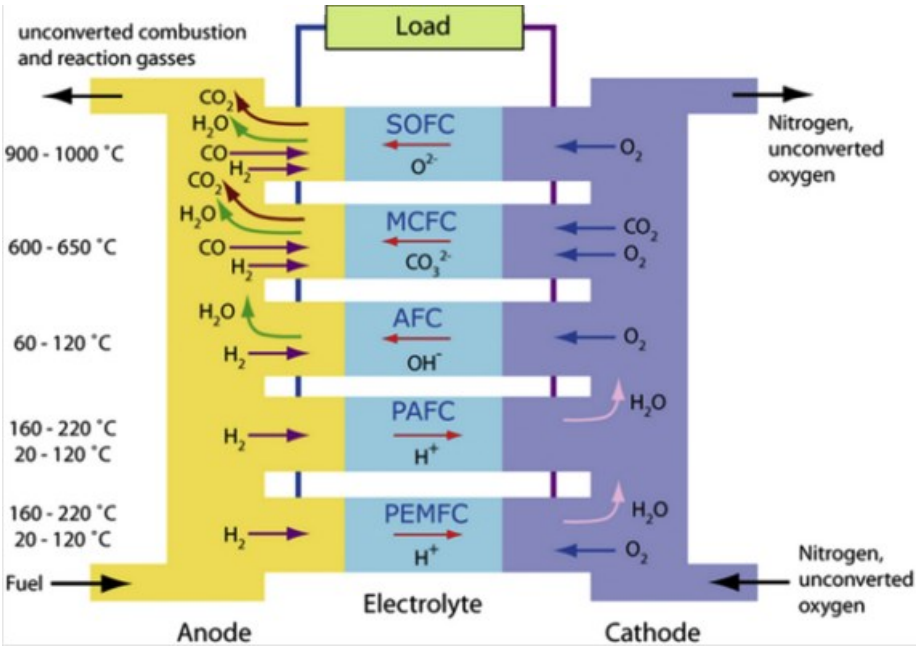

Figure 1.2: Fuel cell typologies, divided by operation temperatures

Fuel Cell Type	Common Electrolyte	Operating Temperature	Typical Stack Size	Electrical Efficiency (LHV)	Applications	Advantages	Challenges
Polymer Electrolyte Membrane (PEM)	Perfluorosulfonic acid	<120°C	<1 kW - 100 kW	60% direct H_2;[i] 40% reformed fuel[ii]	• Backup power • Portable power • Distributed generation • Transportation • Specialty vehicles	• Solid electrolyte reduces corrosion & electrolyte management problems • Low temperature • Quick start-up and load following	• Expensive catalysts • Sensitive to fuel impurities
Alkaline (AFC)	Aqueous potassium hydroxide soaked in a porous matrix, or alkaline polymer membrane	<100°C	1 - 100 kW	60%[iii]	• Military • Space • Backup power • Transportation	• Wider range of stable materials allows lower cost components • Low temperature • Quick start-up	• Sensitive to CO_2 in fuel and air • Electrolyte management (aqueous) • Electrolyte conductivity (polymer)
Phosphoric Acid (PAFC)	Phosphoric acid soaked in a porous matrix or imbibed in a polymer membrane	150 - 200°C	5 - 400 kW, 100 kW module (liquid PAFC); <10 kW (polymer membrane)	40%[iv]	• Distributed generation	• Suitable for CHP • Increased tolerance to fuel impurities	• Expensive catalysts • Long start-up time • Sulfur sensitivity
Molten Carbonate (MCFC)	Molten lithium, sodium, and/or potassium carbonates, soaked in a porous matrix	600 - 700°C	300 kW - 3 MW, 300 kW module	50%[v]	• Electric utility • Distributed generation	• High efficiency • Fuel flexibility • Suitable for CHP • Hybrid/gas turbine cycle	• High temperature corrosion and breakdown of cell components • Long start-up time • Low power density
Solid Oxide (SOFC)	Yttria stabilized zirconia	500 - 1000°C	1 kW - 2 MW	60%[vi]	• Auxiliary power • Electric utility • Distributed generation	• High efficiency • Fuel flexibility • Solid electrolyte • Suitable for CHP • Hybrid/gas turbine cycle	• High temperature corrosion and breakdown of cell components • Long start-up time • Limited number of shutdowns

Figure 1.3: classification of fuel cells [11]

1.1.2. Proton Exchange Membrane Fuel Cells (PEMFCs) [12]

The PEMFC is certainly the most known technology among the fuel cell types and it is considered as a potential replacement for internal combustion (IC) engines in the transport sector. These devices are mainly based on a polymeric membrane, that acts as electrolyte and ensures the proton conductivity (while electron flow is blocked), bonded between two porous electrodes; the principal compound used for this purpose is Nafion®, a sulfonated tetrafluoro ethylene-based co-polymer.

The processes involved are the combustion of H_2 with the consequent production of H_2O:

anode: $2H_2 \rightarrow 4H^+ + 4e^-$

Equation 16

cathode: $O_2 + 4H^+ + 4e^- \rightarrow 2\ H_2O$

Equation 17

overall process: $2\ H_2 + O_2 \rightarrow 2\ H_2O$

Equation 18

PEMs are able to reach efficiency of about 50%, with a power density comparable to an IC engine one (1.35 kW/L). Nevertheless, the main advantage of these cell is its low operative temperature of about 60-80°C, that assure very quick start-and-stop operations thanks to the possibility to reach quickly the operating temperature regime. This is the principal reason that makes these cells suitable for portable applications. The low operating temperature, however, is the cause for the slow chemical kinetics of these cells. For this reason, Platinum Group Materials (PGMs), which are critical raw materials, with low abundancy and located in specific geographic areas, that result in a high cost and an uncertain supply, are needed as catalysts for both anode and cathode reactions.

1.1.3. Phosphoric Acid Fuel Cells (PAFCs) [13]

In the last decade, PAFC have increased in popularity, thanks to their good reliability, even though the electrical efficiency is around 40%. These cells are highly used where the energy supply cannot be stopped, even for a short period of time. Compared to the traditional power supply systems, this kind of devices ensures a reduction of fuel usage and pollution

emissions. PAFCs' main characteristic is that the electrolyte is phosphoric acid (H_3PO_4), that ensures a cationic mobility. The processes involved are:

anode: $2H_2 \rightarrow 4H^+ + 4e^-$

Equation 19

cathode: $O_2 + 4H^+ + 4e^- \rightarrow 2H_2O$

Equation 20

overall process: $2H_2 + O_2 \rightarrow 2H_2O$

Equation 21

This device has a working temperature of about 200°C, and a catalyst is needed; carbon-supported platinum is the most commonly used one, both for the oxidation of hydrogen fuel at the anode and oxygen reduction at the cathode. Its cons are platinum dissolution and carbon corrosion at voltages above 0.8 V, together with the kinetic impediment of the oxygen reduction reaction. More studies are then needed to optimize these types of catalysts.

1.1.4. Alkaline Fuel Cells (AFCs) [14]

AFCs are probably, from a historical point of view, the most important type of fuel cells. In fact, one of these cells was installed by NASA during the Apollo program in the 60's.

This device is characterized by an alkaline aqueous electrolyte made of potassium hydroxide (KOH), which assures high mobility of hydroxide anions (OH^-) but with some disadvantages, as its high sensitivity to CO_2, with which it reacts consuming itself. Moreover, KOH is highly corrosive and confers a short life cycle to the device. The following processes are involved in the cell operation:

anode: $2H_2 + 4OH^- \rightarrow 4H_2O + 4e^-$

Equation 22

cathode: $O_2 + 2H_2O + 4e- \rightarrow 4OH^-$

Equation 23

overall process: $2H_2 + O_2 \rightarrow 2H_2O$

Equation 24

The working temperature is about 100°C and the electrical efficiency is relatively high (60%). These devices are not suitable for commercial applications due to complication related to the alkaline electrolyte, but they're still used in boats and Space Shuttles.

1.1.5. Molten Carbonate Fuel Cells (MCFCs) [15]

MCFCs are characterized by a working temperature above the melting temperature of the carbonates and the results is the charge transportation by the carbonate ion (CO_3^{2-}) within the liquid electrolyte. For the electrolyte, most developers have adopted a molten mixture of alkali metal carbonates -usually a binary mixture of Li and K, or Li and Na carbonates, which is retained in a ceramic matrix of $LiAlO_2$- which has a melting point around 550°C. However, the operating temperature of these devices is around 650°C. Since both anode and cathode also need to be porous to allow the reacting gases to reach the electrode/electrolyte interfaces, the pore structure of the cell components needs to be carefully controlled so that electrolyte loss is minimized.

The reaction involved at the electrodes are:

anode: $2H_2 + 2CO_3^{2-} \rightarrow 2H_2O + 2CO_2 + 4e^-$

Equation 25

cathode: $O_2 + 2CO_2 + 4e^- \rightarrow 2\ CO_3^{2-}$

Equation 26

overall process: $2H_2 + O_2 \rightarrow 2H_2O$

Equation 27

The electrical efficiency of this cell is about 50% and the total projected one is of 80%. The difference in this two terms could be related to the fact that some of the electricity produced is reused in the cell, for example.

Although the materials costs are relatively low if compared with other fuel cell types (no PGMs are required as electro-catalysts), there are major problems associated with degradation of materials and the poor lifetime of cells. So, nowadays research is focused both in the selection of materials to increase the operating life of the cell and system design to maximize the benefit of internal reforming.

1.1.6. Market distribution

In recent times, fuel cells are gaining importance in the industrial and transportation market. This has influenced the field of study of these devices, that is increasing more and more.

As reported by Fortune Business Insights, the global fuel cell market size was valued at USD 9.85 billion in 2023 and is projected to grow from USD 12.75 billion in 2024 to USD 105.01 billion by 2032. Asia-Pacific dominated the fuel cell industry with a market share of 61.21% in 2023. [16]

Regarding the Type Analysis, it is shown that the most used in the market nowadays are:

I. Proton Exchange Membrane Fuel Cell (PEMFC)
II. Solid Oxide Fuel Cell (SOFC)
III. Phosphoric Acid Fuel Cell (PAFC)
IV. Others

The Proton Exchange Membrane Fuel Cell (PEMFC) segment dominates the global market, both in volume and in MW capacity. The demand for PEMFC is higher owing to various benefits over other types. Benefits, such as flexibility in input fuel, compact design, lightweight, low cost, and solidity of electrolyte, will aid market escalation.

The Solid Oxide Fuel Cell (SOFC) segment is estimated to grow significantly during the forecast period. SOFC has been gaining significant share due to the stack's higher efficiency and higher-grade heat. The MW count grew from 207 MW in 2021, to 249 MW in 2022. Much of this is attributable to stronger sales from Bloom Energy (an American public company headquartered in California). The net increase in SOFC shipment capacity is associated with increased bloom units for prime power shipments in the U.S. and Korea, while other suppliers like Bosch and Ceres are influent for a smaller volume.

PAFCs have not met the expectation. The market is dominated by Doosan Fuel Cell's play in South Korea, issues like plant reliability, spark spread differentials and the slowness for policy to kick in have dogged sales. MCFCs have not seen an increase in the unit sold. Last but not least, AFCs continue its advance from near obscurity, with over 100 shipments globally through 2022. Most of these are from GenCell, mainly for remote telecoms backup to renewable energy ensembles. The company, AFC Energy, which began in 2006, has at last started to ship units to early adopters, believed to be less than 10 units sold over 2022.

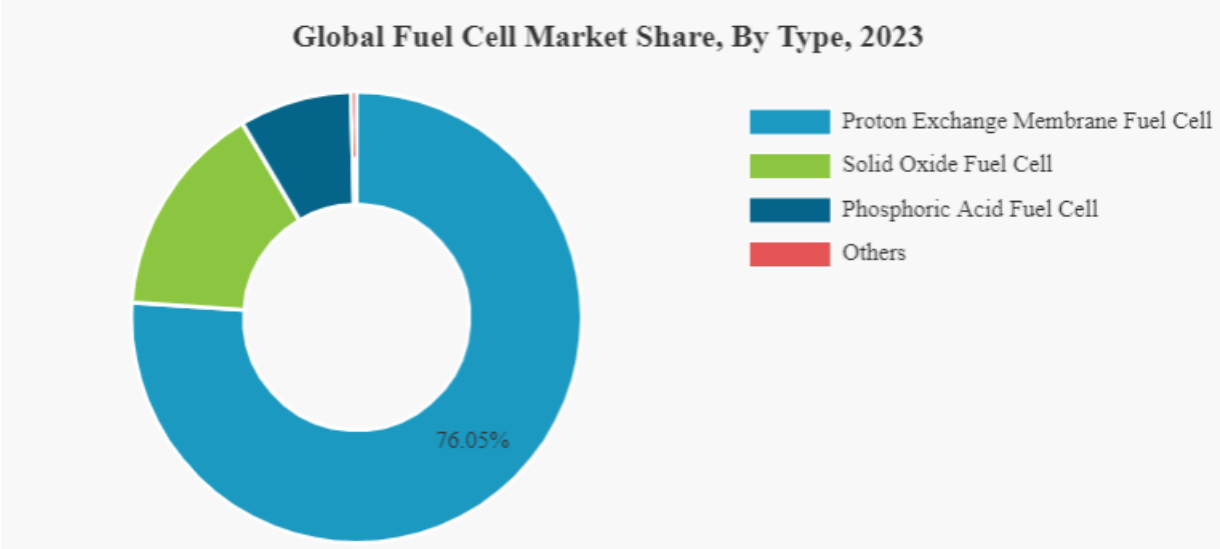

Figure 1.4: Global Fuel Cell market share, divided by type, 2023 [16]

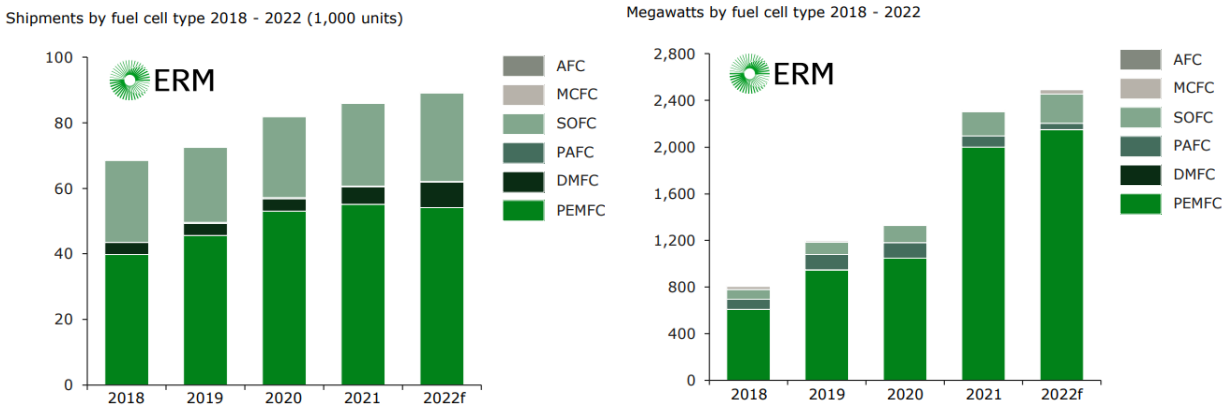

Figure 1.5: on the left the shipments of fuel cell, on the right the megawatts produced by fuel cell type, divided by typologies, 2018-2022 [10]

1.3. Solid Oxide Fuel Cells (SOFCs)

SOFCs are based on a solid electrolyte, usually a mixed oxide, that can exhibit either ion conductivity (O^{2-}) or proton conductivity (H^{+}) but has to be electrically isolating. Both anode and cathode need to be porous, in order to guarantee an optimal gas diffusion between the cell sides.

The occurring reactions in an ideal cell, with the fuel composed of only H_2, are:

anode: $2H_2 + 2O^{2-} \rightarrow 2H_2O + 4e^-$

Equation 28

cathode: $O_2 + 4e^- \rightarrow 2O^{2-}$

Equation 29

overall process: $2H_2 + O_2 \rightarrow 2H_2O$

Equation 30

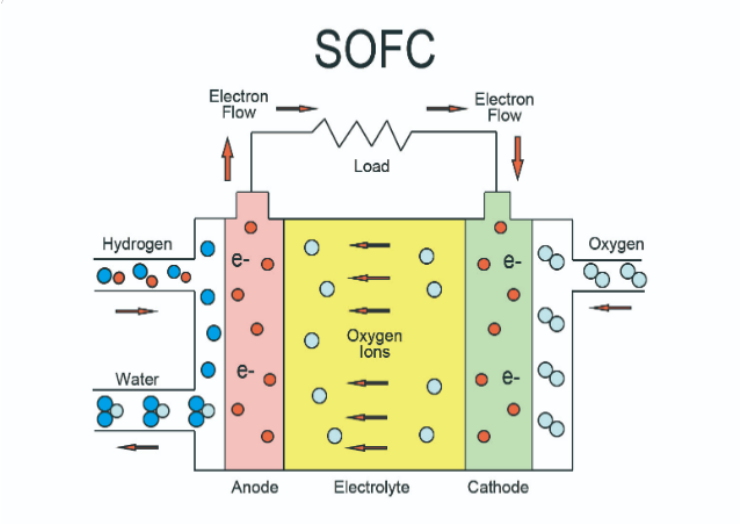

Figure 1.6: SOFC scheme [93]

SOFCs seem to be very promising as energy production technology, due to their numerous advantages, the most notable being:

- the possibility to tune the fuel in a flexible manner (for example, hydrogen, carbon dioxide, natural gas, bio gas, methanol, dimethyl ether and ammonia)
- the wide operating temperature range, that goes from 400-600°C for gadolinium-doped ceria (GDC) electrolytes to 650-950°C for strontium and magnesium-doped lanthanum gallate (LSGM), or yttria stabilized zirconia (YSZ); due to the high working temperatures, PGMs catalysts are not required [17]
- Nonprecious metal catalyst [18]
- High-quality waste heat for cogeneration applications [18]

Moreover, SOFC attractiveness comes also from their capability to be used in the reverse way, and so to produce hydrogen from water electrolysis using the excess of electric energy: ideally this device, the so-called reverse Solid Oxide Cell (r-SOC, *Section 1.7*), has the opposite working principle of the SOFC, operating also as a Solid Oxide Electrolysis Cell (SOEC, *Section 1.6)*. This technology has gained interest lately, as it is particularly keen to work for the production of energy and as energy storage, it will be further explained in *Section 1.7*.

1.3.1. Cell components: the anode (fuel electrode)

The anode is the component of the fuel cell where the fuel oxidation reaction takes place and where the produced electrons are put in the external circuit. Thus, it is mandatory for the anodic material to have enough active sites to host this reaction. Although the oxidation of hydrogen is kinetically favoured in respect to the reduction of oxygen at the cathode side of the cell, the anode becomes particularly relevant assuming the use of different fuels, which may require special characteristics (e.g., avoiding catalyst poisoning by coke in the case of carbon-containing fuels). The anode, in SOFC mode, works as the negative electrode. Anode being negative in nature, allows distribution of positive ions obtained from the hydrogen gas fuel equally over its whole surface. The conduction of electrons released from hydrogen molecule takes place, which is utilized as a useful power in the external circuit. [19] From the theoretical point of view, it is desirable to have an anode material with the following characteristics [20]:

- High electrical conductivity
- High electrocatalytic activity in fuel oxidation
- Good ionic conductivity
- Thermal expansion coefficient matching the electrolyte
- Chemical compatibility with the electrolyte
- Good adhesion to the electrolyte
- Capacity to prevent coke formation at the active site, mandatory for C-containing fuels
- High porosity, in order to have a better gas diffusion

The state-of-the-art material is a cermet made of Ni and YSZ, as nickel alone is quite cheap and exhibits good electrochemical action in case of H_2-based oxidation reaction, but its adhesion to the electrolyte is problematic, so it needs a ceramic material as support, YSZ. This material is also useful to avoid the sintering between nickel particles and to have a thermal expansion coefficient that is the more similar to the electrolyte one ($13.3 \cdot 10^{-6}$ K^{-1} for Ni, $10.5 \cdot 10^{-6}$ K^{-1} for YSZ); moreover, this material is known to have a good porosity (20-40%) and good conductivity, both ionic and electronic. However, it is not a drawback-free material, as Ni particles aggregate and eliminate the triple-phase boundary (TPB) reducing the porosity of the anode and thereby decreasing cell performance at high temperatures.

Furthermore, there are some losses due to the ohmic polarization at the interface electrode-electrolyte. The research has later moved to novel ceramic materials, characterized by having a good conductivity, both ionic and electronic, the so-called Mixed Ionic and Electronic Ceramics (MIECs), which have the main advantage of enlarging the Triple Phase Boundary (TPB) between fuel, anode and electrolyte. Examples of these materials are Cu-CGO, Ni-CGO, Cu-Ni-CGO. Also perovskites are lately particularly attractive, as they exhibit mixed ionic and electronic conductivity. [15]

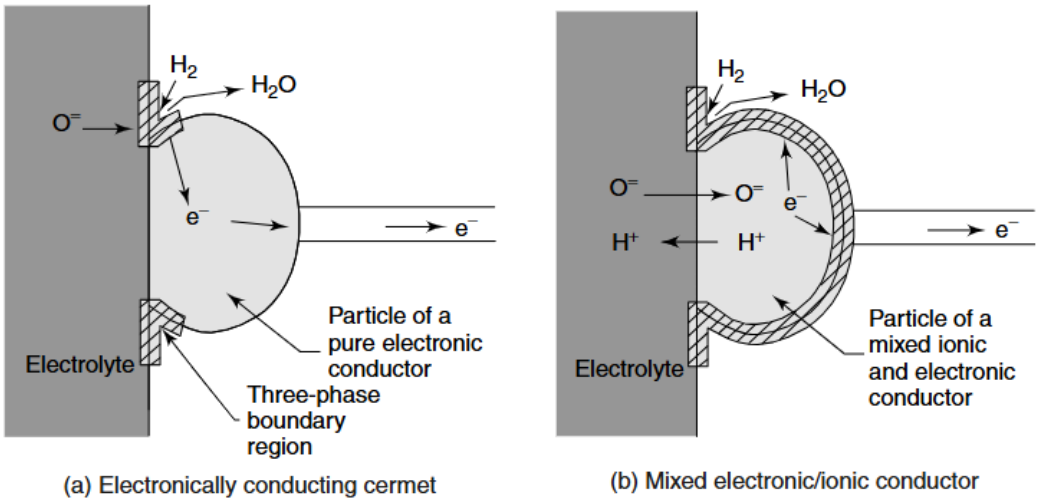

Figure 1.7: Different types of anode material: a) electronically conducting cermet, b) mixed electronic/ionic conductor[18]

1.3.2. Cell components: the cathode [15]

Similar to the anode, the cathode is a porous structure that must allow rapid mass transport of reactant and product gases. It is the side of the cell where the reduction of oxygen takes place; this reaction is, usually, the rate-determining step of the cell working procedure, and thus it is mandatory for the materials used to this aim to have a good TPB regions. The cathode works as the positive electrode, being positive in nature, oxygen ions are distributed fairly over the surface of cathode electrode. Taking into account that the non-stoichiometry and the defects of oxygen have a great effect on ionic and electronic transport properties of the material, perovskite-based materials are a suitable option for the cathode. It creates a conducting pathway for electrons back from the external circuit with the option

of recombining with oxygen ions transporting through the solid electrolyte and with hydrogen to form water.

Strontium-doped lanthanum manganite ($La_{0.84}Sr_{0.16}MnO_3$), a p-type semiconductor, is most commonly used for the cathode material.

The principal drawback of LSM is the interaction with YSZ at high temperature to form the isolating phase $La_2Zr_2O_7$ (LZ) at the interface, thus lowering the performances of the cell; moreover, the Sr concentration should not exceed the value of 30% mol, in order to avoid the formation of SrZrO3 (SZ) from the interaction with the electrolyte.

However, LSM materials cannot be used at temperatures below 800°C, due to the increasing cathode polarization while lowering the temperature and to the absence of oxygen vacancies, that restricts the reduction of oxygen to the TPB regions.

1.3.3. Cell components: the electrolyte [15]

The electrolyte, the middle part of the cell, should ensure to the device an optimal ionic conductivity while its electronic conductivity must be kept as low as possible to avoid leakage currents and thus worst overall performances. The working temperature is a relevant variable in SOFCs operations, as the higher it is, the better will be the oxygen transportation and thus the performance; the lower limit is considered to be 600°C, at which the resistance related to oxygen transportation is no more negligible.

The most known electrolyte materials are:

I. Yttria-Stabilized Zirconia (YSZ):
usually composed by zirconia (ZrO_2) doped with 8 to 10% mol of yttria (Y_2O_3); the result is a ceramic material stable both in oxidizing and reducing environments that are to be found at the anode and cathode of the fuel cell, respectively. The ability to conduct O^{2-} ions is brought about by the fluorite crystal structure of zirconia in which some of the Zr^{4+} ions are replaced with Y^{3+} ions. When this ion exchange occurs, several oxide-ion sites become vacant because of three O^{2-} ions replacing four O^{2-} ions. Oxide-ion transport occurs between vacancies located at tetrahedral sites in the perovskite lattice.

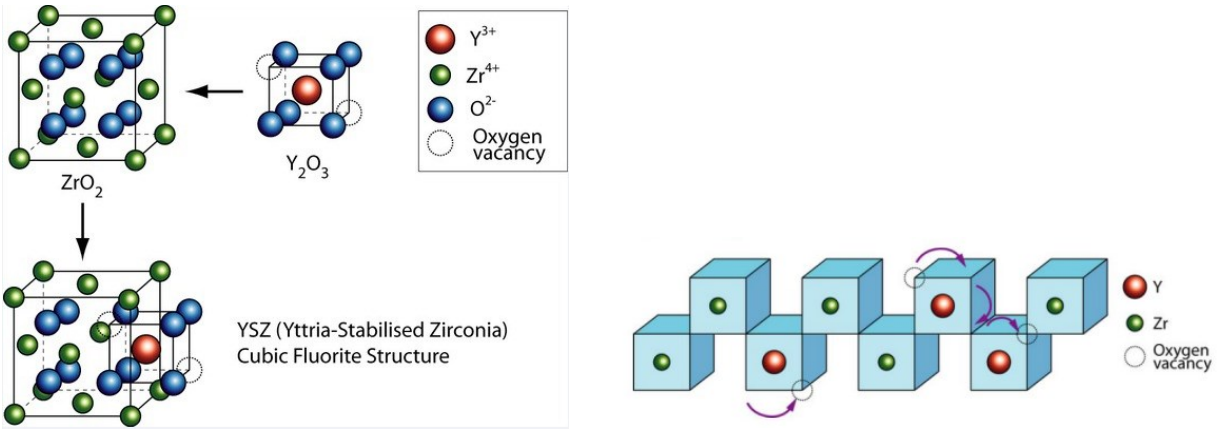

Figure 1.8: on the left, the crystalline structure of YSZ, on the right, the oxygen transportation through vacancies [21]

The ionic conductivity of YSZ at high temperatures is comparable with that of liquid electrolytes (0.1 S cm^{-1} at 1000°C). The main issue is the high ohmic losses related to the thickness of the electrolyte.

II. Cerium oxide:

Usually doped with trivalent cation, in order to suppress the oxygen vacancy ordering, consequent to the presence of the Ce (III)/Ce (IV) redox couple, thereby lowering the activation energy (E_a) and improving oxide ion conductivity at intermediate temperature (higher than YSZ itself). The drawback is the less stability at low oxygen partial pressures as found at the anode of the SOFC. This gives rise to defect oxide formation and increased electronic conductivity and thus internal electric currents, which lower the cell potential.

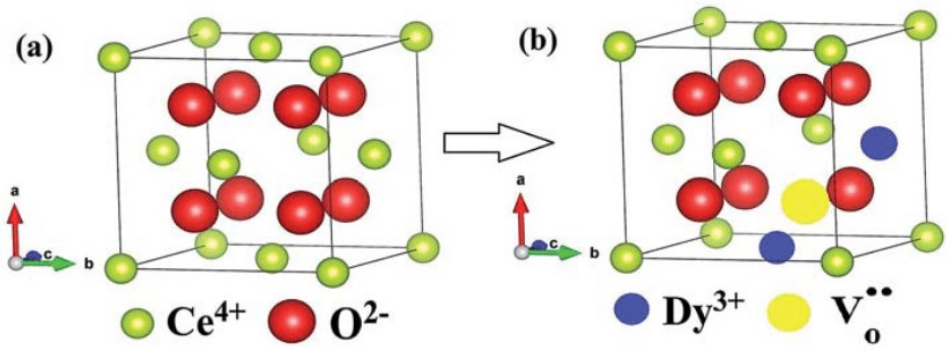

Figure 1.9: the crystal structure of a Dy-doped ceria [94]

III. Strontium-Magnesium doped Lanthanum Gallate (LSGM) [22]

In his composition $La_{0.8}Sr_{0.2}Ga_{0.8}Mg_{0.2}O_6$ presents an ionic conductivity at 800°C of the same magnitude order of YSZ at 1000°C. The material is a lanthanum gallate ($LaGaO_3$) doped in A-site with Sr and in B-site with Mg, that decreases the total electrical

conductivity and enhances the ionic conductivity. The ionic conductivity is enhanced via the substitution of La^{3+} ions with Sr^{2+} and of Ga^{3+} with Mg^{2+}. The main disadvantages of this electrolytes regards the material before it is doped, the formation of stable secondary phase and the relatively high cost.

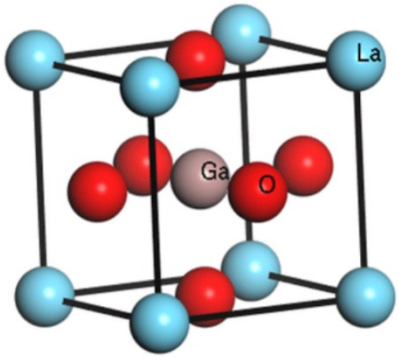

Figure 1.10: unit cell of c-$LaGaO_3$ [95]

1.3.4. SOFCs challenges

SOFC technology offers a promising approach to generating energy in a clean and sustainable manner; however, significant advancements are required to achieve widespread commercial adoption. Currently, state-of-the-art SOFCs operate only at high temperatures and are costly to manufacture and sell. Therefore, substantial efforts are needed to develop new materials that can reduce operating temperatures and production costs while maintaining the device's performance and structural stability.

1.4. Electrolysers introduction [23]

Electrolysis cells require the electrical energy input for driving the non-spontaneous electrochemical and chemical changes to occur at the electrodes. Every electrolytic cell consists of the following components:

- an external power supply;
- electrolyte ;
- anode for the oxidation of water (anodic catalytic layer);
- cathode for reduction of water (cathodic catalytic layer).

Electrolytic processes and electrolysers are used for a diverse range of applications including synthesis of chemicals and materials, extraction and production of metals,

recycling, water purification and effluent treatment, metal and materials finishing and processing, energy storage and power generation and corrosion protection.

In an electrolyser, as in the case of a FC, the two electrodes are spatially separated by an electrolyte, in order to force the electrons to flow through an external circuit and to avoid explosive mixtures between the developed gases. Important to mention is the fact that the cathode of SOFC corresponds to the anode of SOEC. In general, the cathode in SOEC is where the reduction of CO_2/H_2O takes place, while in SOFC is where the reduction of O_2 occur. On the other way around, the anode in SOEC is where O^{2-} oxidize to O_2 and in SOFC is where H_2 oxidize to H_2O.

The concept of water electrolysis cell (used for the electro-dissociation of water into molecular hydrogen and oxygen) is more than two-century old now. During water electrolysis, DC current passes through the electrodes when a voltage is applied.

The overall process is summarized in the following equation:

$$H_2O \ + \ electric\ current \rightarrow \ H_2 + \frac{1}{2} O_2$$

Equation 31

Hydrogen can be used in its pure form as an energy carrier or as an industrial raw material. In recent years, colours have been used to refer to different sources of hydrogen production. "Black," "Grey," or "Brown" refer to the production of hydrogen from coal, natural gas, and lignite, respectively. "Blue" is commonly used to produce hydrogen from fossil fuels with CO_2 emissions reduced by the use of CCS (Carbon Capture and Storage) . "Green" is a term applied to the production of hydrogen from renewable electricity to electrolyze water (*Figure 1.11*).

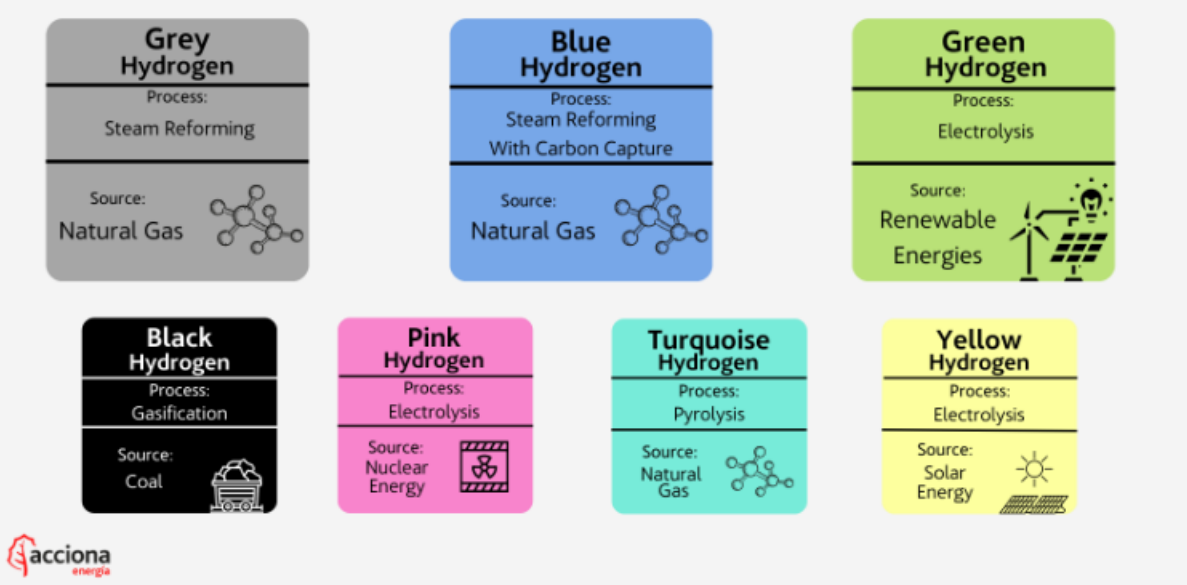

Figure 1.11: classification of hydrogen, through the process of production and the source [24]

As at the end of 2021, almost 47% of the global hydrogen production is from natural gas, 27% from coal, 22% from oil (as a by-product) and only around 4% comes from electrolysis. Electricity had a global average renewable share of about 33% in 2021, which means that only about 1% of global hydrogen output is produced with renewable energy. [25]

Hydrogen can be efficiently converted into electricity, and vice versa. It can be produced from renewable materials such as biomass and water, and most importantly, it is environmentally friendly at all processes utilizing hydrogen.

It is here that stands the advantage of using electrolyser, and it can be particularly interesting implementing this technology with the fuel cell, in order to store and convert H_2 to produce electricity from water. This is especially attractive considering the challenges that come out in the storage of hydrogen.

The main drawback of electrolysers regard the low efficiency in the electrolysis process, the necessity for some technologies to use rare metals, such as PEM, the most popular type of electrolysers nowadays (*section 1.5.2*). [26] Other technologies, such as solid oxide electrolysers, are very efficient and close to industrialization, but their high cost make this technologies still not spread.

In the most recent years, due to higher concerns around the CO_2 theme, the idea of exploit the carbon dioxide has been circulating, leading to the development of electrochemical

reduction of CO_2. This would permit to upgrade the carbon dioxide to value-added chemicals -green alternatives of fossil fuel-based products- and closing the carbon cycle. The reactions take the general form as follows:

$$xCO_2 + nH^+ + ne^- \rightarrow C_xH_{n-2y}O_{2x-y} + yH_2O$$

Equation 32

The different products that can be produce are, for example: CO, HCOOH, CH_3OH, CH_3COOH. [27]

1.4.1. Electrolysers efficiency

The efficiency of the electrolysers is calculated differently, considering the fuel entering.

In general, the operation of electrolysis is the reverse of the fuel cell reaction, so the efficiency calculations, therefore, can be inverted as well. There are different types of efficiency that can be determined: voltage efficiency ($\boldsymbol{\eta_V}$), electrical efficiency ($\boldsymbol{\eta_E}$), efficiency of H_2 production rate ($\boldsymbol{\eta_C}$) and cell efficiency ($\boldsymbol{\eta_{cell}}$)

Working with Steam Electrolysis and High-Temperature Cells, like SOEC, leads to consider in this condition, that the thermodynamics are significantly different, as the temperature climbs, the LHV (Lower Heating Value, the amount of heat released by fully combusting a specified quantity less the heat of vaporization of the water in the combustion product) of hydrogen increases and the Gibbs free energy decreases.

These high-temperature cells are considerably more efficient as they have lesser internal resistance losses and improved reaction kinetics as compared to their low-temperature PEM counterparts.

In the high-temperature case, calculating the voltage efficiency ($\boldsymbol{\eta_V}$) of the cell can be straightforward and the thermodynamic voltage can be used, calculated as E_a-E_c, where E_a and E_c are the potential of the anode and the cathode respectively.

$$Voltage\ efficiency_{(cell)} = \frac{Thermodynamic\ voltage\ (E)}{Operating\ voltage\ (V)}$$

Equation 33

A high-temperature electrolysis cell could operate below the thermoneutral voltage. In this case, the heat requirement must be made up by an external heat source. As the cell operated, the electrochemical reaction would withdraw heat from the cell components and cool the

cell to the point that it ceases operating. Therefore, to maintain temperature, sensible heat must be supplied to the cell components from an outside source.

In the case of electrical efficiency ($\boldsymbol{\eta_E}$), however, both the electrical input and the heat input from the external source must be included, otherwise the calculation produces a nonsensical answer and an efficiency that is greater than 100%. [28]

$$Electrical\ efficiency_{(system)} = \frac{HHV\ of\ H_2\ produced}{Electricity\ used + Heat\ supplied}$$

Equation 34

The measurement of hydrogen yield ($\boldsymbol{\eta_H}$) from the electrolysis cell is calculated in terms of electrical energy input: [23]

$$Hydrogen\ yield = \frac{HVV}{\Delta E} = \frac{HVV}{V \cdot i \cdot t}$$

Equation 35

Where *HVV* (Higher Heating Value), is the amount of heat released by fully combusting a specified quantity plus the heat of vaporization of the water in the combustion product, V is the cell potential (V), i is the current (A) and t is the time (s).

To calculate the cell efficiency ($\boldsymbol{\eta_{cell}}$), is calculated as:

$$Cell\ efficiency = \frac{Theoretical\ cell\ potential\ (V)}{Actual\ cell\ potential\ (V)}$$

Equation 36

Where the Nernst equation can be used to calculate the theoretical cell potential.

1.5. Electrolysers typologies

Electrolysers classification is based on their electrolyte and working temperature, as it can be seen in *Figure 1.12 and Figure 1.13*.

Thus, it is possible to differentiate the devices in two categories:

Low temperature Electrolysis (50-100°C):

- Alkaline Water Electrolysis (AEL)
- Proton Exchange Membrane Electrolysis (PEMEL)
- Anion Exchange Membrane Electrolysis (AEMEL)

High temperature Fuel Cells (700-1000°C):

- Solid Oxide Electrolysis (SOEC)

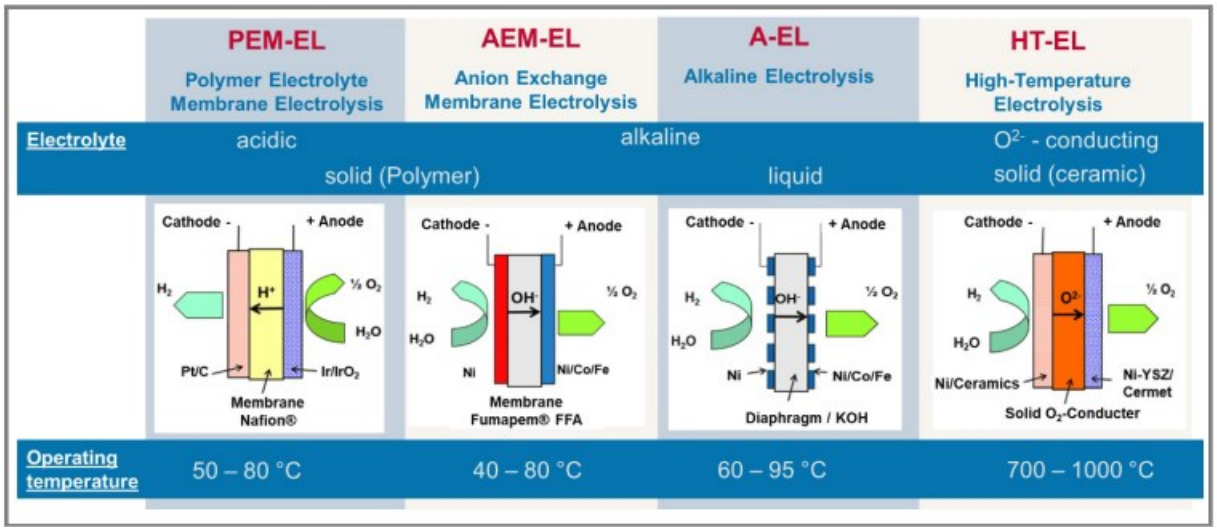

Figure 1.12: Electrolysers typologies [29]

	Alkaline	PEM	SOE	AEM
Electrolyte	Aqueous potassium hydroxide	PFSA membranes (e.g., Nafion)	Yttria Stabilises Zirconia (YSZ)	Anion exchange ionomer
Cathode	Nickel, Nickel - Molybdenum alloy	Platinum, Platinum - Palladium alloy	Nickel/YSZ	Nickel and Nickel alloys
Anode	Nickel, Nickel - Cobalt alloys	Ruthenium oxide, Iridium oxide	YSZ	Nickel, Ferrous, Cobalt oxides
Operating Temperature (°C)	60-80	50-80	500-850	50-60
Operating Pressure (Bar)	30	70	1-25	1-30
Stack Lifetime (h)	60-100k	20-60k	<10k	-
Technology Readiness	Matured	Commercialised	Demonstration	Large prototype
Cost	USD 500-1400/kW	USD 1100-1800/kW	USD 2800-5600/kW	

Figure 1.13: electrolysers classification [30]

1.5.1. Alkaline electrolyser (AEL) [23,29]

Alkaline electrolysers is a mature and commercially available technology, which has been introduced into the commercial market in the early 1900s. It presently accounts for almost two-thirds of the global electrolyser capacity. It operates via transport of hydroxide ions (OH^-) through the electrolyte, a liquid potassium hydroxide solution, from the cathode to

the anode with hydrogen being generated on the cathode side. The electrodes are usually made of Co, Ni or Fe. It is necessary the utilize of a separator, to better divide the gases which are produced at the electrodes -the most common is polymer-bonded zirconia.

Although current densities with up to 0.6 A cm^{-2}, pressure levels are low, the use of liquid electrolyte, which is corrosive and concern safety issue, and the high crossover of the gases, which lead to less pure hydrogen; the advantage of this cost-efficient technology lies in the long lifetime and the absence of expensive and rare catalyst materials. Efficiencies up to 65% are achieved.

The processes are:

Anode (+): $2OH^- \rightarrow H_2O + \frac{1}{2} O_2 + 2e^-$

Equation 37

Cathode (-): $2\ H_2O + 2e^- \rightarrow H_2 + 2OH^-$

Equation 38

overall process: $H_2O \rightarrow H_2 + \frac{1}{2} O_2$

Equation 39

1.5.2. Proton exchange membrane electrolyser (PEMEL) [23,29]

The Proton exchange membrane electrolyser (PEMEL) is one of the most popular electrolyser technologies. The technology of polymeric electrolyte is divide into:

- Proton exchange (PEMEL);
- Anionic exchange (AEMEL). (*Section 1.5.3*)

A PEMEL is constituted of the electrode (a *catalyst*, usually Ir and Pt, and a *GDL*, a gas diffusion layer, which act as collector, conductor and needs to be porous). The electrolyte is a membrane, usually Nafion®, that exchange cations, even though we are only keen on H^+, as already seen in *Section 1.2.1*.

One of the major advantages is the highly dynamic and fast response behaviour. Additionally, PEMEL offers high current densities and high stack efficiencies. Moreover, hydrogen can be produced at higher pressure levels for further usage like the refuelling process. On the downside, PEMEL needs cost-intensive and rare metal catalysts like

platinum and iridium. There is still potential concerning lifetime and plant size. Key figures are efficiencies up to 65% based on the lower calorific value and current densities up to 3 $A \cdot cm^{-2}$ for commercial products. Operating temperatures range between 50–80 °C.

The processes are:

Anode (+): $H_2O \rightarrow 2\ H^+ + \frac{1}{2}\ O_2 + 2e^-$

Equation 40

Cathode (-): $2H^+ + 2e^- \rightarrow H_2$

Equation 41

overall process: $H_2O \rightarrow H_2 + \frac{1}{2}\ O_2$

Equation 42

1.5.3. Anion exchange membrane electrolyser (AEMEL) [23,29]

In contrast to the PEMEL, the anion exchange membrane electrolysis (AEMEL), has an alkaline membrane as an electrolyte, composed of an aqueous potassium hydroxide (KOH) or sodium hydroxide (NaOH) and a polymeric membrane. The advantages of this technology are the low-cost catalysts, which reduce the system costs significantly. However, the major disadvantage of AEMEL is the low current density compared to PEMEL and short lifetime. As AEMEL is still in an early stage of development, the possibilities to increase current densities and lifetime are given. Today, there are only systems up to 5 kW with a system efficiency up to almost 70% available. Possible current densities go up to 2 $A \cdot cm^{-2}$ with an operating temperature from 40–80 °C.

The processes are:

Anode (+): $2OH^- \rightarrow H_2O + \frac{1}{2}\ O_2 + 2e^-$

Equation 43

Cathode (-): $2\ H_2O + 2e^- \rightarrow H_2 + 2OH^-$

Equation 44

overall process: $H_2O \rightarrow H_2 + \frac{1}{2}\ O_2$

Equation 45

1.5.4. Market distribution [31]

The global electrolysers market was valued at $3 billion in 2022, and is projected to reach $34.4 billion by 2032, growing at a CAGR (Compound Annual Growth Rate) of 27.2% from 2023 to 2032.

Electrolysis capacity is expanding from a modest starting point and must accelerate substantially to align with the Net Zero Emissions by 2050 (NZE) Scenario, which calls for installed electrolysis capacity to exceed 550 GW by 2030. In addition, some governments to give a boost to electrolyser business, thanks to some new policies.

The electrolyser market is divided into: AEL, PEMEL, AEMEL, and SOEC. As we can see from *Figure 1.14*, the Alkaline Electrolyser dominate the market in 2022, but SOEC has projected to dominate the growth for the period 2022-2032. In fact, the high operating temperature leads to higher efficiency, consistent to what is required by the industries nowadays. In addition, the higher push done by the government and the experts for the use of hydrogen as a clean and adaptable energy carrier, will accelerate the spread of technology that are able to produce hydrogen on-site, like SOECs.

Figure 1.14: electrolysers market distribution 2022 and projected in 2032 [31]

1.6. Solid Oxide Electrolysis Cell (SOEC) [23]

As we have just seen, Solid Oxide Electrolysis Cells (SOECs) are very promising for the future. A SOEC consists of a dense electrolyte layer in the middle and a porous cathode -

state-of-art material is Ni/YSZ- and anode -state-of-art material is LSCF or LSM. The electrolyte conducts oxygen ions between the electrodes, block the electronic conductance, and separate the oxidizing gas from reducing gas. As the SOEC operates at higher temperatures, some devices need a sealing material, that acts to prevent oxidation and reduce gas leakage, has a thermal expansion coefficient that matches the rest of the device, and has good physical and chemical stability at high temperatures.

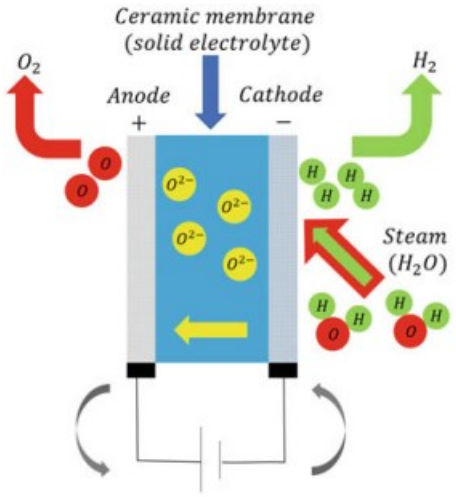

Figure 1.15: SOEC scheme [23]

All the processes that take place in the device is:

Anode (+): $O^{2-} \rightarrow \frac{1}{2} O_2 + 2e^-$

Equation 46

Cathode (-): $H_2O + 2e^- \rightarrow H_2 + O^{2-}$

Equation 47

overall process: $H_2O \rightarrow H_2 + \frac{1}{2} O_2$

Equation 48

SOECs present some advantages over the standard electrolysers, such as:

- their low internal resistances, that allow high production rates at low voltages;
- requirement of less electrical energy;
- high efficiency for electrolytic hydrogen production;
- high purity of the produced hydrogen;
- operating at high current densities;

- possibility of co-electrolysis and to work as reversible Solid Oxide Cells (r-SOCs, further information in *Section 1.7*)

These devices are also useful from the pollutants point of view for two main reasons; in fact, they would possibly replace the actual way to produce hydrogen via methane steam reforming, thus reducing the vicious cycle of pollutants emission, and they can be used for the co-electrolysis of CO_2 with steam, as mention in *Section 1.4*, allowing the possibility to produce C-based chemicals, enhancing its value and converting it in a more valuable chemicals and fuels. Moreover, it has been studied the possibility of using ammonia (NH_3) for chemical storage, in particular, through r-SOCs electrochemistry, H_2 is produced from ammonia (during SOFC phase) and then can later react with N_2 to convert in NH_3 during the SOEC phase.

The flexibility of the incoming fuel is surely advantage of SOECs, which is why they have been considerably studied lately.

However, they have multiple drawbacks, like the high operating temperature (750-1000°C), limited useful life 10.000-20.000 h in commercial systems, and low technologic development, which is the reason why the investment costs are very high.

1.6.1. Cell components: the anode (oxygen electrode) [23]

The oxygen electrode, i.e. the anode, has a key role in the SOEC system. Increasing the OER (Oxygen Evolution Reaction) activity is one of the significant parameters for improving the electrochemical catalytic performance. The main properties of the SOEC oxygen electrode should include high electronic/ionic conductivity and catalytic activity for the OER, chemical compatibility, and stability with electrolytes materials.

Here, the reaction that takes place is the oxidation of O^{2-} that spread out from the electrolyte into O_2.

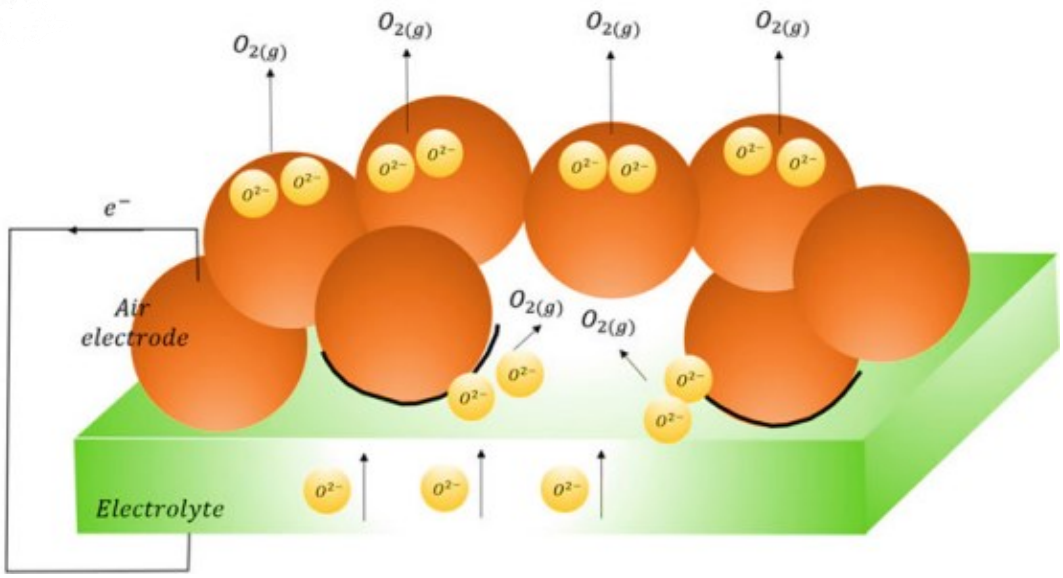

Figure 1.16: the oxygen electrode [23]

There are multiple electrodes used as anode, such as:

I. *The Metal electrodes*: only noble metals like Pt or Au can be used;
II. *Ceramic Electrode materials*: the state-of-art perovskites (La,Sr)(Co,Fe)O_3-based (LSCF) and $La_{0.8}Sr_{0.2}MnO_3$-δ-based materials (LSM) with optimized microstructures (particle size and volumetric content in single layers) to reduce polarization resistance and enhance durability. In the case of LSCF, the structure is a La-ferrite doped with Sr and Co, in order to enhance the ionic and electronic conductivity of the material. This occurs because Sr on the A site lattice of LSCF acts as an acceptor, enhancing the oxygen vacancy formation, and Co ions on the B site lattice have a smaller binding energy for oxygen than that with Fe ions, increasing the electronic conductivity. [32]

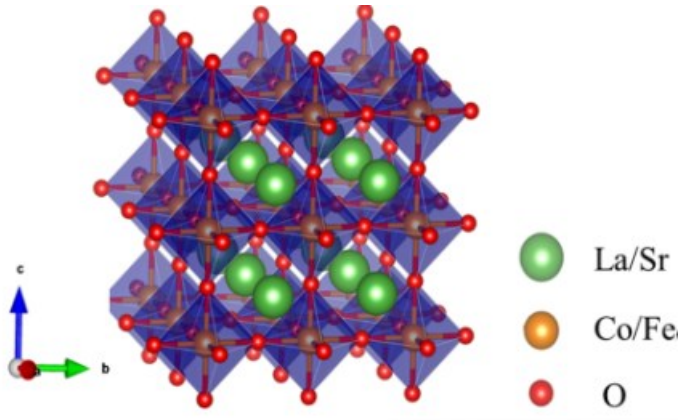

Figure 1.17: crystal structure of LSCF [32]

III. *Composite electrodes*: they can be generally classified into two types: ceramic-metal composite electrode (Ni-YSZ, Ni-SDC, LSCM-Cu, etc.) and ceramic-ceramic electrodes (LSC-YSZ, LSM-YSZ, etc.)

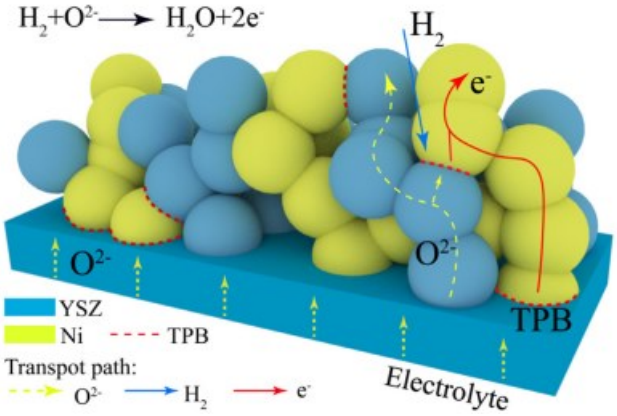

Figure 1.18: Ni-YSZ electrode[23]

1.6.2. Cell components: the cathode [23]

The morphology and composition of the hydrogen electrode, i.e. the cathode, play an important role in the efficiency of water electrolysis, as it is the place where the decomposition of H_2O takes place and where the supplied electrons travel from the interconnectors to the electrolyte/electrode interface, allowing oxygen ion reactants to be transported through the electrolyte.

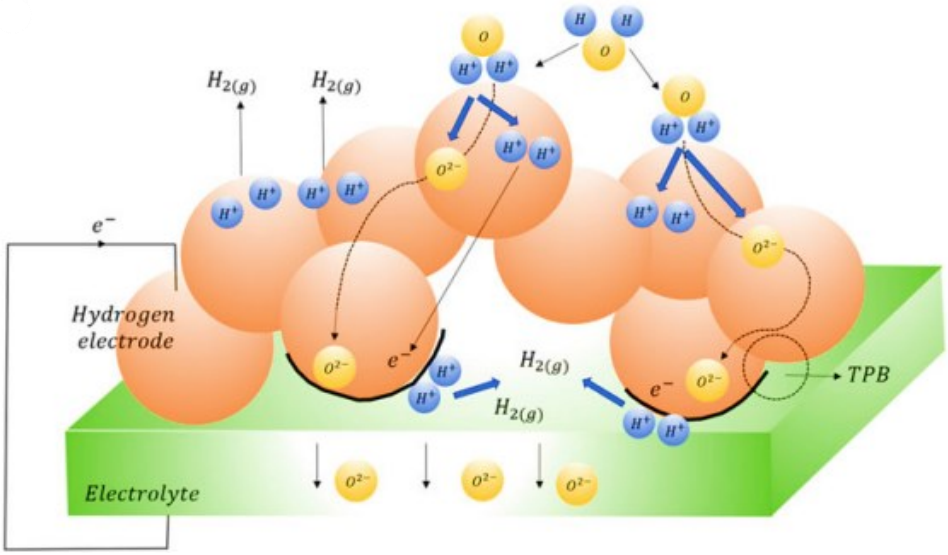

Figure 1.19: the hydrogen electrode [23]

The state-of-art materials are ceramic-metal (cermet) material, composed of Ni-based composite materials with Yttria Stabilized Zirconia (YSZ) and Yttrium-doped Barium cerate

zirconate. They are excellent oxygen ion and proton conductors, have low cost compared to noble metal, good electrochemical activity, chemical stability, and matching thermos-mechanical expansion coefficient with the other components. However, the Ni-based composite materials tend to agglomerate and degrade the performance under long-term SOEC operations. Lately, perovskite-based mixed oxide has gained interest as new class used as hydrogen electrodes.

1.6.3. Cell components: the electrolyte [23]

The solid electrolyte is the central component of the SOEC system, with its properties—such as conductivity, stability, thermal expansion coefficient, and sintering temperature—not only directly influencing the electrolytic cell's performance but also determining compatible electrode materials and fabrication methods.

It has basically three functions:

I. To conduct oxygen ions or protons between the electrodes,
II. Block electron conductance,
III. Separate the produced gases.

In order to allow all of these functions, it is necessary for the electrolyte to have high ionic conductivity and negligible electronic conductivity, to have compatibility with the electrode material in mechanical and chemical properties from room temperature to operating temperature (usually above 800°C).

There are three types of electrolyte:

I. *Oxygen ion-conducting type*: Zirconia (ZrO_2)-and ceria (CeO_2)-based materials and their derivates, such as YSZ; Ceria-based electrolytes have higher ionic conductivity than a YSZ-based at intermediate temperature (500-800°C). Lately, perovskite oxides ceramic materials are explored as oxygen ion-conducting electrolyte.
II. *Proton-conducting type:* the perovskite oxides ceramic material, such as barium cerate ($BaCeO_3$)-based and zirconate ($BaZrO_3$)-based electrolytes are investigated as proton-conducting

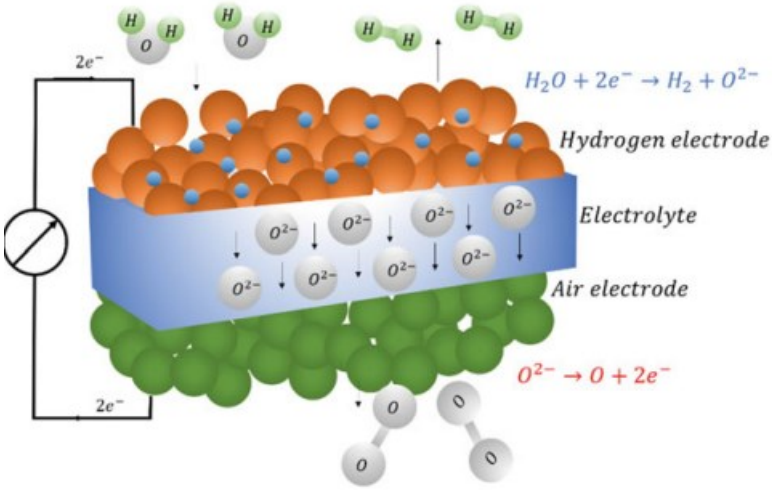

Figure 1.20: Oxygen ion-conducting electrolyte [23]

1.6.4. SOEC challenges

SOEC technology presents a promising method for producing pure hydrogen in a clean and sustainable way; however, considerable progress is necessary for broad commercial adoption. Currently, advanced SOECs require high operating temperatures and are expensive to produce and market. Thus, this technology has high issues, including not only the high operating temperature, but also the oxygen partial pressure and overpotential. Moreover, there are some problems related to the stability and the long-term operation. Thus, extensive efforts are needed to develop new materials that can lower operating temperatures and reduce production costs while preserving the device's performance and structural stability.

1.7. Reversible Solid Oxide Cells (r-SOCs)

Reversible solid oxide cells (r-SOCs) technology has become a focus in the world for its high energy storage efficiency, environmental friendliness, low development cost, and high market conversion rate.

The strong point of this technology is the interchangeability between electrical and chemical energy according to people and production needs. It integrates the functions of power generation and energy storage, switching between the SOFC and SOEC modalities.

Imaging it as a type of battery, it is charged during the electrolysis cell operation and discharged during fuel cell operation. [1]

As soon as the electricity is needed, the H_2 stored and produced by SOEC modality could be converted.

From the beginning of 1900 it has been studied the electrolysis of both H_2O and CO_2 (in liquid phase), lately it has been investigated more the reduction of CO_2 to CO in gas phase and even the co-electrolysis of CO_2/ H_2O.

Generally, the performance of CO_2 electrolysis was significantly inferior to that of H_2O electrolysis because of the lower diffusion rate of CO_2 and higher activation energy of CO_2 reduction. In comparison to pure CO_2 electrolysis, co-electrolysis showed a lower activation energy, lower polarization resistance, and faster electrochemical kinetic.

Mixture of CO_2+H_2O+H_2 was always injected into the cathode of SOEC, where H_2 was indispensable for cathode protection. Syngas with tuneable ratio of H_2 /CO can be acquired in the outlet. Meanwhile, O_2 was produced at the side of anode. [33] The possible reactions occurred during co-electrolysis were showed as follows:

Cathode:

$$CO_2+2e^- \rightarrow CO+O^{2-}$$

Equation 49

$$H_2O+2e^- \rightarrow H_2+O^{2-}$$

Equation 50

$$H_2 + CO_2 \rightleftharpoons H_2O + CO \text{ (RWGS reaction)}$$

Equation 51

Anode:

$$O^{2-} \rightarrow 1/2\ O_2 + 2e^-$$

Equation 52

During the co-electrolysis both of the *Eq. 49 and 50* could compete and occur, which are the electrochemical reduction of the starting material. Except for electrochemical reduction, the thermochemical reaction of Reverse Water Gas Shift Reaction (RWGS reaction, *Equation 51*) is parallel, making the real reaction processes complicated. [33]

The overall processes, if we work with the co-electrolysis of CO_2 and H_2O, are:

Table 1.1: the electrochemical processes in a reversible Solid Oxide cells (r-SOCs)

		SOFC		**SOEC**
Oxygen electrode	Cathode (+)	**$1/2\ O_2 + 2e^- \rightarrow O^{2-}$**	Anode (+)	**$O^{2-} \rightarrow 1/2\ O_2 + 2e^-$**
Fuel electrode	Anode (-)	**$CO + O^{2-} \rightarrow CO_2 + 2e^-$** **$H_2 + O^{2-} \rightarrow H_2O + 2e^-$**	Cathode (-)	**$CO_2 + 2e^- \rightarrow CO + O^{2-}$** **$H_2O + 2e^- \rightarrow H_2 + O^{2-}$**

As it has seen from the table, the cathode in SOFC corresponds to the anode in SOEC and the processes that happen in their compartment are exactly the opposite.

Clearly, to make this technology more sustainable, the electric energy needed by the SOEC technique could be the surplus energy from nuclear reactors and renewable energy as well as the waste heat from production and life, and can be used to convert water vapor/carbon dioxide into hydrogen/carbon monoxide with high efficiency, which is indeed the main aim of this project. [34]

The SOFC-based high-temperature power generation technology or combined heat and power technology can efficiently convert the chemical energy in the stored hydrogen/carbon monoxide into clean electricity and heat, which can be used as distributed energy for community houses, buildings, and corporate data centres.

The efficiency of this kind of chemical energy storage technology that uses hydrogen energy as an energy carrier is not restricted, as already mentioned, by the Carnot cycle. It is mainly determined by the energy conversion efficiency of electrolytic hydrogen production technology and fuel cell technology; the highest conversion efficiency can reach more than 90%. [34]

The following graph compare the specific power (a measure of power generated by the engine divided by the mass, defined as: $Specific\ Power = \frac{Power\ (W)}{mass\ (kg)}$), *Equation 53*

versus the Power Density (a measure of how fast a device can deliver energy, $Power\ Density = \frac{Power\ (W)}{Volume\ (m^3)}$), *Equation 54*

underlining that SOFC is an attractive technology concerning how much power is generated and how fast the energy is delivered.

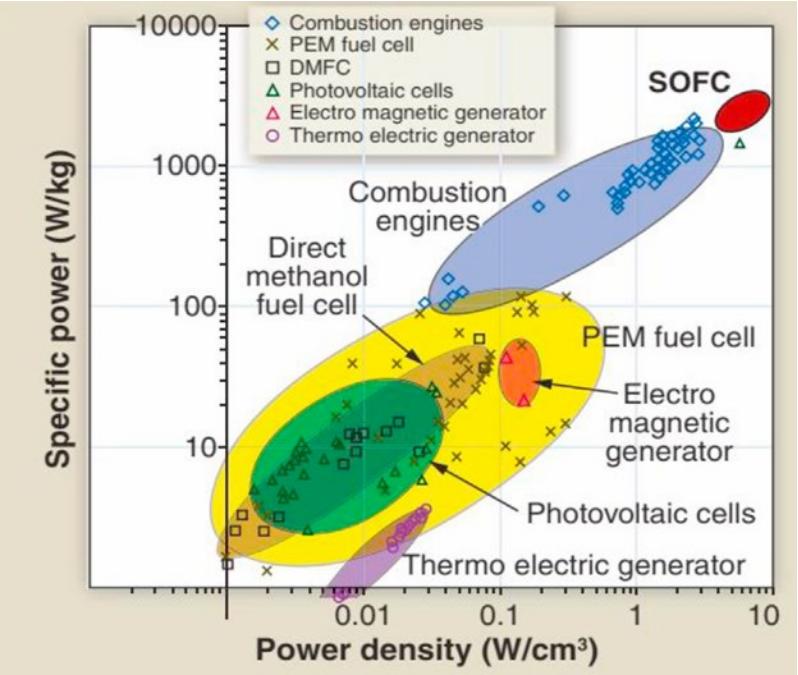

Figure 1.21: Combined graph of I-V and Power density for different technologies [34]

Talking about the cell materials, as already expose above, the requirements are not different to what is required by SOFC and SOEC technologies alone.

The electrolyte should have higher density, higher ionic conductivity and lower electronic conductivity, higher structural stability, high thermal expansion matching and isolate the gases in the gas chamber.

For what concern the electrodes, they should have higher porosity, higher ionic and electric conductivity, fine chemical compatibility, higher electrocatalytic activity to oxygen (in case of oxygen electrode) or fuel gas (in case of fuel electrode), be stable in both oxidizing and reductive atmosphere. [34]

For this type of device, several materials have been tested as:

- *Oxygen electrode*: ABO_3 Perovskite material, $AA'B_2O_{6-x}$ Double Perovskite or A_2BO_{4+x} Ruddlesden-Popper material
- *Electrolyte*: Oxygen ion (Zirconium based, Cerium based or perovskite materials) or Proton conductive materials (ABO_3 perovskite structure oxide, Spinel, Composite material)
- *Fuel electrode*: Ni-based or Cu-based composite material, ABO_3 Perovskite material

2. CO_2 [35]

2.1. Decarbonization [8,36]

The theme of decarbonization has been already mentioned in the Introduction. However, it should be significant to underline some data and facts in order to better understand the size of the theme that in this thesis is examined in depth.

"*The climate crisis remains the defining challenge of our time*" is the sentence that open the document from the European commission, dated 2020, which has the aim to step up Europe's 2030 climate ambition.

The past five years were the warmest on record. Global average temperature increased by 1.1°C above pre-industrial levels by 2019, and this leads to the need of all sectors of economy to decarbonize by 2050. The impact of climate change is beyond dispute, with droughts, storms, and other weather extremes on the rise, as we have unfortunately dealt with lately. Some national cases are floods, that has been experienced every other month in precise zone of Italy, like Veneto, Sicily and Emilia Romagna region. Mentioning some international examples, the so-called biggest hurricane Milton, that hit Florida on October 2024. Clearly, we are facing an emergency and we should do anything possible in our hands.

The European Green Deal, approved in 2020, sets some policies in order to reach the climate neutrality by 2050, in which an intermediate step is achieving 55% greenhouse gas emissions reduction by 2030. The analysis demonstrates that the achievement of the target is possible in a responsible and socially fair manner, explaining that the citizen themself are a key points. In fact, they can support and contribute to the question, only if they are really aware of the importance of it.

Buildings and transport are, alongside industry, the main energy users and source of emissions. Decarbonizing both energy supply and demand is key to becoming climate neutral and can actually be achieved while enhancing the well-being of citizens drawn from transport and housing.

The building sector represents the 34% of energy-related emissions in 2022, as shown in *Figure 2.1*. These emissions are both part from the direct use of fossil fuels in buildings (e.g.

oil and gas used in boilers for heating) and from the production of electricity and heat for use in buildings (e.g. electricity consumed by water heaters, lighting, electrical devices, etc.) The GHG fell by 34% between 2005 and 2022 thanks to some strategies, driven by the European Governance and the national governments, that push to the electrification in the residential sector, decarbonisation of the electricity and heating/cooling sectors, and improvements of energy efficiency in buildings. [37]

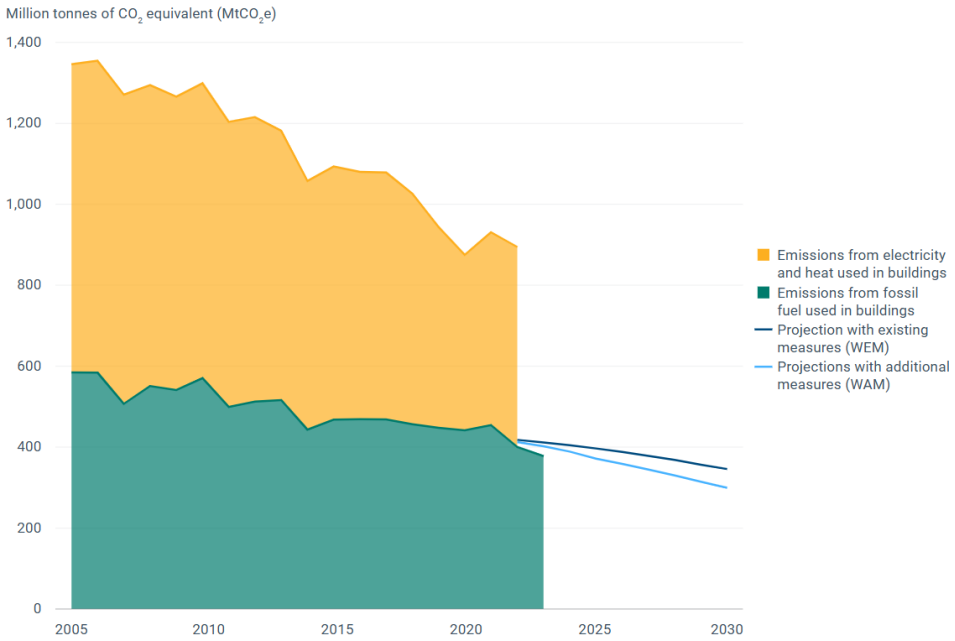

Figure 2.1: CO_2 emissions in building sector [37]

Renovate buildings not only lowers energy bills and greenhouse gas emissions, but it also improves living condition and creates local jobs.

For what concerns the transport in Europe, the emissions dropped drastically in 2020 because of COVID-19 pandemic (*Figure 2.2*). Preliminary estimates of emissions in 2021 indicate a rebound of 8.6% in transport, followed by further growth of 2.7% in 2022. The European Environment Agency (EEA) indicate that domestic transport emissions will only drop below their 1990 level in 2032. International transport emissions (aviation and maritime) are projected to continue increasing. [37]

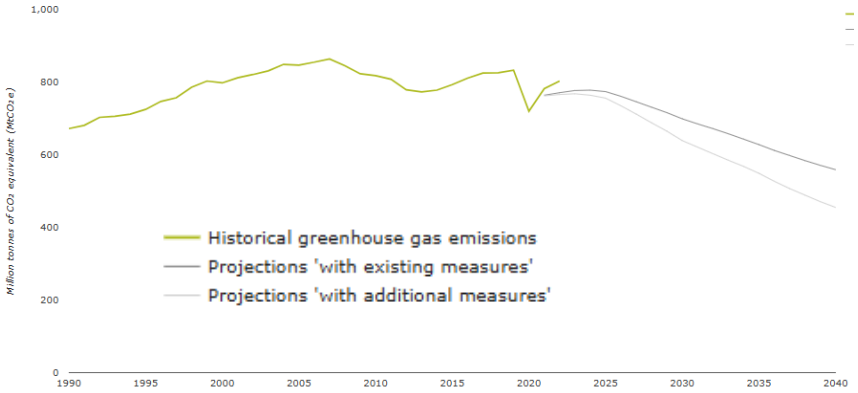

Figure 2.2: CO_2 emissions in transport sector [37]

2.2. Reduction of CO_2

There are different ways to reduce CO_2 emissions, through multiple Carbon Capture and Utilisation (CCU) pathways. Some of these are:

I. The production of chemicals and fuels from CO_2
II. The utilization of microalgae, to fix CO_2 at high efficiencies and then processing the biomass
III. The use of CO_2 to 'cure' the cement, as a building material
IV. The injection of CO_2 into oil wells, in order to increase the production of oil. It is called 'CO_2-enhanced oil recovery (EOR)'.
V. Land management techniques for soil carbon sequestration, to store CO_2 and enhance agricultural yields.

The reduction of CO_2 is the method tested along this thesis. There are different ways that allow the reduction: thermocatalysis, electrocatalysis and photocatalysis.

The thermocatalytic pathway is straightforward to scale for industrial applications; however, certain reactions face limitations due to kinetics and/or thermodynamic equilibrium constraints (it usually works at 100-500°C and 1-100 bar, respectively). In contrast, while the electrocatalytic approach is less developed, it offers advantages such as operating at higher temperatures and pressures that overcome the activation barrier and accelerate the reaction rate, utilizing water as a hydrogen source, and avoiding thermodynamic equilibrium limitations. Nonetheless, advancing electrocatalysis requires the development of more efficient and stable electrocatalysts. [38]

One of the latest research direction is thinking of working with a tandem system, including electrocatalytic-thermocatalytic or thermocatalytic- electrocatalytic reaction.

For example, CO_2 can be reduced to syngas (CO and H_2, where H_2 is generated in a side reaction) via electrocatalytic approach and the syngas is further converted to higher products such as C3 oxygenates via thermocatalytic approach. In theory, this tandem system can also be a thermocatalytic process followed by electrocatalytic process. The approach chosen for this thesis is the first mentioned, with an electrochemical reduction of CO_2 and H_2O syngas (CO and H_2), which could be followed by thermocatalytic Fischer-Tropsch synthesis to petroleum-like product.[38] The so-called process is co-electrolysis, deeply described in *Section 1.7* and that receive an important boost recently, moved by the necessity of a more sustainable energy, the need of reduce greenhouse gas emissions and the requirement from citizens to have energy at lower price.

3. PEROVSKITE MATERIALS

Perovskite oxide materials represents nowadays the state-of-the-art materials for electrodes in a Solid Oxide Fuel Cell and Solid Oxide Electrolysers, but their history is not so recent. In fact, their first discover is dated back in 1839, when Gustav Rose found a calcium titanium oxide mineral of formula $CaTiO_3$ in the Ural Mountains, naming it after the Russian mineralogist Lev Alekseevich Perovski (1792-1856). Since then, the materials that present the same crystal structure were named perovskites.

3.1. Crystalline structure

A perovskite structure is a substance that has the generic from ABO_3 and the same crystallographic structure as perovskite.

The simplest way to conceive a perovskite structure is to have a large atomic or molecular cation (positively-charged) of type A in the centre of a cube. The corners of the cube are then occupied by ions of the type B (also positively-charged cations), and the faces of the cube are occupied by the anion X (Oxide ion) with a negative charge.

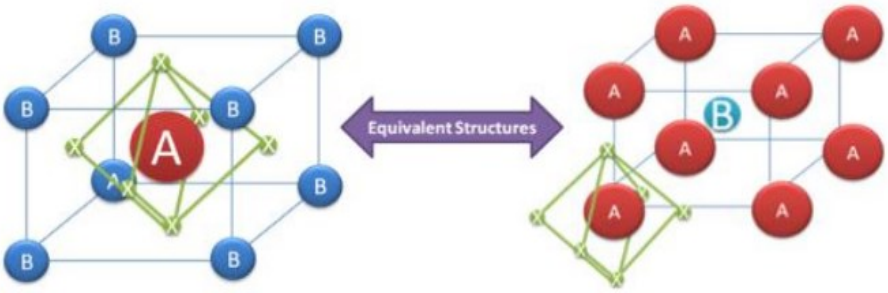

Figure 3.1: crystal structure of an ABO_3 perovskite [96]

The structure can be also described as if the A-atom (Sr in the case of *Figure 3.2*) is coordinated to 8 B(Ti)-atoms at corners of the cube and 12 X atoms (oxygen) at the centre of the cell edges.

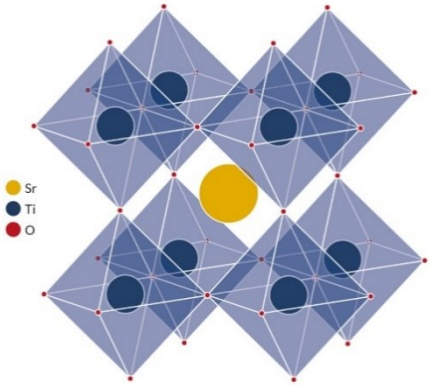

Figure 3.2: Other configuration of crystal structure of an ABO_3 perovskite [97]

The perovskite structures exist in different forms such as: ABO_3-perovskite (ex: $BaTiO_3$, $CaTiO_3$), A_2BO_4-Layered perovskite (ex: Sr_2RuO_4, K_2NiF_4), $A_2BB'O_6$-Double perovskite (ex: Ba_2TiRuO_6) and $A_2A'B_2B'O_9$-Triple perovskite (ex: $La_2SrCo_2FeO_9$). [39]

It is noteworthy that the ideal cubic perovskite is not common in nature and the mineral perovskite is itself slightly distorted; this is principally due to size effects, deviations from the ideal composition and the Jahn-Teller effect.

Regarding the size effect, Goldschmidt introduced for the first time the concept of the "tolerance factor", which is an indicator for the stability and distortion of crystal structures. It is calculated as:

$$t = \frac{r_A + r_O}{\sqrt{2}(r_B + r_O)}$$

Equation 55

where r_A, r_B and r_O are, respectively, the ionic radii of the A-cation, B-cation and oxygen ion. The ideal cubic perovskite, strontium titanate ($SrTiO_3$), is characterized by a tolerance factor of 1.00, since r_A = 1.44 Å, r_B = 0.605 Å and r_O = 1.40 Å.

In practice, there is some flexibility over bon lengths and usually, a cubic perovskite forms with t in the range $0.9<t<1.0$. For $t>1$, the B site is larger than required, the structure distorts but is still basically a perovskite as in $BaTiO_3$. For smaller tolerance factors ($0.85<t<0.9$), several different kinds of structural distortions occur, where A-site is too small for the site.

These distortions generally involve tilting and rotation of the BO_6 octahedra, as shown in *Figure 3.3*.

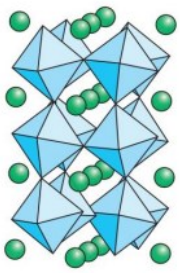

Figure 3.3: Tilting and rotation of BO_6 octahedra, due to small tolerance factor [98]

The change in composition can be the result of a thermal treatment in an oxidizing or reducing atmosphere, that causes the change in oxygen content of the entire structure. As a result, a defective perovskite can be produced, characterized by different properties with respect to the stoichiometric one.

The Jahn-Teller effect is due to some active ions in the B site, as a results of strong electron interactions between the partially filled d-orbitals in this cation. This effect is a mechanism of spontaneous symmetry breaking in both solid state and molecular systems, as B-site cations are always surrounded by six nearest neighbour oxygen anions, that due to the Coulomb repulsion between the 'd' orbital electrons and the surrounding charges from oxygen, change the energy of the orbitals, causing an elongation of the BO_6 octahedra to decrease symmetry. [39]

3.2. Perovskite properties

Perovskites are unique today among all the known solid-state materials with a variety of applications contrasting in a property like highly resistive (positive temperature coefficient materials) to highly conducting materials (superconductor). From the electronic point of view, these materials are mostly showing dielectric and ferroelectric properties, thanks to easy chemical manipulation in the composition. Some of them, like $SrRuO_3$, shows ferromagnetism.

Nearly all the elements can be included in the perovskite structure, and since this structure tolerates partial substitution at both the cationic sites and several anions can be placed in the perovskite composition, the number of materials that can be obtained in perovskite composition appears to be significant in numerous applications. [39]

Notable are the properties of conductivity and stability of perovskites making them ideal for SOFC and SOEC applications, both as electrodes or electrolytes. Nonetheless, there are some challenges still to overcome, as the operating temperature and the high costs of some of these materials, already mentioned above in *Section 1.3.4 and 1.6.4*.

3.3. Double perovskite materials

The double perovskites are composed of two simple perovskite structures, ABO_3 and $AB'O_3$, so the general chemical formula is $A_2BB'O_6$ (where A is an alkaline-earth or rare-earth ion, B and B'-sites are alternately occupied by the transition metal, like Co, Fe, Ni and Mn). The two simple perovskite structures are located in two alternating face-centred cubic sublattices, achieving rock salt ordering between these cations. The octahedral voids are occupied by A-cations, as shown in *Fig. 3.4*. [40]

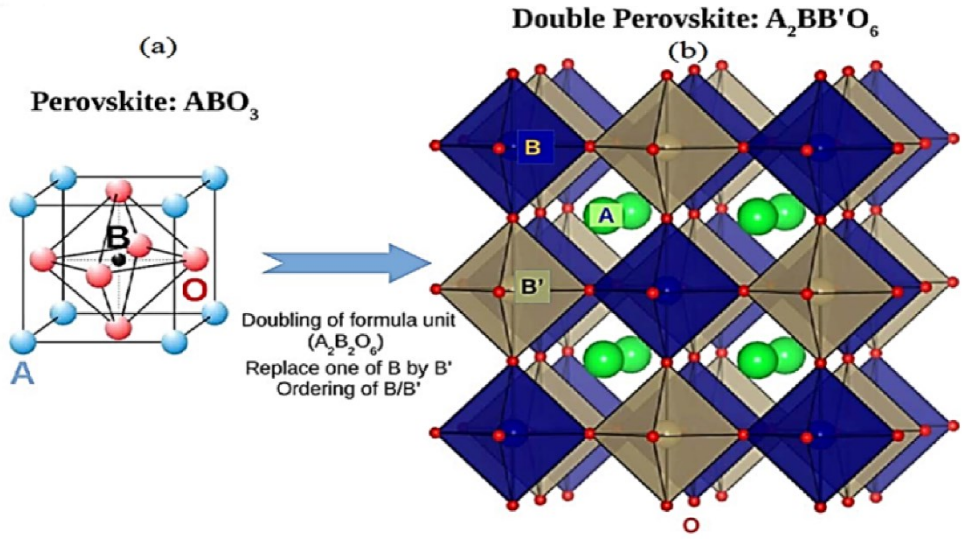

Figure 3.4: the schematic representation of: a)perovskite and b)double perovskite [99]

Factors involved in the double perovskites ordering are the differences in cation oxidation states and ionic radii.

In the case of double perovskite with an A^{2+} the total oxidation of the B site will be eight, that can be B^{4+}/B^{4+}, B^{3+}/B^{5+}, B^{2+}/B^{6+} and B^{+}/B^{7+}.

The crystallographic structure of ABO_3 can be calculated through the tolerance factor (*Eq. 55*), but the ionic radius of the cations (r_A, r_B and $r_{B'}$ are, respectively, the ionic radii of the A-cation, B-cation and B'-cation) should be taken into account in the case of double perovskite, as following:

$$t' = \frac{r_A + r_O}{\sqrt{2}(\frac{r_B + r_{B\prime}}{2} + r_O)}$$

Equation 56

From the tolerance factor, it might be predicted the crystal system of the compound. [41]

Every double perovskite has its own peculiarities, due to the elements chosen to compose it. The possibility of choosing every element from the periodic table is surely interesting and promising for the future.

Cobaltites and manganites-based perovskites have drawn attention because of their phases, dieletric, magnetic, and electronic properties. Moreover, lanthanide (Ln)-containing oxide materials doped with alkaline elements (Ba, Sr, Ca, etc.) and transition metals (Cr, Mn, Fe, etc.) have good and promising electronic and ionic conductivity, attractive for their use as electrodes in SOFC and SOEC. However, these materials still exhibit slow oxygen transportation kinetics, specifically at intermediate temperatures.

In general, the presence of B and B' redox active elements bring to high electron transport, so, usually, the choice of B and B' is made in order to ensure the electronic conductivity.

For example, B and B' of $SrFeMoO_6$ (SFM 1:1) double perovskite shows several different oxidative states, as Fe could have +2, +3, +4 and Mo +5, +6; which is also the reason that explain why this compound has high chemical stability, both in reducing and oxidative atmospheres. Then, it shows high conductivity (from 100 to 300 S cm^{-1} at 800 °C), as it has a metallic type of conductivity. Moreover, in the most studied iron-containing molybdate material ($Sr_2Fe_{1.5}Mo_{0.5}O_{6-x}$, SFM 1.5:0.5), the oxygen vacancies are mainly transported through the Fe-O-Fe bonds instead of the Mo-O-Fe and Mo-O-Mo bonds; at the same time, the Fe-O bonds are relatively weak, contributing to a high level of oxygen conductivity.

In addition, these materials prevent carbon deposition due to carbon interaction with the lattice oxygen, and low poisoning by sulphur and methane is registered.

All these characteristics -high electronic and oxygen conductivity, adaptability to different fuels, stability in both reductive and oxidative atmospheres- make this material particularly interesting for its use as electrode in Fuel Cells or Electrolysers, which is also the reason why they have gained interest lately. [42]

4. SYNTHESIS AND CHARACTERIZATION OF SFM MATERIALS

The following chapter will be dedicated to the description of the main synthesis routes to obtain double perovskite materials, with a focus on the approach that has been used in this work, the so-called Pechini route.

Subsequently, all the characterization performed on the obtained powders (XRD, H_2-TPR, SEM, EDX, BET and XPS) will be presented and the obtained results discussed.

4.1. Main synthesis routes

Double perovskites are usually prepared with the same approaches commonly used for the synthesis of perovskites, through solid-state or liquid-state synthesis. It is important to find the proper way of synthesizing the material, as perovskites are strongly synthesis route dependent.

4.1.1. Solid-state synthesis [43]

Solid-state synthesis technique is used to produce polycrystalline materials. It is also known as ceramic method because most of the ceramics are synthesized by this method. This method requires raw materials in carbonates and/or oxides forms, the raw materials do not react chemically to each-other at room temperature, but they go through mechanical grinding and mixing, usually done by ball milling. When the mixture of raw materials is heated at very high temperatures (i.e., 700–1500°C), the chemical reaction takes place at a significant rate.

This kind of treatment is easy to perform and relatively cheap, but the presence of impurities inside the materials is difficult to control. Moreover, it is difficult to reach a good homogeneity of the final product.

4.1.2. Liquid-state synthesis

Differently from the solid-state synthesis, the liquid-state synthesis involves the utilization of precursors, such as nitrates, acetates, or oxalates, which are dissolved in a liquid and the precipitation of the precursor oxides is induced by pH or temperature changes.

One of the most utilized methods is the wet chemistry synthesis, which is usually carried out in water, thus only water-soluble precursors can be used.

The choice of using water is better for the environment and safer for the technician (compared to toxic solvents). The advantage of the liquid-state approach over the solid-state one is a better control of the precursors that lead to a more homogeneous product, characterized by the exact desired stoichiometry. Then, the operating temperature is lower compared to solid-state synthesis. Finally, the method is simple and does not required sophisticated laboratory infrastructure facilities.

One of the most popular synthesis approach, due to its simplicity and versatility, is the Pechini method (*Section 4.2*), which has three steps: [44]

I. Aqueous dissolution of precursors
II. Drying and heating of the solution obtained and formation of a polymeric resin
III. Decomposition of the precursor material to obtain an oxide powder

4.2. Powder synthesis: Pechini route

Two materials, with different stoichiometry, have been synthesized, through the Pechini route:

- Sr_2FeMoO_6, called SFM 1:1
- $Sr_2Fe_{1.5}Mo_{0.5}O_6$, called SFM 1.5:0.5

The choice of two materials is due to the will of studying their different behaviour related to the amount of Fe and Mo integrated. In particular, to examine how much the activity of the two electrodes is correlated to a higher quantity of Fe and lower of Mo.

This method implies the utilization of:

- Metal precursors of the corresponding cations
- Citric Acid (CA, $C_6H_8O_7$) and ethylene glycol (EG, $C_2H_6O_2$), as chelating agents
- Nitric acid (HNO_3)

Citric acid is particularly suitable for this aim considering that it is a weak organic acid with three carbonyl groups that can act as anchoring points for cations; in addition, its middle carboxylic acid group is the most acidic due to the electron withdrawing power of the alpha -OH group and hence the formation of the strongest complexes. [44] The use of ethylene glycol promotes homogeneity of the final oxide and results in a highly cross-linked gel. The gel structures can be varied depending on the acid-to-alcohol ratio. The main advantage of using this synthesis route stands in the temperature, as the organic components are eliminated as low as at 300 °C, and its relatively low cost. [44]

In this work, the used metal precursors were:

- $Sr(NO_3)_2$, Sigma Aldrich, >99%
- $Fe(NO_3)_3 \cdot 9H_2O$, Sigma Aldrich
- $(NH_4)_6Mo_7O_{24} \cdot 4H_2O$, Sigma Aldrich, >99%

These compounds were weighed considering the stoichiometry that each material has to respect, calculated considering that in the sample SFM 1:1, the molar ratio between Fe and Mo is 1:1. Correspondingly, in the sample SFM 1.5:0.5 the molar quantity of Fe is 3 times the quantity of Mo.

These compounds were solubilized separately in water keeping the solutions at 125 °C and under continuous stirring, some drops of nitric acid are added and then all inserted in the same beaker, with the addition of citric acid and ethylene glycol. The ideal ratio between cations, citric acid and ethylene glycol has been found to be 1:1.9:6 from previous attempted synthesis.

The addition of nitric acid should be small and just in order to better solubilize each precursor and avoid undesired precipitation phenomena.

The solution was then basified to pH 7 via drop-wise addition of ammonium hydroxide. At that point the stirring was stopped and the solution was maintained at 180 °C, allowing the complete evaporation of water and inducing the formation of a gel phase, that was later burnt through an auto-combustion process at about 350 °C.

To eliminate residual organic compounds and to induce the formation of the right double perovskite phase, a calcination treatment at 900°C for 4 hours and reduction treatment (the reaction atmosphere was 5% H_2/H_2O) at 900°C for 8 hours, both with a heating and cooling ramp of 5°C/min, have been carried out.

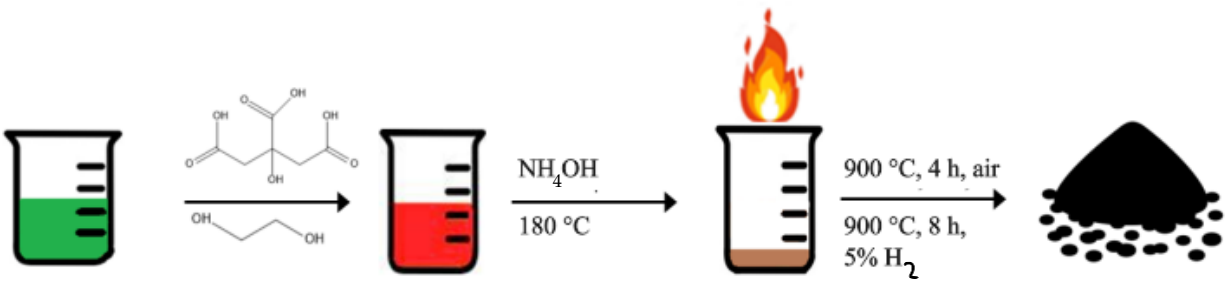

Figure 4.1: scheme of the synthesis approach

This sequence of treatments is mandatory to obtain the desired crystalline phase and porosity and also to avoid the formation of impurities, commonly observed in previous work.[45–47]

4.3. X-Ray diffraction (XRD)

The XRD analysis were performed using a Brucker D8 Advance diffractometer with Bragg-Brentano geometry and a Cu Kα radiation (40 kV, 40 mA, λ=0.154 nm). The data collecting was performed with 0.02°/step at a counting time of 0.35 s/steps in the 2θ range from 20° to 80°. The crystalline phases were identified by search-match method using the Crystallography Open Database through DIFFRAC.EVA, a software for XRD analysis. The bases of this technique are described in the Appendix.

The following paragraphs will show the XRD diffractogram of the samples after the thermal treatment in different atmospheres:

- Air
- Dry hydrogen (H_2)
- Wet hydrogen (5% H_2/H_2O)

4.3.1. Air atmosphere

The powder was first treated at 900 °C for 4 hours in an oxidative environment, with a temperature ramp of 5 °C/min.

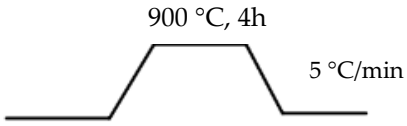

Figure 4.2: condition of air atmosphere treatment

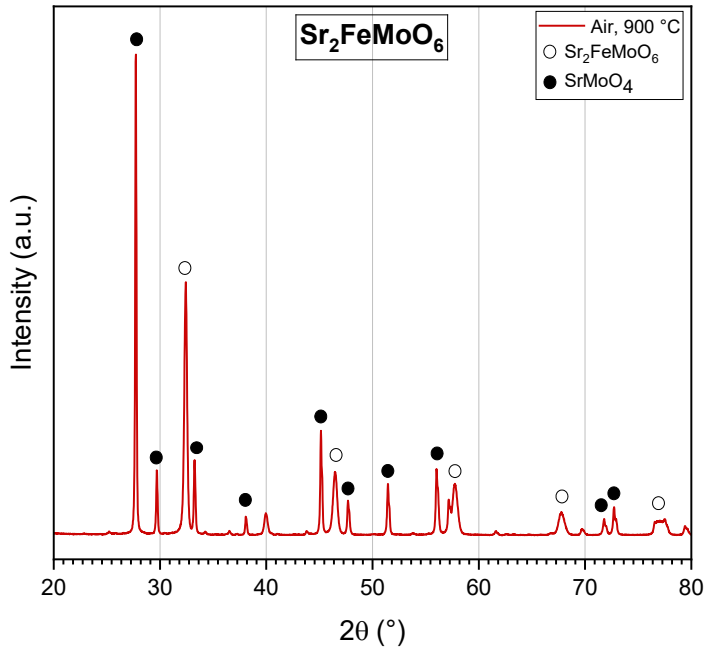

Diffractogram 4.1: XRD diffractogram of SFM 1:1 sample after the calcination treatment in air

Analysing the previous diffractogram is clear that, besides the formation of the researched phase (Sr_2FeMoO_6), the presence of impurity is substantial. In particular, the most relevant one is $SrMoO_4$. The chemical stability of $Sr_2Fe_{1-x}Mo_xO_2$ is caused by the existence of two redox active elements showing a wide range in their oxidation states (+2,+3, and +4 for iron and +5 and +6 for molybdenum). Nevertheless, in atmospheres with high oxygen partial pressures, the content of oxidized cations (Fe^{3+}, Fe^{4+} ,Mo^{6+}) increase, leading to unstable over-stoichiometry products that decompose until the formation of a $SrMoO_4$ impurity.[42] Although strontium molybdate is known to be an insulating material, its presence is not always a drawback, as it helps avoiding the evaporation of molybdenum precursors at temperatures about 800°C, conferring thermal stability to SFM compounds until temperatures about 1500°C; moreover, it can easily be reduced to $SrMoO_3$, a perovskite-like material known for relevantly contributing to the electrocatalytic activity due to its high electrical conductivity. [48]

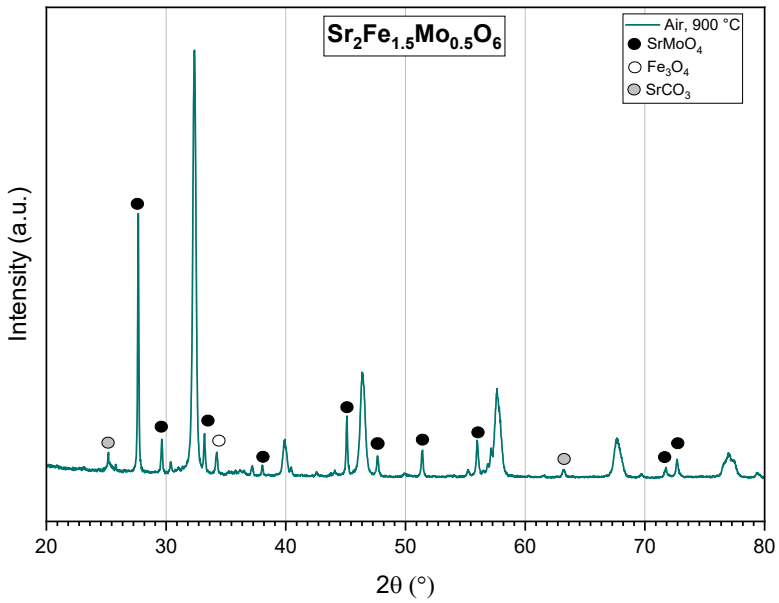

Diffractogram 4.2: XRD diffractogram of SFM 1.5:0.5 sample after the calcination treatment in air

The same pattern has been observed for SFM 1.5:0.5 (*Diffractogram 4.2*), where in addition to the reflexes of the target material, other impurities were recognized.

Wright et al. noted that SFM 1.5:0.5 easily reacts with water to from strontium hydroxide $Sr(OH)_2$, decomposing into Fe_3O_4 and $SrMoO_4$.[49] This observation justifies the presence of the reflexes of these compounds in the diffractogram.

Moreover, the search-match function of the XRD database has detected the presence of a third impurity, strontium carbonate.

4.3.2. Dry hydrogen atmosphere

Given the consideration presented in the last section, a thermal treatment in reducing atmosphere was found to be necessary to limit the presence of undesired phases, thus increasing the desired materials' yield.

The first test was run heating the reactor with the sample from room temperature to 900°C with a linear ramp of 5°C/min under a constant flow of H_2 (5% in He, flow of 50 mL/min). For these reasons, the atmosphere is called dry hydrogen.

This analysis is performed on the air-calcined samples, with the aim of understanding the behaviour of the species and obtaining only the double perovskite material.

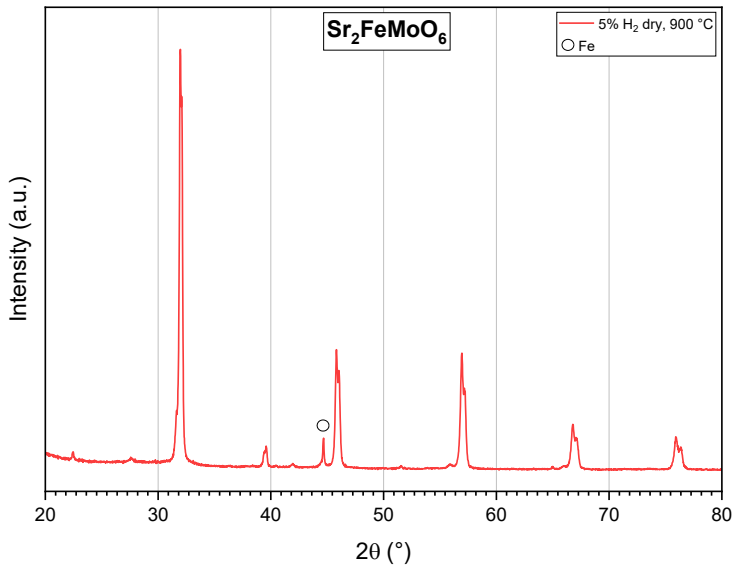

Diffractogram 4.3: XRD diffractogram of SFM 1:1 sample after the treatment in dry hydrogen (5% H_2), 900 °C

The outcome after running the SFM 1:1 (*Diffractogram 4.3*) material is the reflex of mainly the searched material. However, looking closer, it is noticed that the reflex of the double perovskite contains a part of the signal from the defective perovskite, named Ruddlesden Popper phase.

Ruddlesden-Popper phases, with the general formula of $A_{n+1}B_nO_{3n+1}$, were first synthesised by S.N. Ruddlesden and P. Popper in 1958. The structure consisted of $nABO_3$ perovskite layers which are sandwiched between two AO rock-salt layers. The number of perovskite polyhedral units sandwiched determines the phase of the material (*Figure 4.3*).[50] These structures have recently gained interest considering that the nature of these materials allows several of them to accommodate a substantial amount of interstitial oxygen, which could be interesting for their better capacity to diffuse oxygen. The main obstacle of these compounds, particularly when there is only one layer of AO, is the stability of the structure.[51]

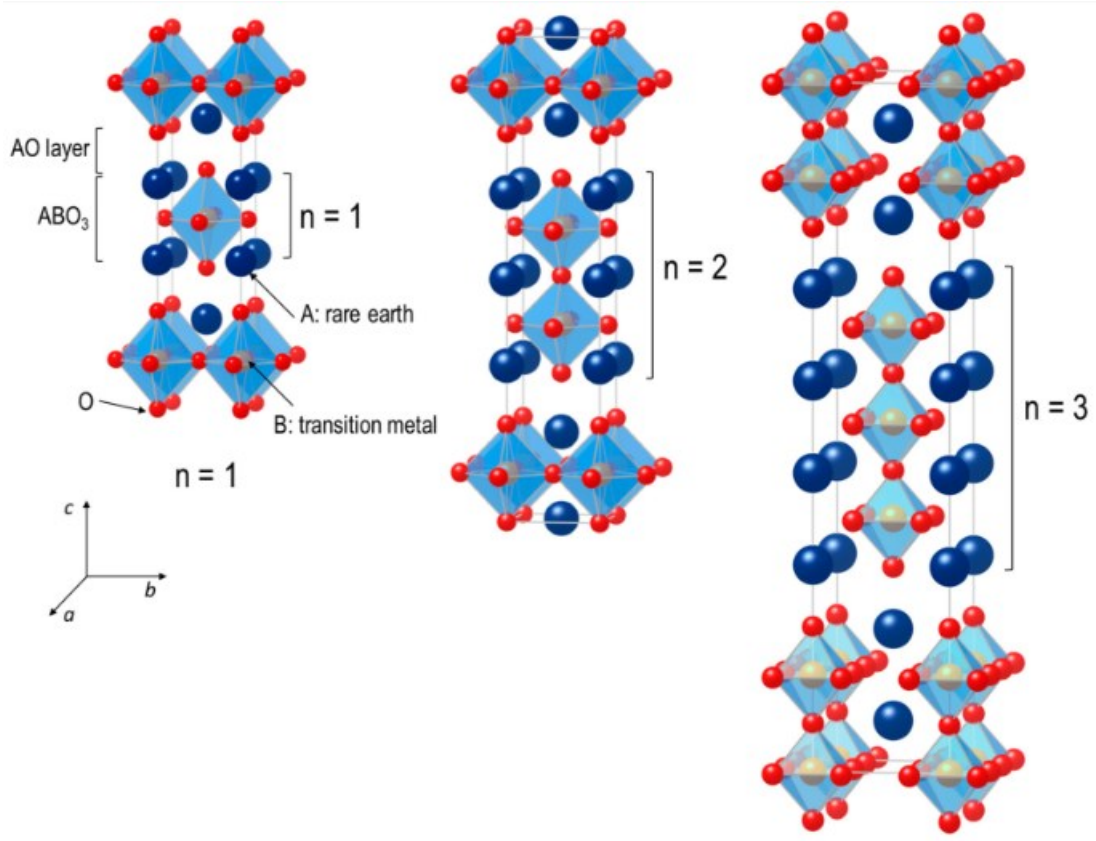

Figure 4.3: Schematic crystal structures of n=1,2,3 members of Ruddlesden-Popper type [51]

Nevertheless, the presence of a reflex at 46° is attributable to Fe, leading to the conclusion that this environment is too drastic for the only production of SFM.

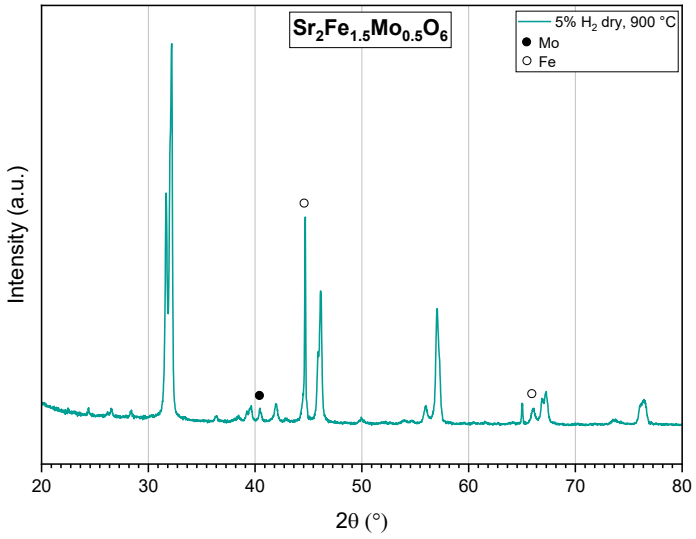

Diffractogram 4.4: XRD diffractogram of SFM 1.5:0.5 sample after the treatment in dry hydrogen (5% H2), 900 °C

Similarly, as with SFM 1:1, in this diffractogram (*Diffractogram 4.4*) there is the presence of the desired phase , Ruddlesden Popper phase and metals, such as Mo and Fe.

4.3.3. Wet hydrogen atmosphere

In order to study a more appropriate environment, the sample was treated in a wet hydrogen (5% H_2/H_2O) atmosphere with the aim to reduce the presence of undesired phases. Thus, subsequently to the thermal treatment in hydrogen-containing atmosphere, another XRD analysis has been out to verify the eventual residual impurity phases and the formation of the desired materials.

The reason why these materials are tested in wet hydrogen atmosphere arises from comparisons with data reported in the literature, in particular, Skutina et al.[42] noted that SFM 1:1 is highly stable in a hydrogen atmosphere, while in air it tends to decompose, as seen from the previous diffractograms. In the same way, SFM 1.5:0.5, according to the data from the literature, is stable in a hydrogen atmosphere even after annealing at 1000 °C and in pure CO_2 at 800 °C. The only significant drawback is that the sample is unstable in humid atmospheres at low temperatures; however the environment without water is already tested and it is not working properly, as seen in *Diffractogram 4.3 and 4.4*.

In the following images, the diffractogram of all samples is reported with the corresponding COD (Crystallography Open Database), which reports the correct pattern recognize for every crystal structures.

The diffractograms were obtained after the air-calcined sample was put in a crucible and heated up from room temperature to 900°C with a linear ramp of 5°C/min under a constant flow of H_2 in a bubbler for 8 hours (5% H_2/H_2O in Ar, flow of 100 mL/min).

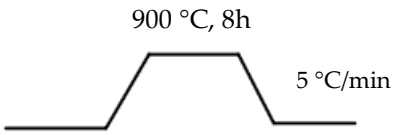

Figure 4.4: condition of wet hydrogen atmosphere treatment

The resulting XRD has been confirmed the presence of the desired perovskite phases (respectively, SFM 1:1 and SFM 1.5:0.5) and the reduction of most of the spurious compounds, as it can be visualized in the following diffractograms.

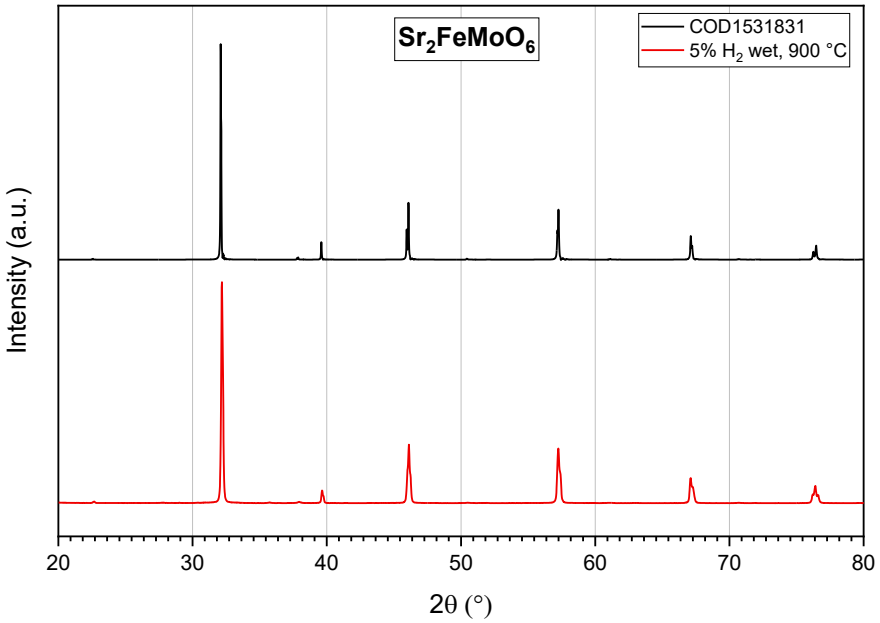

Diffractogram 4.5: XRD diffractogram of SFM 1:1 in wet hydrogen atmosphere (below), compared with the COD (above)

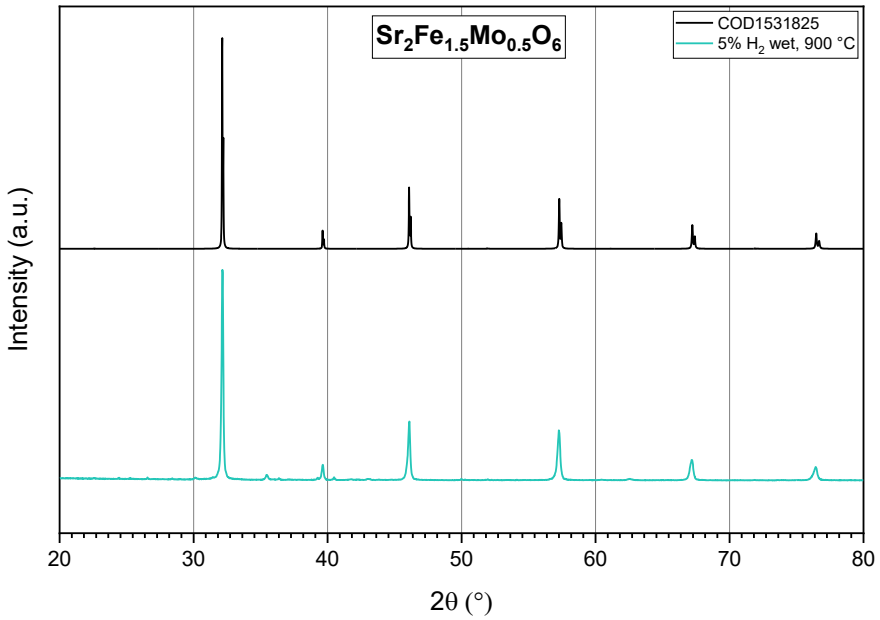

Diffractogram 4.6: XRD diffractogram of SFM 1.5:0.5 in wet hydrogen atmosphere (below), compared with the COD (above)

The SFM 1.5:0.5 diffractogram shows a reflex at 36°, which can be attributed to Fe_3O_4. $Sr_2Fe_{1.5}Mo_{0.5}O_6$ has shown to react with water at low temperatures, forming various oxides

and hydroxides, one of which is magnetite. In spite of these compounds should be eliminated while repeated heating to 800°C [52], a small amount of it is found in the *Diffractogram 4.6*.

The resulting XRD patterns has confirmed that the better experimental path to reach the proper perovskite phase is:

1. Calcination of the powder from room temperature (RT) to 900°C, for 4 hours (temperature ramp: 5°C/min)
2. Reduction of the calcinate sample in a wet hydrogen atmosphere (5% H_2/H_2O) at 900°C, for 8 hours (temperature ramp: 5°C/min)

4.3.4. Summary of all diffractograms

In this paragraph, a summary of the XRD patterns of the calcined, dry hydrogen and wet hydrogen powder is reported, in order to have a better comparison and understanding of the preferred procedure to obtain the desired output.

In each diffractogram, at the bottom, there is the XRD patterns of the sample treated in air, in the middle those of the sample treated in a dry hydrogen environment and on top those obtained after treatment in a wet hydrogen atmosphere, reported with the Miller indexes.

Comparing all of them, it is clearly shown that the sample calcined is the one with the highest quantity of different phases and components.

The one in the middle is very similar to the desired product, but has some reflex which is attributable to the metallic phase of some metallic precursors, as Fe and Mo. This section is better disclosed in *Section 4.4*.

Eventually, the phase obtained via wet hydrogen atmosphere has the same pattern as proper product, as shown in the previous paragraph.

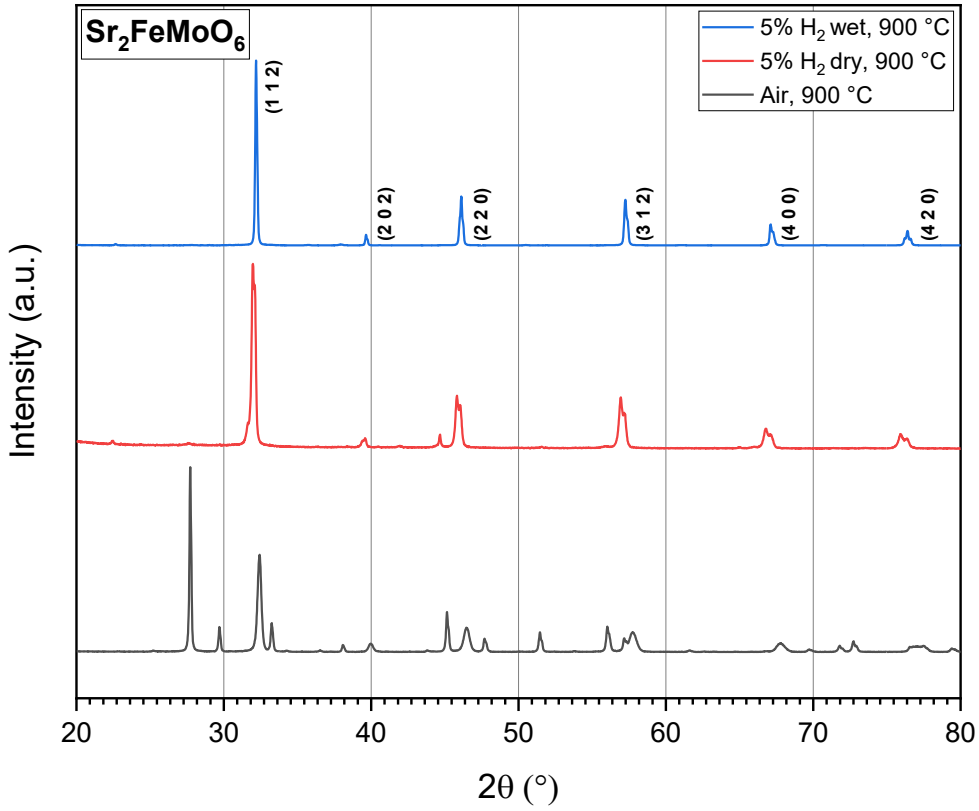

Diffractogram 4.7: XRD diffractograms comparison of SFM 1:1 in air (at the bottom), in dry hydrogen (in the centre) and in wet hydrogen (at the top)

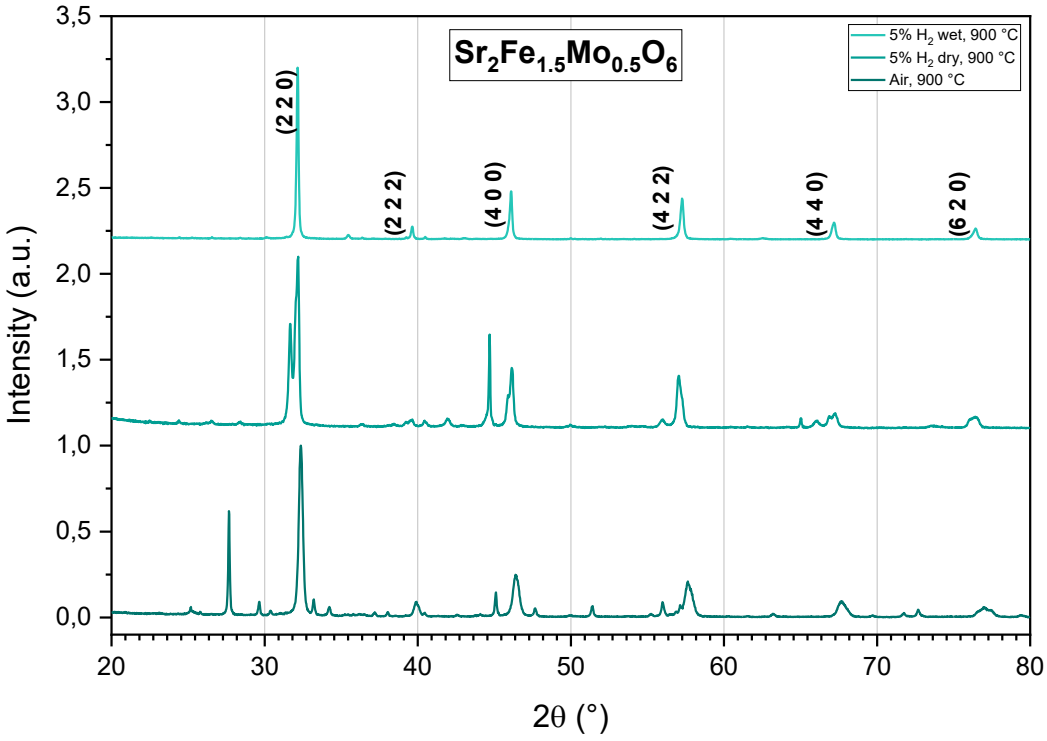

Diffractogram 4.8: XRD diffractograms comparison of SFM 1.5:0.5 in air (at the bottom), in dry hydrogen (in the centre) and in wet hydrogen (at the top)

4.4. H_2-Temperature Programmed Reduction (H_2-TPR)

The Hydrogen-Temperature Programmed Reduction (H_2-TPR) analysis was performed using an Autochem II 2920 Micromeritics, equipped with a Thermal Conductivity Detector (TCD).

The measurements were carried out in a quartz reactor by using 50 mg of sample and heating from room temperature to 900°C with a linear ramp of 10°C/min under a constant flow of H_2 (5% in He, flow of 50 mL/min). In order to collect good data, the samples were previously outgassed with a flow of He at room temperature. This kind of analysis has been carried out on the air-calcined samples, with the aim of understanding the behaviour of the reducible species and the conditions required to achieve the target materials.

The H_2-TPR profiles in *Graph 4.5* have shown different features, depending on the type of the perovskite:

- **Sr_2FeMoO_6**
- **$Sr_2Fe_{1.5}Mo_{0.5}O_6$**

The first peaks could probably refer to the double reduction of Fe. In particular, the first one at 413°C could be assigned to the reduction of Fe^{4+} to Fe^{3+}, the second one (at 503 °C) to the reduction of Fe^{3+} to Fe^{2+}.

The peak at 730°C could be probably ascribed to the double reduction of Mo, from Mo^{6+} to Mo^{4+}.

The intensity of both peaks in the range 400°C-500°C increases with the quantity of Fe, meaning that they can be attributed to the Fe. Instead, the second peak at 730 °C is less wide in SFM 1.5:0.5 than SFM 1:1, for this reason attributable to Mo.

Kim et al. [53] reported overlaid results, moreover they have noticed that SFM perovskites with higher Mo content exhibit lower reducibility and moderate oxygen ionic conductivity, which could explain why SFM 1:1 has a wider and right-shift peak for Mo. Other results in literature as similar, nevertheless to be certain about the attributions further investigations with other techniques, i.e. XAS, Mössbauer, could be implemented. [54]

Then, the peaks at around 900 °C are probably assigned to the reduction to metallic component for both cations, as these phases were detected by the XRD measurements performed after this analysis.

The previous deductions are confirmed by the *Table 4.1*, which highlight the hydrogen consumption, found through the integration of the signal of each peak:

- The first peak (composed of the first two peaks), which could refers to Fe(IV)->Fe(II) reduction, shows a higher H_2 consumption for SFM 1.5:0.5 than SFM 1:1
- The second peak, which was attributed to the reduction of Mo(VI) to Mo(IV), shows a higher value for SFM 1:1
- The third peak, is probably ascribed to the reduction of Fe and Mo to their metallic phases, as shown by *Diffractogram 4.3 and 4.4*. Moreover, for SFM 1:1 no Mo metallic phase was found, so that value could be possible refer to only Fe reduction, and this could be the reason why it is lower compared to SFM 1.5:0.5.

Table 4.1: H_2 consumption for both materials

	SFM 1:1		**SFM 1.5:0.5**	
	H_2 consumption (cm^3/g)	**H_2 consumption** (mmol)	**H_2 consumption** (cm^3/g)	**H_2 consumption** (mmol)
1^ peak (Fe)	15.6	34.9	29.8	66.7
2^ peak (Mo)	49.1	110.0	38.4	85.8
3^ peak (metallic phases)	1.37	3.07	8.33	18.6

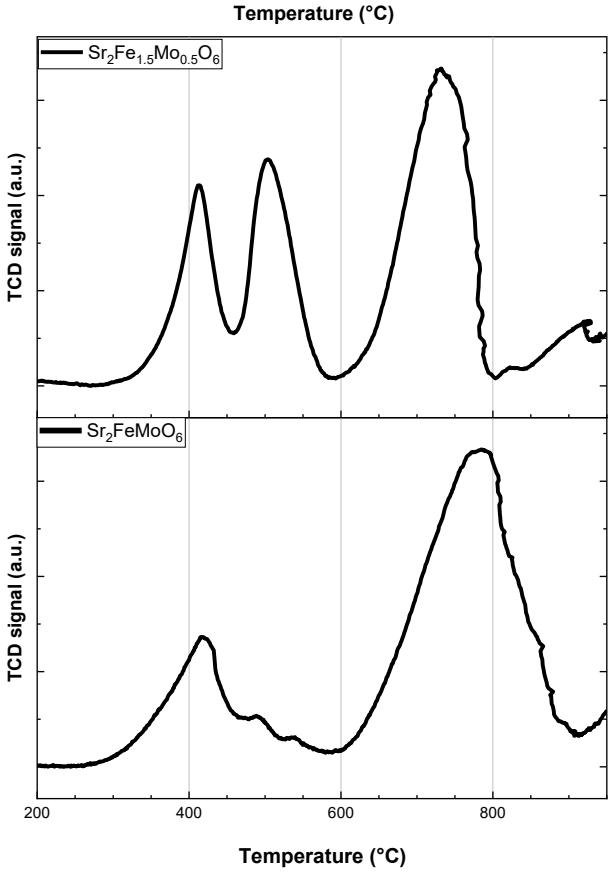

Graph 4.5: H2-TPR analysis of SFM 1.5:0.5 (on the top) and SFM 1:1 (on the bottom) materials after the calcination treatment in air

4.5. Scanning Electron Microscopy (SEM)

Scanning Electron Microscopy (SEM) images were acquired with a Zeiss Sigma HD Microscope with an applied potential of 5 kV. In the following chapter, images at different enlargements are captured, in order to have an understanding of the fresh materials' morphology. The instrument is equipped with EDX, whose results are analysed in the next section.

The images in *Figure 4.6* at low magnification have shown that the two samples (SFM 1:1 and SFM 1.5:0.5) exhibit dissimilar morphology. In fact, comparing the images at an enlargement of 25x, they both share a coral-like structure.

The figures shows worm-like particles, which are homogeneously distributed, together with porous framework. This conformation of the material can facilitate gas diffusion and mass transport within the electrode layer. [55]

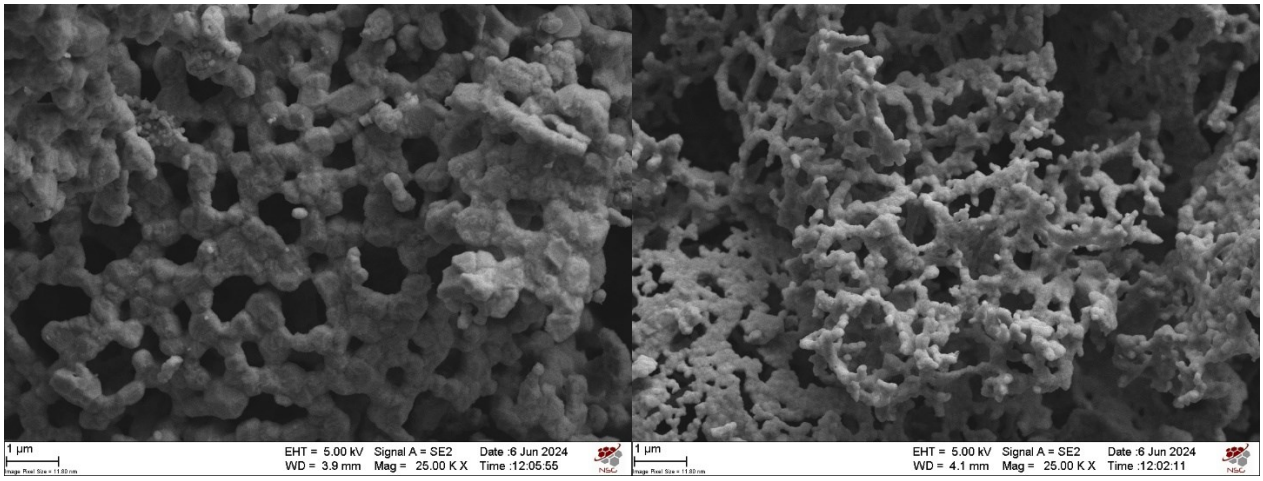

Figure 4.6: SEM images at 25x magnification of SFM 1:1 (on the left) and SFM 1.5:0.5 (on the right)

However, looking closely with a higher magnification (100x, *Figure 4.7*), the particles are completely different, as SFM 1:1 sample shows the grains with a polyhedral and faceted shapes, while SFM 1.5:0.5 particles have a rounded configuration. The morphology can be influenced by the sintering technique used, however, in this case it was identical. This difference is presumably due to the higher presence of molybdenum: as can be seen from a comparison with the literature, several materials containing this transition metal show crystallites of comparable size and shape, differently if the materials are SFM 1:1 or SFM 1.5:0.5.[56,57] The porosity of these materials will be investigated more in the *section 4.8*, with BET model.

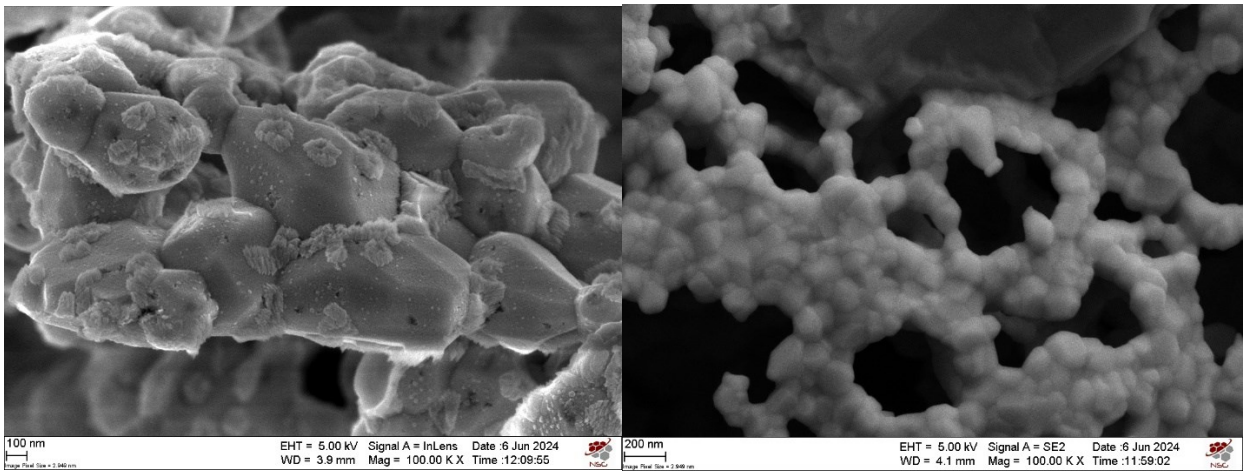

Figure 4.7: SEM images at 100x magnification of SFM 1:1 (on the left) and SFM 1.5:0.5 (on the right)

4.6. Energy Dispersive X-Ray (EDX) and quantitative X-Ray Photoelectron Spectroscopy (XPS)

The EDX and the XPS techniques were used to characterize the samples from the compositional point of view. The main difference between the two is the depth of analysis and this is linked to their working principles, which are further described in the Appendix:

- EDX characterization is an analytical technique in which a high energy beam of charged particles is focused into the sample to stimulate the emission of characteristic X-Rays that can be collected and studied. The whole process is based on the unicity of the X-Ray spectrum of each element. This technique gives qualitative and quantitative information about elements present in a sample and its typical depth is in the order of micrometres.
- XPS analysis is based on the photoelectric effect. It measures the kinetic energy and number of photoelectrons emitted from a material by irradiating the sample with an X-Ray beam. The escape depth is of few first layers of the sample, thus making this technique useful for surface studies. Its typical sampling depth is, in fact, considered to be between 1 and 10 nm.

The two techniques may be coupled, to achieve a good general understanding of the constituent elements of the material and their relative percentage in function of the depth, thus evaluating the presence of segregation phenomena. Moreover, by means of XPS it is possible to have an information concerning the oxidation state of the elements and their chemical environment. The EDX analysis have been carried out using the Oxford X-Act PentaFET Precision microscope, while XPS analysis have been performed with a Thermo Scientific ESCALAB QXi spectrometer, employing a monochromatized Al Kα source ($h\nu$ = 1486.68 eV) and a charge compensation gun. The elemental quantification has been obtained by integration of the photo peaks, after Shirley-type background subtraction.

By comparing the results obtained with the two techniques in *Tables 4.2 and 4.3*, it is possible to see that the nominal Fe content is increased for both samples (SFM 1:1 and SFM 1.5:0.5) compared to the stoichiometric value. It generally tends to segregate, which could be related to the tendency of Fe to migrate to the surface (or in the first micrometres) in order to form other species thermodynamically favourable, as well as in the perovskite phase, as the oxides/hydroxides. It is surely something expected considering the presence of Fe_3O_4 in the XRD diffractogram, even though XRD is a bulk technique, with a depth of analysis up to 30 μm, while XPS is a surface technique.

The migration of Mo is noted in two different directions for both of the materials. In particular, in the SFM 1:1 sample, a smaller amount of the metals is found within the first micrometres, while for SFM 1.5:0.5 the quantity is higher in the first micrometres and in the surface.

For what concerns Sr, in both the samples, a reduction of it (specifically, ~ 7% in case of SFM 1:1) is found, in agreement with the segregation of Fe in the surface.

Table 4.2: comparison of theoretical and experimental percentage compositions of cations of SFM 1:1

Element	**Theoretical (%)**	**EDX (%)**	**XPS (%)**
Sr	50.0	46.3	46.2
Fe	25.0	30.5	29.1
Mo	25.0	23.2	24.7

Table 4.3: comparison of theoretical and experimental percentage compositions of cations of SFM 1.5:0.5

Element	**Theoretical (%)**	**EDX (%)**	**XPS (%)**
Sr	50.0	45.3	48.2
Fe	37.5	41.5	38.5
Mo	12.5	13.2	13.3

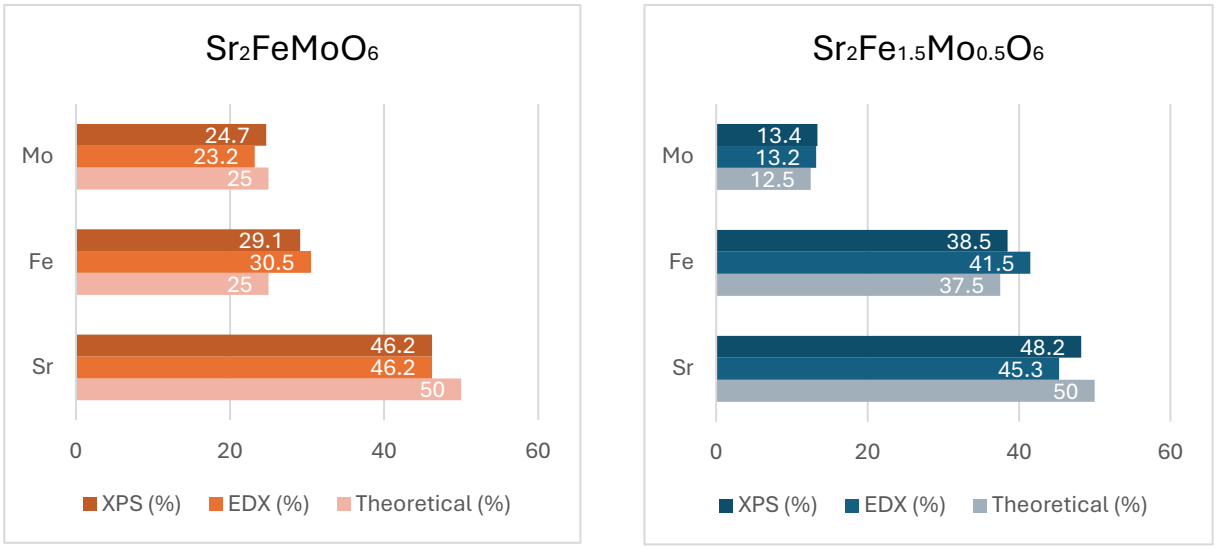

Figure 4.8: comparison of Mo, Fe and Sr percentage quantity theoretical, from XPS and EDX analysis in SFM 1:1 (on the left) and SFM 1.5:0.5 (on the right)

4.7. Understanding the surface: qualitative X-Ray Photoelectron Spectroscopy (XPS)

XPS technique has also been carried out in its qualitative way, in order to have a more specific understanding of the possible presence of spurious phases on the samples' surface by means of the cations' oxidation states. The analysis has been performed again with the Thermo Scientific ESCALAB OXi spectrometer, employing a monochromatized Al Kα source ($h\nu$ = 1486.68 eV) and a charge compensation gun. Survey spectra were acquired with a 100 eV pass energy, 0.5 eV/step and 25 ms/step dwell time, high resolution spectra have been collected at 20 eV pass energy, 0.1 eV/step and 25 ms/step dwell time. The bases of this technique are deeply described in the Appendix.

To have a better comprehension of the species present in the surface (between 1-10 nm), high resolutions spectra of Sr 3d, Mo 3d, Fe 2p, O 1s, are reported and analysed as follows. The spectra are analysed with Advantage Software and the value of the binding energy are corrected, due to the charging of the sample, conferring to adventitious carbon the value of 284.6 eV.

4.7.1. Strontium XPS spectra

The high resolution spectra of Sr 3d, reported in *Spectrum 4.1*, shows two doublet that overlap, as strontium is characterized by a spin-orbit splitting of its 3d peak. The slight shift

of the SFM 1:1 sample to higher binding energy is attributed to a reduction in electron density around the nucleus. This is associated with a change in the chemical environment of Sr, caused by the increased amount of Mo in the sample, which possesses higher electronegativity.

For both of the materials, the fitting procedure reveals two main contributions (four peaks in total, coupled two by two), which overlap . Based on the binding energy, in agreement with the literature[58], at around 132.6 eV for SFM 1.5:0.5 and 132.8 for SFM 1:1, the photopeak ($3d_{5/2}$) could arise from perovskite structure, while the second photopeak ($3d_{5/2}$) at around 134.3 eV for SFM 1.5:0.5 and 134.5 eV form SFM 1:1 is attributed to the oxides and other additional states. In both the cases the spin-orbit splitting between $3d_{5/2}$ and $3d_{3/2}$ of 1.7 eV.

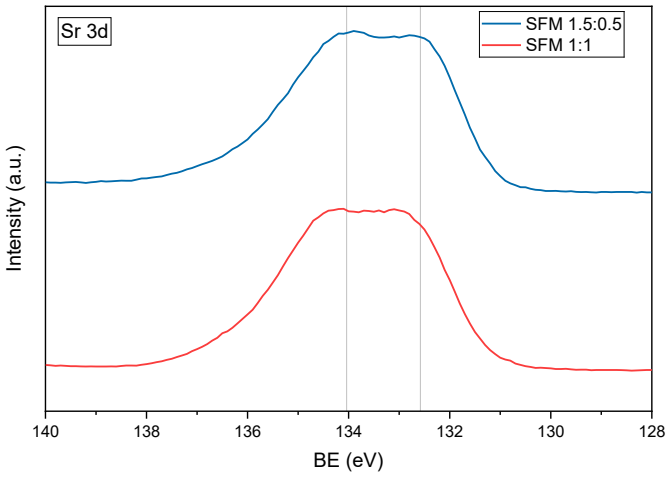

Spectrum 4.1: high resolution analysis of Sr3d peak (the two straight lines refer to SFM 1.5:0.5 main contributions ($3d_{5/2}$))

4.7.2. Molybdenum XPS spectra

In *Spectrum 4.2*, the high resolution spectrum of Mo is reported. The separation in binding energy due to spin-orbit splitting for Mo 3d is approximately of 3.1 eV for both samples, as found in a previous work. [58]

The spectrum comprises two contributions: one ($3d_{5/2}$) at 231.8 eV for SFM 1:1 and 231.9 eV for SFM 1.5:0.5, the other ($3d_{5/2}$) at 233.3 eV for SFM 1:1 and 233.4 eV for SFM 1.5:0.5. The first could be attributed to Mo^{5+} and the second to Mo^{6+} . Nevertheless, it is not straightforward to attribute the species to one peak, as from the literature, it is said that comparing the spectrum of the reference compounds, Fe and Mo are present in a mixed iron

and molybdenum valence states, involving 30% Fe(III)-Mo(V) and 70% Fe(II)-Mo(VI) states. This is strengthened via the analysis made by Mössbauer technique, which indeed exhibit the presence of valence fluctuations, in which an electron jumps from Fe^{2+} ion to a Mo^{6+} ion leading to a Fe^{3+}-Mo^{5+} configuration.[59]

A slight rightward shift is observed for SFM 1:1 only in the high-resolution Mo spectra. Based on a comparison with the literature [60], this shift is likely attributed to the presence of a more reduced phase in the material. Employing Mössbauer spectroscopy and correlating its results with both materials could clarify whether the SFM 1:1 sample exhibits an enhanced presence of Fe(III)-Mo(V) states, instead of the percentage cited above and found in other samples.

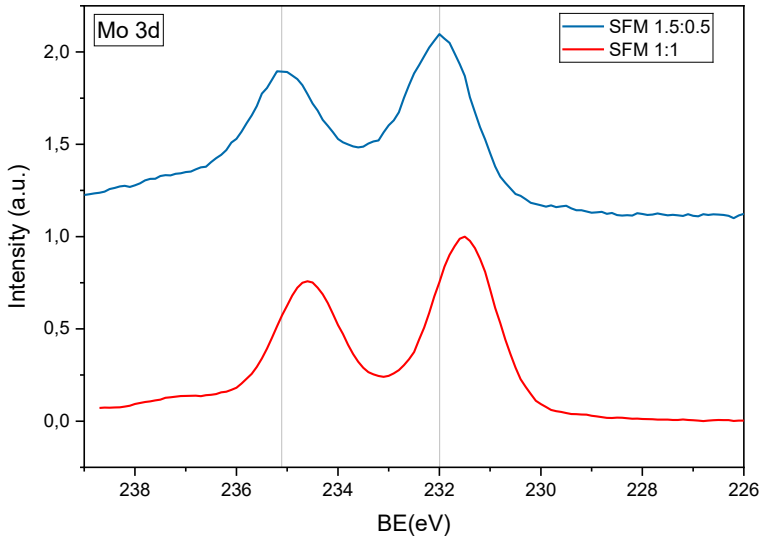

Spectrum 4.2: high resolution analysis of Mo3d peak (the two straight lines refer to SFM 1.5:0.5 main contributions ($3d_{5/2}$))

4.7.3. Iron XPS spectra

The high resolution spectrum for Fe is reported as follows. The deconvolution of these peaks is not performed as the signal is low and a very unprecise prediction would have been done. The only study done in this case is qualitative, and related to the shift of the peaks. The two spectra are superimposable, meaning that any notable change is observed by the XPS measurements, which does not necessary mean that the species detected are identical. For

what concern iron, a brief explanation was taken by the literature and reported in *Section 4.7.2*.

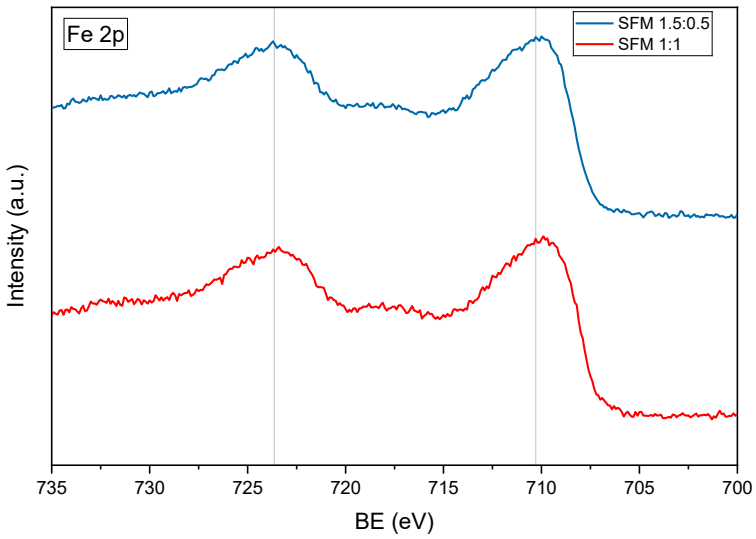

Spectrum 4.3: high resolution analysis of Fe2p peak (the two straight lines refer to SFM 1.5:0.5 main contributions)

4.7.4. Oxygen XPS Spectra

The XPS spectrum of O 1s, as reported by Angervo et al., can have a profoundly complex shape due to various chemical states falling to a relatively narrow binding energy range. In fact, there could be several oxides on the surface originating from SFM (both 1:1 and 1.5:0.5) and from separate compounds including Fe, Sr and Mo. [58]

The spectra are characterized by three main contributions: metal oxides, carbonates/hydroxides and highly oxydrilate species.

The binding energy values, respectively of 529.8 eV, 531.2 eV and 532.5 eV, are in agreement with what is reported in literature.[61] The presence of carbonates is confirmed, for both of the materials, by C 1s spectra.

As noticed in Sr spectral region, the SFM 1:1 signal is shifted at higher binding energy, consistently, how above mentioned, with the presence of higher electronegativity material. The shape of the peak in SFM 1.5:0.5 is wider compared to the other material, showing a more intense contribution of metal oxides, as confirmed by quantitative analysis, which could be related to the migration of cations like Fe and Mo in the surface.

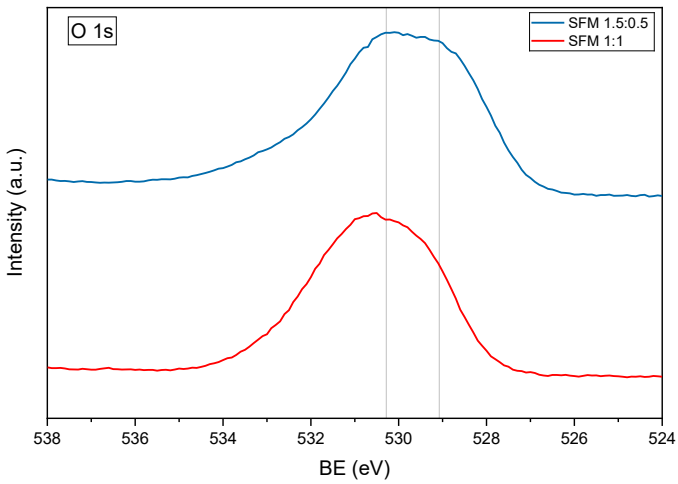

Spectrum 4.4: high resolution analysis of O1s peak (the two straight lines refers to SFM 1.5:0.5 contributions of metal oxides and carbonates)

4.8. Porosity analyses

In order to characterize the textural parameters of the samples, such as the Specific Surface Area (SSA) and Pore Size Distribution (PSD), gas adsorption analyses using nitrogen were performed, so as to obtain the adsorption and desorption isotherms for the studied materials.

From these, the SSA was determined by employing the BET model, while the PSD was obtained using the BJH method. The basis of these techniques is described in the Appendix. The measurements were carried out using an ASAP 2020 Plus Physisorption instrument. The samples were first degassed at 300°C for 3 hours in order to remove gas molecules adsorbed on the surface of the material, to then undergo analysis. During the analysis, the instrument doses a specific amount of gas inside the tube containing the sample to reach a predefined pressure , then it waits until equilibrium is reached, and finally the amount of gas adsorbed by the sample, is measured. This was done consecutively up until close to saturation pressure is reached, corresponding to relative pressure p/p^0 =0.995.

The isotherm is useful to figure out the type of pores that are found in the two samples, however, an additional calculation through BJH model is carried out, in order to quantify the number and the average width of the pores.

Porous materials are classified by the pore size; the International Union of Pure and Applied Chemistry (IUPAC) classify the porous materials in:

- Microporous, materials have pore diameters of less than 2 nm;
- Mesoporous, materials have pore diameters between 2 nm and 50 nm;
- Macro porous, materials have pore diameters of greater than 50 nm. [62]

From the following graphs, the isotherm of SFM 1:1 and SFM 1.5:0.5 is a hybrid between type II-IV, respectively typical of macroporous and mesoporous adsorbents, since these materials have both types of pores, as confirmed by the pore size distribution graphs (*Graph 4.10*).

For sample SFM 1:1 an abrupt closing of the hysteresis can be observed at relative pressure ~ 0.45, due to cavitation. This can be caused by the presence of pores with pore necks diameter smaller than 5 nm, which desorb all at the same pressure due to tensile strength effect.

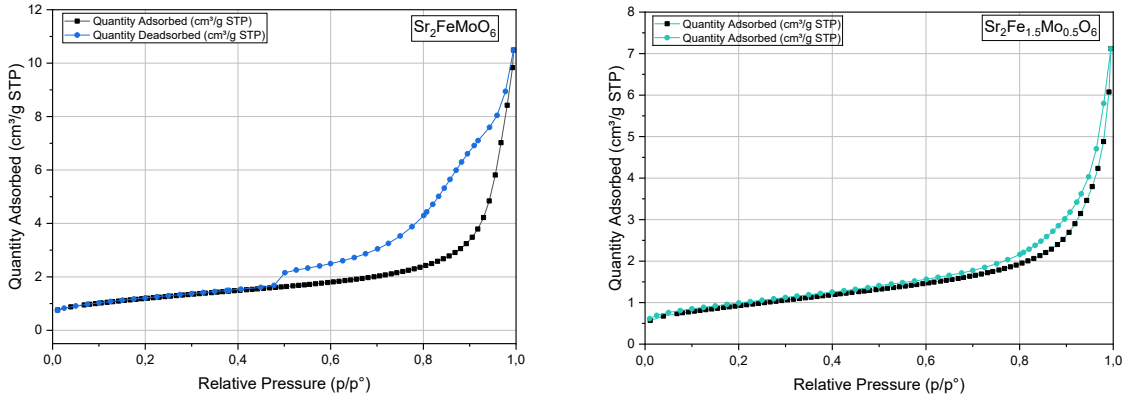

Graph 4.9: Isotherm curves of SFM 1:1(on the left) and SFM 1.5:0.5 sample (on the right)

From the PDSs of the samples, it is possible to determine the average dimension of the pores. To evaluate it, the BJH model is used, which is based on the Kelvin equation (*Equation 66*), which correlates p/p^0 to the radius of the pore.

SFM 1:1 sample has a broad peak, in the range of 30-60 nm and the maximum is around 40 nm, while for the SFM 1.5:0.5 sample, the peak is around 20-50 nm, and the maximum around 30 nm.

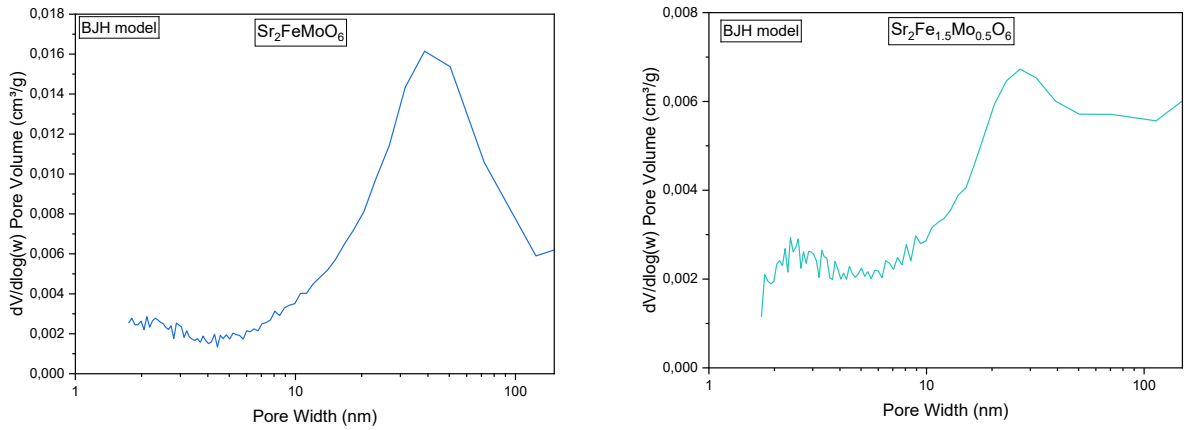

Graph 4.10: Pore Size Distribution graph for SFM 1:1 (on the left) and SFM 1.5:0.5 (on the right)

The SSA (Specific Surface Area, m^2/g) is calculated through the BET model; this information is indispensable for the development of surface materials with high performance. It is 4.1 m^2/g for SFM 1:1 and 3.2 m^2/g for SFM 1.5:0.5, similar to other values found in literature. [63] All these information can be used for characterizing the pores of the materials.

The pore size is lower for the highest iron containing sample, as well as SSA; this implies that in SFM 1.5:0.5 sample, there is a lower amount of small pores. Such a behaviour could be a consequence of the presence of agglomerations.

5. THERMOCATALITIC TEST: CO_2 HYDROGENATION (RWGS)

This chapter will be dedicated to the explanation of the use of SFM materials as catalysts for the Reverse Water-Gas Shift reaction (RWGS), both from the architectural point of view, with a brief description of the experimental apparatus, and from the chemical point of view, regarding firstly the results but also the analysis of post-reaction samples and the relative considerations in respect to the fresh ones.

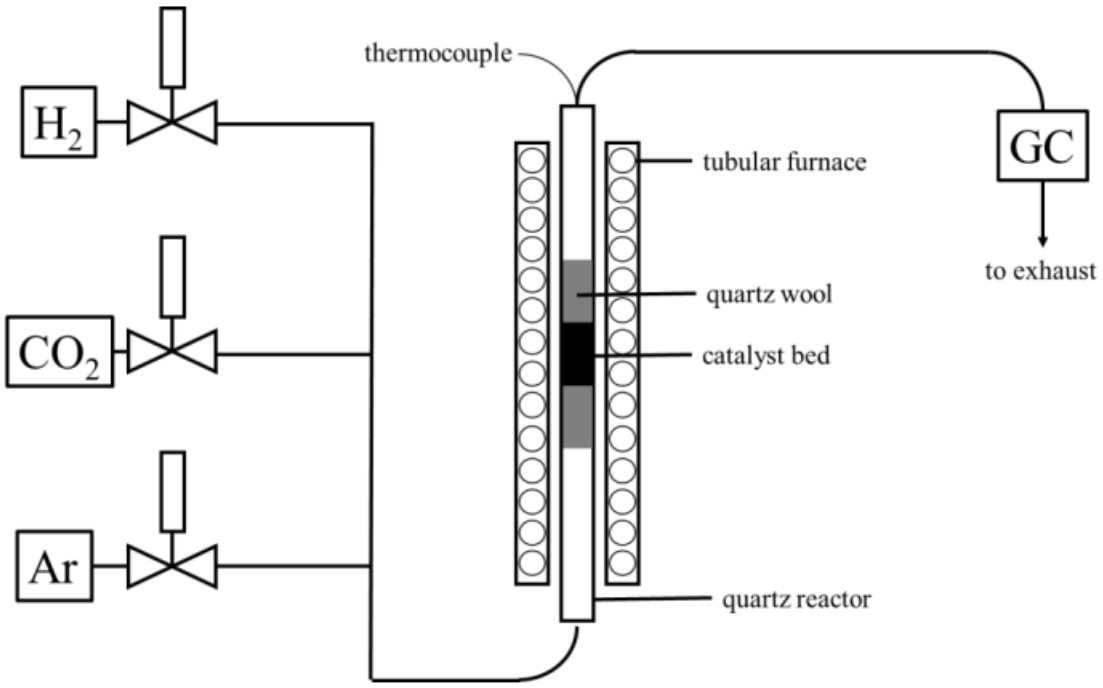

Figure 5.1: schematic representation of the set-up utilised for the thermo-catalytic reduction of CO_2 to CO

The depicted reaction is summarised as:

$$CO_2 + H_2 \rightarrow CO + H_2O$$

The catalytic set-up utilised for this work, represented in *Figure 5.1*, was composed by a fixed reaction bed, in which the reduced powders were deposited in a 6 mm quartz tube between two layers of quartz wool. The reactor, finally, was inserted into a tubular furnace; the temperature was controlled by a K-type thermocouple on the upper end of the tube, in which the connection to the Gas Chromatographer (GC) was located. The inlet gas fluxes were managed by three mass-flow controllers (MFCs), in order to have H_2:CO_2 ratio of 5.6%:4.4% [35], while argon was used as carrier gas (90%). The choice of this proportion is made after some comparison with the literature[35], in which the entering fuel of 16%H_2O +

16%CO_2 + 20%H_2 + 48%N_2 was found to be the most suitable for the reaction. The high percentage of the hydrogen chosen is due to the necessity of maintaining SFM 1:1 and SFM 1.5:0.5 stable in the working conditions. Moreover, the proportion of fuel gas: carrier gas used by the research group 10%:90%, in order to have a diluted system. The choice of not including water in the inlet gases is due to the need of avoiding the contamination of the gas chromatographer column .

The inlet gas passes through to a condenser to remove water. The exhaust gasses analysis was carried out by an Agilent Technologies 7890A GC System, equipped with a Porapak Q and a Molsieve column, while the gas detection was controlled by a TCD detector. The sampling time was equal to 12 minutes, to have a complete evaluation of all the output gasses.

5.1. Catalytic results

The catalytic results are reported in *Graph 5.2*, comparing the activity of the two materials in the conversion of CO_2. The curve in red reports the %CO yield.

The first quantity is calculated through the *Equation 57*:

$$\%CO_2\ conversion = \frac{A^0_{CO_2} - A^f_{CO_2}}{A^0_{CO_2}} \cdot 100$$

Equation 57

Where $A^0_{CO_2}$ is the peak area detected by GC of CO_2 at the beginning of the experiment and $A^f_{CO_2}$ is the peak area of CO_2 at the different temperatures (corresponding to the different sampling time).

The %CO yield is calculated as follows:

$$\%CO\ yield = \frac{A^f_{CO} - A^0_{CO}}{A^0_{CO_2}} \cdot 100$$

Equation 58

Where A^f_{CO} is the peak area of CO at each temperature and A^0_{CO} is the peak area of CO at the beginning of the experiment. The denominator of the ratio ($A^0_{CO_2}$) is the area of CO_2 at the beginning of the experiment.

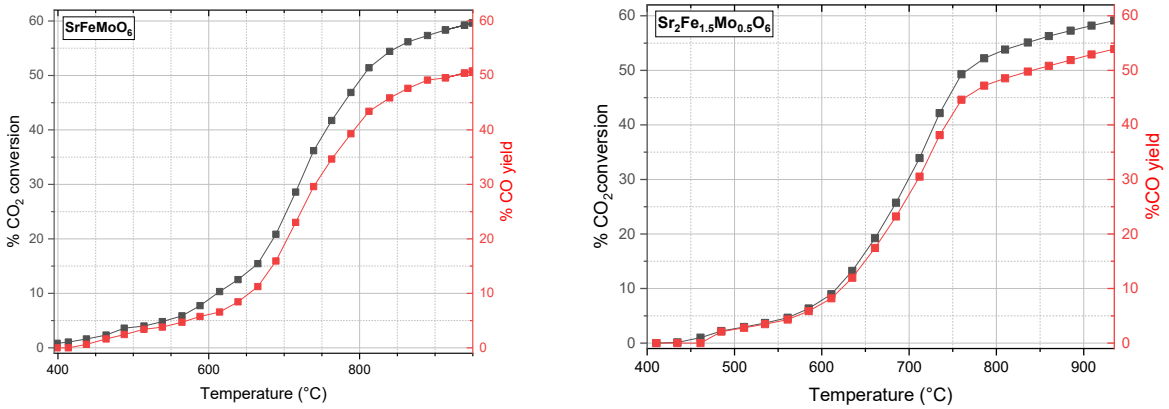

Graph 5.2: %CO_2 conversion and %CO yield with respect to reaction temperature for SFM 1:1 (on the left) and SFM 1.5:0.5 (on the right)

A comparison graph of the two samples is reported in *Graph 5.3*, in order to better correlate the behaviour of each perovskite.

The temperature on-set of the RWGS reaction is about 400 °C. This value is quite accurate, since the temperature has been measured at the time that the produced gas was injected into the GC system.

The %CO_2 conversion reaches the same value for both samples, around 59.7%, but the %CO yield is the main difference between them. In fact, SFM 1:1 shows a value of 50.8%, while SFM 1.5:0.5 55.9%.

The curve for the SFM 1.5:0.5 is narrow, meaning that the difference in values between CO_2 conversion and CO yield is lower and less undesired compounds are formed.

The exhaust gasses pass through a gas chromatograph and none of the following gases (CH_4, O_2) were detected.

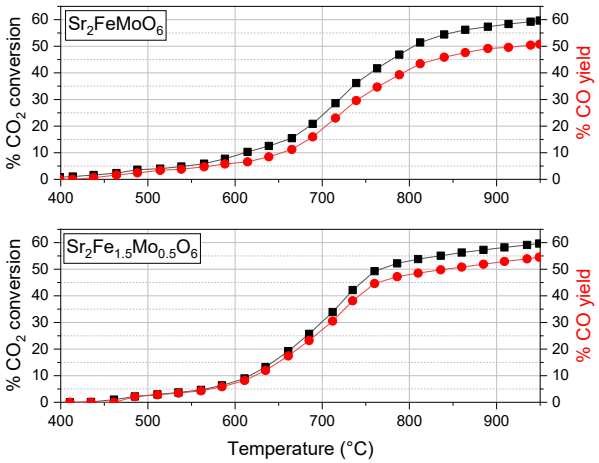

Graph 5.3: %CO_2 conversion and %CO yield with respect to reaction temperature for SFM 1:1 (above) and SFM 1.5:0.5 (below)

To better understand the processes at the base of the reaction, some further comparisons with the literature has been needed. Meng et al. [64] studied the selectivity between RWGS reaction and Fischer-Tropsch synthesis in carbon-supported iron-based catalysts and what they noticed is that the primary reaction during CO_2 hydrogenation is the production of CO via RWGS, in particular at low CO_2 conversion; in this case the CO selectivity is almost 100% (as found in the experiment, *Graph 5.3*).

It has been reported that CO_2 adsorbed on metal surfaces is present in two states: a physiosorbed linear CO_2 state and a chemisorbed bent CO_2^- state. The anionic species turns out to represent an intrinsic precursor for CO_2 dissociation into CO and oxygen on iron surface. Molybdenum interacts with the Fe species via the Fe-O-Mo bridge. The literature reports the presence of charge transfer from Fe to Mo species, via the Fe-O-Mo bond, resulting in an electron-deficient state for the Fe species. CO_2 is strongly chemisorbed on the Fe surface (in Fe-O-Mo structure) and undergoes sequential carbon-oxygen bond cleavage. In agreement to the results obtained, the both decrease of Mo and increase of Fe enhance the CO selectivity for RWGS reaction.[65,66] Light hydrocarbons are by-products of RWGS reaction over many catalysts, which could be the explanation of the presence of the small gap between the two curves of *Graph 5.3*.

5.2. Post-reaction Characterization of SFM materials

All the sample were again characterized, after their use as catalysts for the RWGS reaction, in order to have a better comprehension of eventual structural and/or surface modification and also to give some considerations about the possibility for these materials to be re-used in CO_2 reduction reaction cycles.

5.2.1. X-Ray Diffraction (XRD)

The XRD analysis was performed keeping unchanged the experimental parameters used for the fresh samples and described in *Section 4.3*.

A different behaviour was noticed for the two samples; in fact, SFM 1:1 diffractogram has shown no significant differences between the fresh samples and the same materials after RWGS reaction cycle.

In particular, in *Diffractogram 5.1*, a comparison of the two patterns (SFM 1:1 pre reaction, in red, and SFM 1:1 after GC, in green) is reported. As it is possible to notice, the diffractograms are superimposable, meaning that the material does not undergo the formation of undesired crystalline phases; this result is clearly interesting for the purpose of a realizing reversable materials and devices.

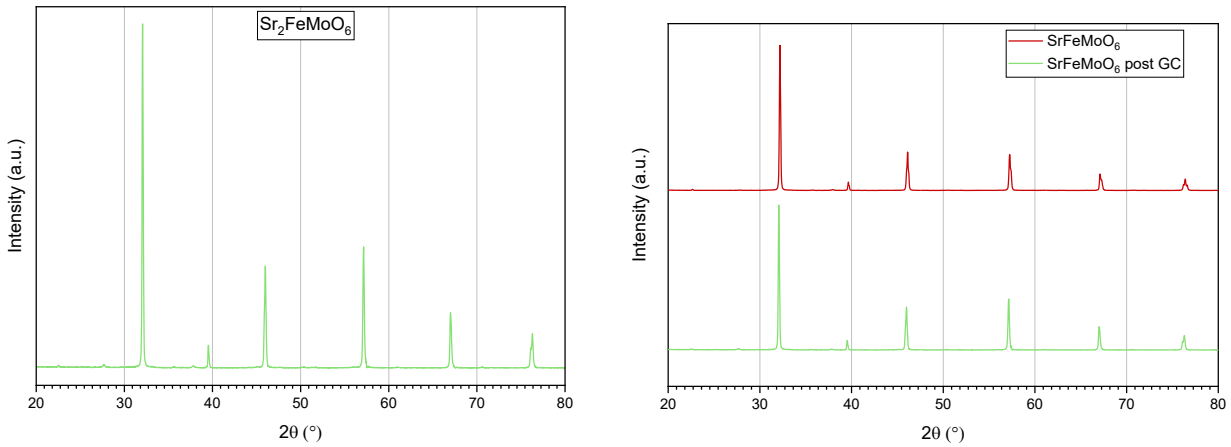

Diffractogram 5.1: on the left, XRD diffractogram of the SFM 1:1 material post-reaction, on the right, the pattern of the fresh (above) and post-reaction (below) material

In the Fe enriched material (SFM 1.5:0.5), which has higher catalytic activity, some changes are noticed, as shown in *Diffractogram 5.2*. In particular, different new phases are formed after exposure to the CO_2-H_2 mixture.

The presence of Fe_3O_4 is not negligible even in the sample before the reduction: in fact the reflex at 36° is present in the diffractograms before and after the reaction.

$SrCO_3$ is produced after exposure to CO_2 and it is consistent with the tendency of Sr to form carbonates when it is exposed to carbon dioxide. Nevertheless, the carbonate formation reduced the catalytic activity of the perovskite. The decomposition of $SrCO_3$ is noted to start at 930°C in argon atmosphere on a Ce-doped $SrFeO_3$ perovskite. A minor carbonate formation was found when treating $SrFe_{0.9}Ti_{0.1}O_3$ in a pure CO_2 atmosphere at 600°C and it was suggested the physisorption of CO_2 to the surface rather than carbonate formation (chemisorption). The samples tested were taken up to 950°C in a CO_2+H_2 atmosphere, and

this could explain the modest yet non-negligible presence of carbonates.[67]

The formation of the strontium carbonates could make the perovskite less stable, driving other elements, such as Mo, to give rise to new phases, which could justify the presence of $SrMoO_4$ on the diffractogram.

Comparing the diffractograms, it is seen that, besides the presence of undesired compounds, the perovskite phase is stable, meaning that it is possible to carry on with the cell testing with this material as electrode.

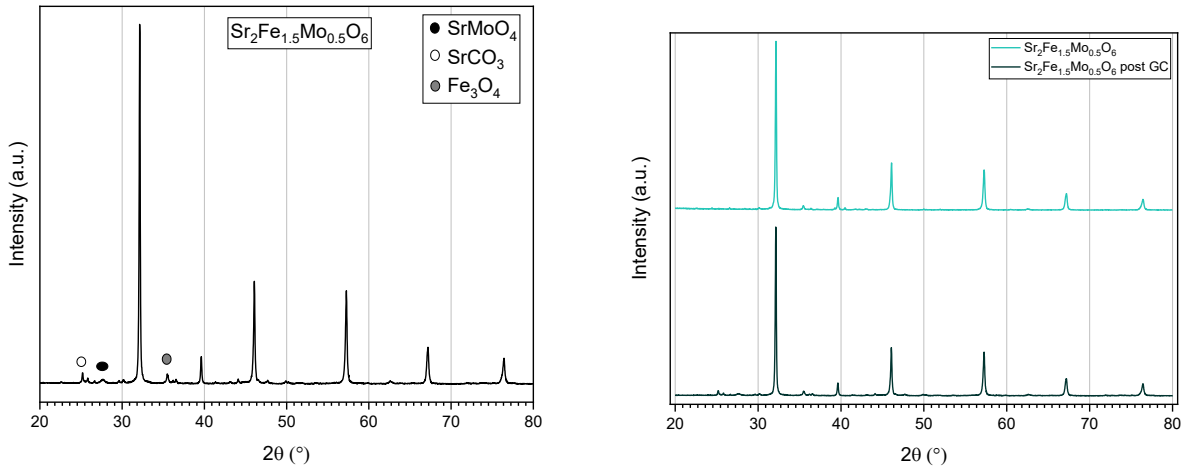

Diffractogram 5.2: on the left, XRD diffractogram of the SFM 1.5:0.5 material post-reaction, on the right, the pattern of the fresh (above) and post-reaction (below) material

5.2.2. X-Ray Photoelectron Spectroscopy (XPS)

The XPS analysis were performed keeping unchanged the experimental parameters used for the fresh samples and described in *Section 4.7*.

The qualitative-quantitative composition of all samples has again been studied after the RWGS reaction cycle with XPS, in order to better understand eventual segregation phenomena by means of a comparison between the fresh materials and the post-reaction ones. The more evident phenomenon observed after the reaction was the surface segregation of strontium cation, noticed not only from the quantitative analysis, in fact, the percentual increase is ~20%, but also through the XPS *spectrum 5.1*. From the high-resolution spectra, two main contributions are noted: the increasing of the signal of strontium oxides in SFM 1:1 (reported in literature [61] to be located at around 132.9 eV) and the addition of a signal in between the two former peaks, at around 133.4 eV for sample 1.5:0.5, which is

attributed to carbonates.[61] The tendency of this cation to produce carbonates has already been mentioned in *Section 5.2.1* and the graph (*Spectrum 5.2*) that compares the C 1s spectrum and confirms the enhanced presence of carbonates, is reported. The straight line is centred at 289 eV, which is the binding energy for $SrCO_3$ in NIST Database.[61]

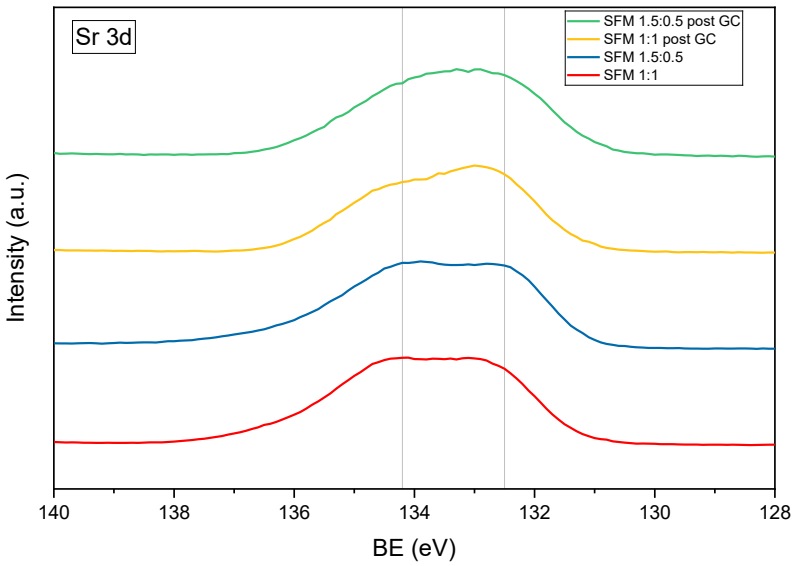

Spectrum 5.1: high resolution analysis of Sr3d peak of both materials (SFM 1:1 and SFM 1.5:0.5) before and after the reaction (post GC)

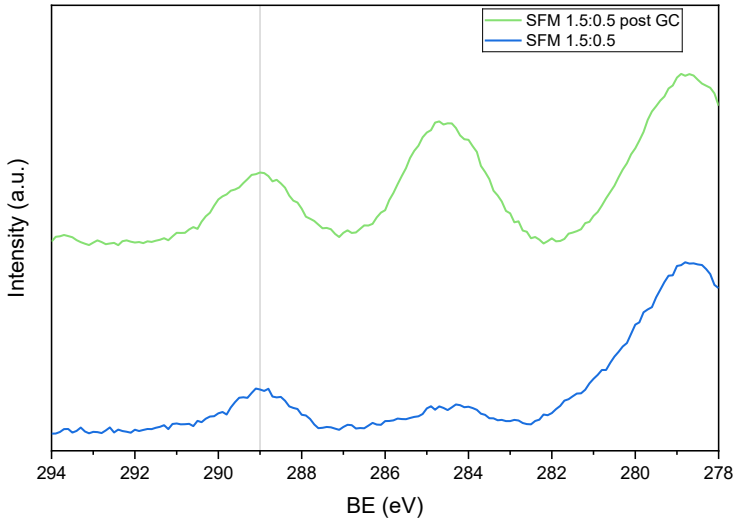

Spectrum 5.2: high resolution spectrum of C1s of SFM 1.5:0.5 before (below) and after (above) the reaction

Consistent results are also found in the O 1s high-resolution spectra. In fact, comparing the contributions of the spectrum in blue (SFM 1.5:0.5) with the green one (SFM 1.5:0.5 post GC), is noted the decreasing of the signal of metal oxides (~529-530 eV) and the increasing of metal carbonates (~531 eV), both phenomena probably correlated with the decreasing/formation of strontium oxides/carbonates.

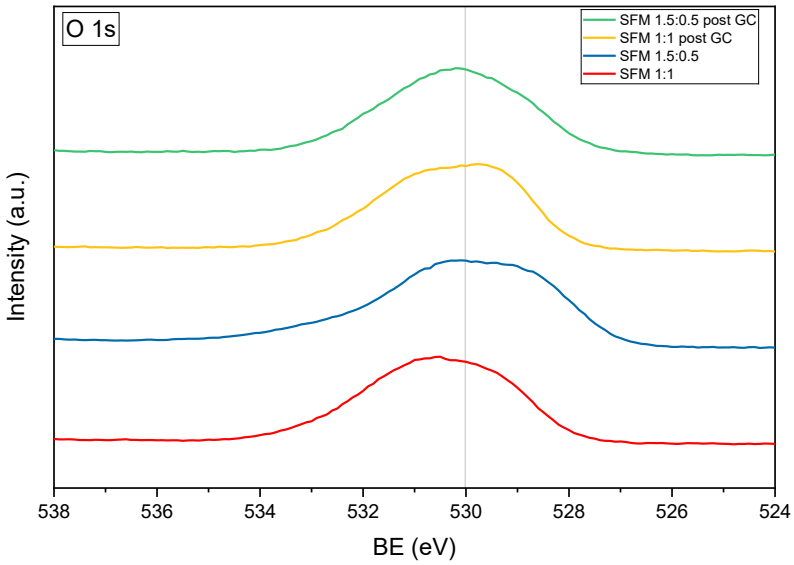

Spectrum 5.3: high resolution analysis of O 1s peak of both materials (SFM 1:1 and SFM 1.5:0.5) before and after the reaction (post GC)

For what concerns Mo, a broadening of the two peaks is noted, which is certainly attributable to the formation of species with different valence states (or different chemical environment). In particular, in SFM 1.5:0.5 post GC, a slight shift toward lower Binding Energy is noticed, probably due to the reduction of the sample, as during the thermocatalytic test, the atmosphere is at 5.6% H_2 up to 900°C.

A modest widening of the peaks is also observed for SFM 1:1 post GC, as well as a slight shift to higher Binding Energy compared to spectrum before the test (red and yellow spectra). This is probably due to oxidation of some of the species in the sample, once the material is exposed to CO_2, as $SrMoO_4$.

The quantity of Mo increases at the surface after the test, suggesting that, probably, other spurious phases are produced and this cation is involved in the catalytic activation.

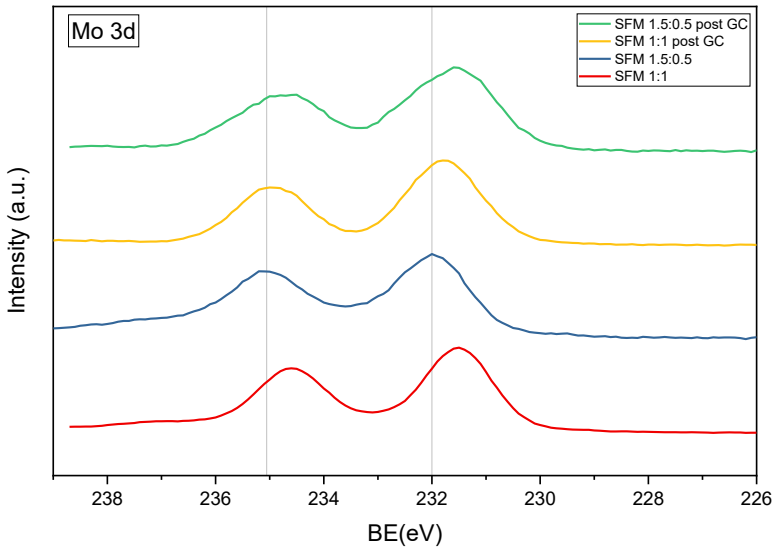

Spectrum 5.4: high resolution analysis of Mo3d peak of both materials (SFM 1:1 and SFM 1.5:0.5) before and after the reaction (post GC)

The high resolution spectrum of Fe does not change during the test, even though the signal is really weak. The peaks do not shift but the atomic percentage decreases by more than 60% in the case of SFM 1:1 and 50% in the case of SFM 1.5:0.5. This could depend on the migration of other elements to the surface (i.e. Sr or Mo), and corresponds to the drop of the Fe element in the surface, as reported in *Table 5.1 and 5.2*.

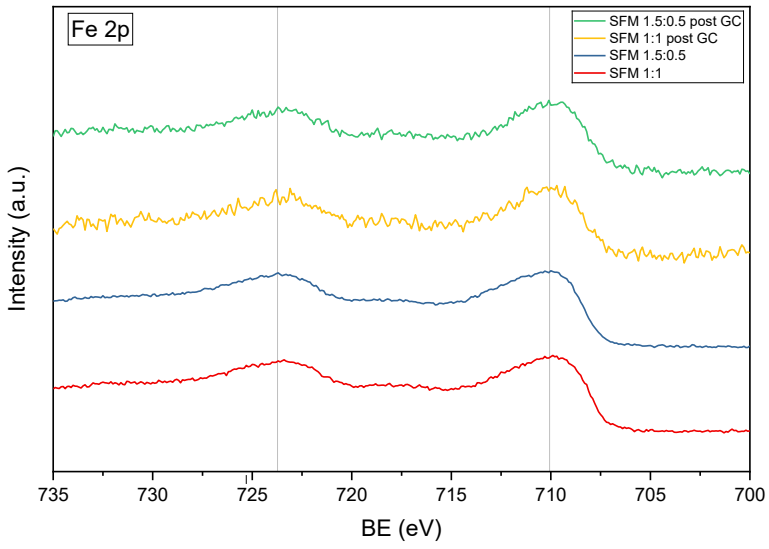

Spectrum 5.5: high resolution analysis of Fe2p peak of both materials (SFM 1:1 and SFM 1.5:0.5) before and after the reaction (post GC)

Table 5.1: comparison of theoretical and experimental percentage compositions of cations of SFM 1:1

Element	Theoretical (%)	EDX (%)	XPS (%)	XPS post GC (%)
Sr	50.0	46.3	46.2	59.3
Fe	25.0	30.5	29.1	10.9
Mo	25.0	23.2	24.7	29.8

Table 5.2: comparison of theoretical and experimental percentage compositions of cations of SFM 1.5:0.5

Element	Theoretical (%)	EDX (%)	XPS (%)	XPS post GC (%)
Sr	50.0	45.3	48.2	58.6
Fe	37.5	41.5	38.5	19.6
Mo	12.5	13.2	13.3	21.8

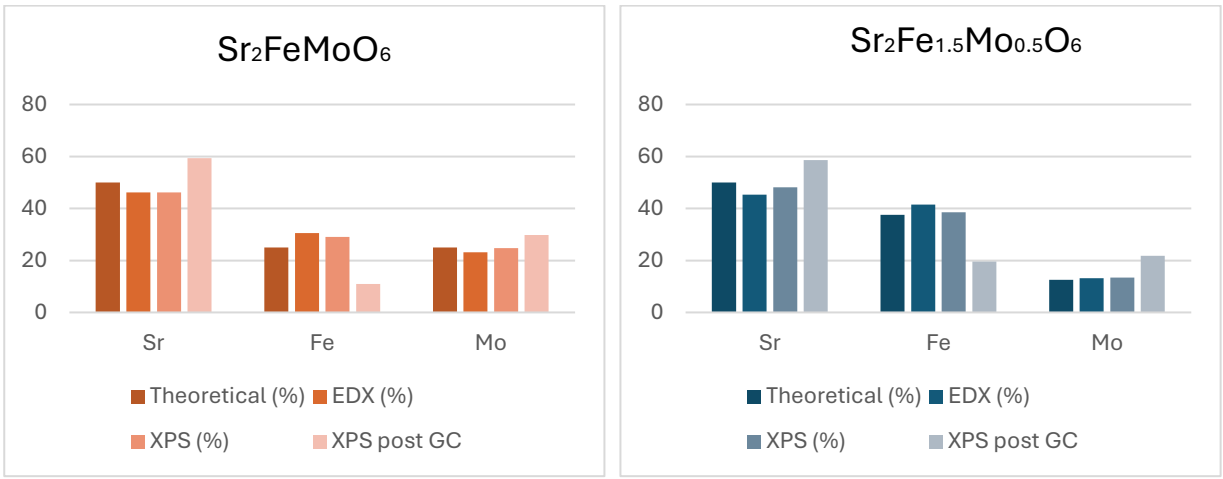

Figure 5.4: comparison of Mo, Fe and Sr percentage quantity theoretical, from XPS and EDX analysis in SFM 1:1 (on the left) and SFM 1.5:0.5 (on the right)

6. CELL DESIGN AND MANIFACTURING PROCESSES

The following chapter will be dedicated to the description of the cells' design and construction procedures, together with the technical issues that had to be overcome. In particular, a full description of the realisation of a symmetrical and single-cell will be carried out.

6.1. SOFC and SOEC configurations

The cell applications usually define the design of the device itself; nevertheless, among all the possible configurations two are the most used: the planar and the tubular design. In recent studies, however, it has been tried to overcome the limitations that are proper of these designs.

6.1.1. Tubular design [68,69]

Tubular design is usually employed in high temperature SOFCs and SOECs and is the most present in market-ready devices for stationary applications. It is made of a cathode tube, covered by a layer of electrolyte that is in turn coated with an anode layer, as shown in *Figure 6.1*.

This design has higher mechanical strength and facilitate sealing. The air is fed through the inside of the tube and is reduced to oxygen ions by the electrode, while outside a stream of H_2 will flow, in the case of SOFC configuration (*Figure 6.1*).

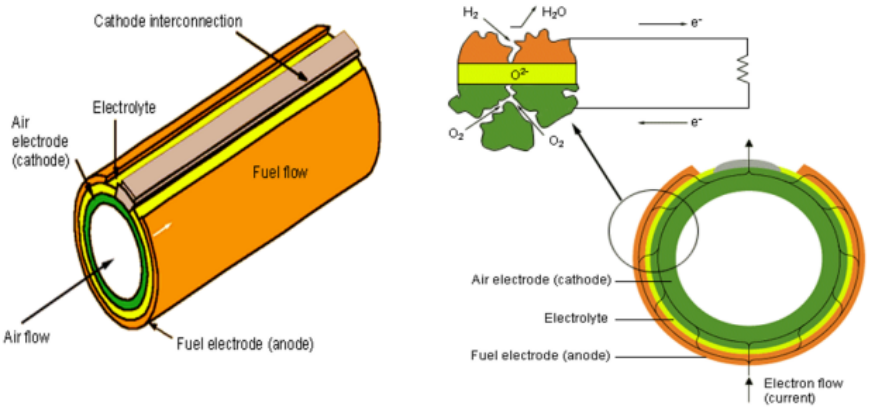

Figure 6.1: Tubular design with the air electrode as inner layer [100]

However, it is exceedingly true, that switching the air electrode with the fuel electrode, the flows swap in the same way, as shown in the following *Figure 6.2*.

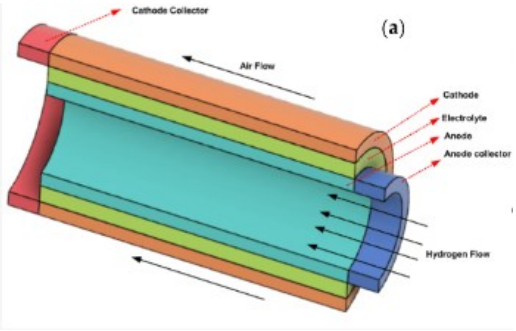

Figure 6.2: : Tubular design with the fuel electrode as inner layer [101]

Instead, in SOEC configuration, if the inner layer is always the cathode, the inner flow would be the steam (and carbon dioxide in case of co-electrolysis), which will be reduced to hydrogen and carbon monoxide. The oxygen gas is extracted from the outer layer of the tubular design.

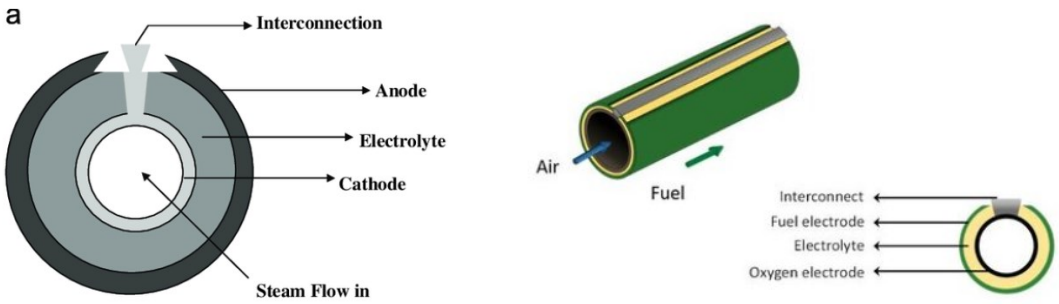

Figure 6.3: tubular configuration with fuel electrode|electrolyte|air electrode (on the left) and air electrode|electrolyte|fuel electrode (on the right) for a SOEC [70]

These types of cells can work for long periods under different operating conditions with less than 0.1% performance degradation per 1000 h of working-time, but with low power density (as high as 1 W/cm^2), making these devices not suitable for mobile applications. Nevertheless, some drawbacks are also present, the principal being the difficulty in the production of the ceramic cylinder with a good uniformity between the different layers.

6.1.2. Planar design

This configuration finds primary application in research due to its straightforward construction.

The planar arrangement comprises either a singular or multiple stacks, consisting of individual units or planar layers that are iteratively replicated. Illustrated in *Figure 6.4* (in

the case of SOFC configuration), the individual layer is constituted by the cell positioned at the structure centre and two interconnects flanking the core. This arrangement provides both structural integrity and pathways for fuel to access the two electrodes. Additionally, the interconnects function as current collectors. The design of the interconnects facilitates perpendicular (or parallel) flows of air and fuel, allowing for the creation of a compact stack.

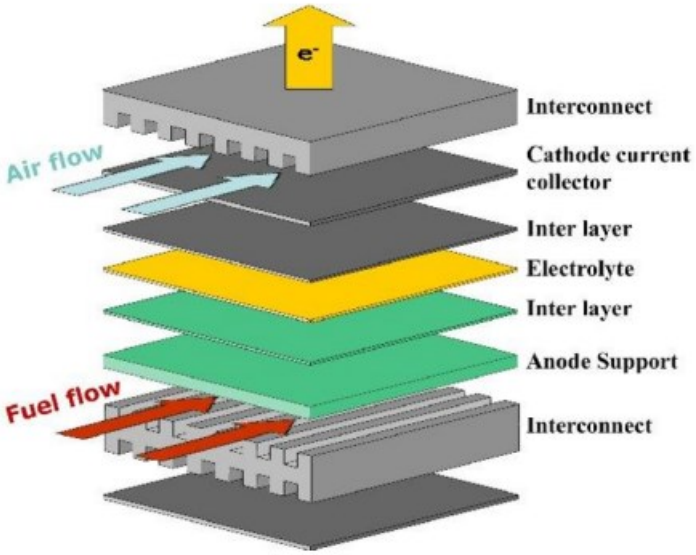

Figure 6.4: Planar design for SOFC and SOEC [102]

The planar design is preferred due to its better manufacturability and better electrochemical performance than tubular cells, this is because the distribution of gas species is more uniform.

Taking into account the above factor as well as easier mass production of planar cells, the planar system configuration is advantageous.

6.2. Cells construction

This work has opted for the button planar design due to its ease of implementation in the laboratory facilities. This configuration is commonly employed in research applications. The differences between this cell and the basic planar design are attributed to the smaller dimensions of the button planar and variations in electrical connections. The primary advantage of adopting this design is the minimal quantity of materials required for

constructing the device, making it suitable for laboratory-scale use but impractical for industrial applications due to its size.

The cell built in this way is called 'electrolyte-supported cell', in which the electrolyte (250 μm-1 mm) is between the fuel electrode and the oxygen electrode. Its advantages are their good mechanical robustness and better redox behaviour compared to electrode-supported cells. However, they exhibit high ohmic resistances due to the relatively thick electrolyte, leading to lower power densities and thus requiring high operating temperatures (above 800°C).

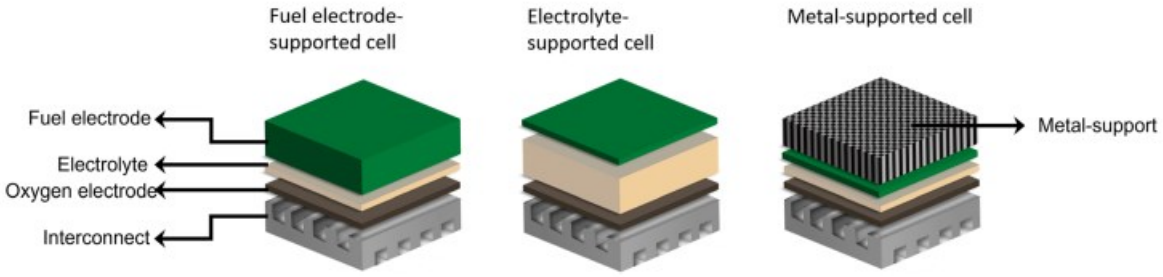

Figure 6.5: Planar cell designs and schematic representation of the three different cell support types: electrode-supported cells, electrolyte-supported cells, and metal-supported cells. [103]

6.3. Choice of the electrolyte: compatibility and adhesion tests

After a deep research in literature, several electrolytes were discarded. YSZ, which is the most used SOFC solid electrolyte, starts to react with the electrodes as low as 800°C and the main product is the scheelite $SrMoO_4$. [71] Other promising electrolytes are GDC (Gadolinium doper ceria), LDC (Lanthanum doped ceria) and SDC (Samarium doped ceria), with high conductivity values. However, they are mixed ion-electron conductors (MIE) suffering from a lower open-circuit voltage caused by an electron leakage current. Moreover, at temperatures up to 500 °C, Ce^{4+} ions can be reduced at the anode to Ce^{3+} enhancing electronic conductivity and causing addition lattice expansion.[52]

The last chance is LSGM (Strontium and magnesium-doped lanthanum gallate, $La_{0.8}Sr_{0.2}Ga_{0.8}Mg_{0.2}O_3$) whose compatibility with the electrodes was studied by Dos Santos-Gomez in the temperature range between 800°C and 1200°C and no appreciable peaks were found in the XRD diffractograms indicating that there is no formation of undesired phases at the interface between electrode and electrolyte. [72]This is very relevant because in case of

reaction at the interface, it is necessary the deposition of a buffer layer that can, however, reduce the cell performance and surely increase the device complexity. Another thing to consider is the fact that the Thermal Expansion Coefficient (TEC) for LSGM is found to be $11.2 \cdot 10^{-6}$/°C, which is very similar to the TEC found for Sr_2FeMoO_6: $13.9 \cdot 10^{-6}$/°C [73] and for $Sr_2Fe_{1.5}Mo_{0.5}O_6$ is $16.33 \cdot 10^{-6}$/°C. [74] This, in fact, means that if the values are similar, once they are heated up, the behaviour is similar for both the electrode and the electrolyte. Working with solid oxide cells and electrolysers mean that high temperatures are reached. The materials, when a change in temperature occurs, is subjected to stress, which can be compressive if the object would expand in the absence of the constraint and tensile if it would contract. When two materials, with similar TEC are put in contact, they compress or expanse in the same way, avoiding the stress, which could lead to the break of the cell.

Specifically, the specimens were created through the manual blending and grinding of electrodes material (SFM 1:1 and SFM 1.5:0.5) with LSGM powder – in a weight ratio of 50%-50%. In particular, the mixed powders of the samples and the electrolyte, were first subjected to calcination in air up to 600°C (ramp of 5 °C/min) for a dwell time of 1 h, and then a second calcination in a 5%H_2 reducing atmosphere (again ramp of 5°C/min) for 6 h at 1200 °C (*Figure 6.6*).

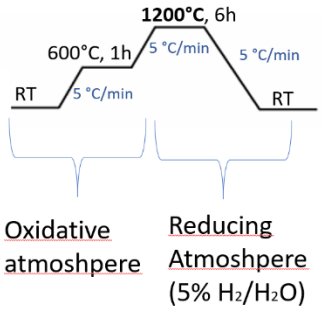

Figure 6.6: condition for compatibility test up to 1200 °C

After several attempts and research in the literature, the deposition of the electrode on the electrolyte was performed up to 1200 °C, with a first step up to 600 °C in oxidative atmosphere in order to ensure the complete removal of any residual of carbonium compounds in the materials.

As visible from *Diffractograms 6.1*, a non-negligible phase of $SrGaLaO_4$ is formed. In fact, Don Santos-Gomez et al. [72], who tested SNM (Sr_2NiMoO_6) with LSGM noticed that below 800 °C no appreciable reaction is detected; however, above 1000°C several reaction products are visible, with the identification of $LaSrGaO_4$ and $SrLaGa_3O_7$, as found in this case.

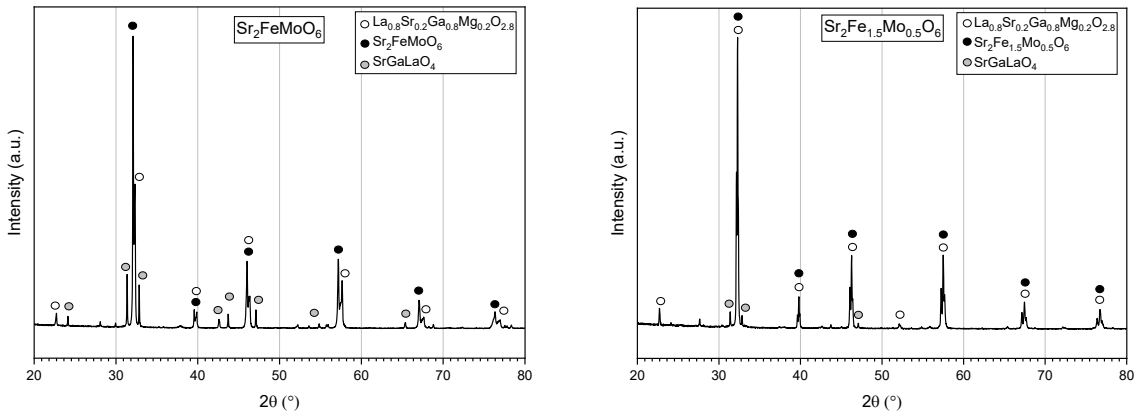

Diffractogram 6.1: XRD diffractograms after the compatibility test of SFM 1:1 (on the left) and SFM 1.5:0.5 (on the right)

The cell realization procedure was thus modified and, after several tests, the ideal protocol has been determined, decreasing the maximum temperature and the heating rate in order to let the single elements adapt themself in the more stable phases at these condition, i.e. the perovskite phases. This will diminish the kinetic velocity of the migration.

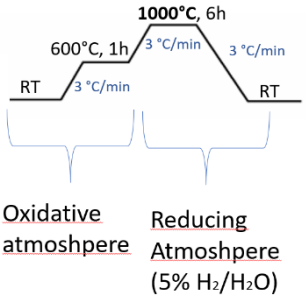

Figure 6.7: condition for compatibility test up to 1000 °C

Working in these conditions, the situation is more favourable. In particular, the SFM 1:1 material has some spurious phases, as $LaSrGaO_4$ and $SrMoO_4$, but in small quantity compared to what was observed above (*Diffractogram 6.3*).

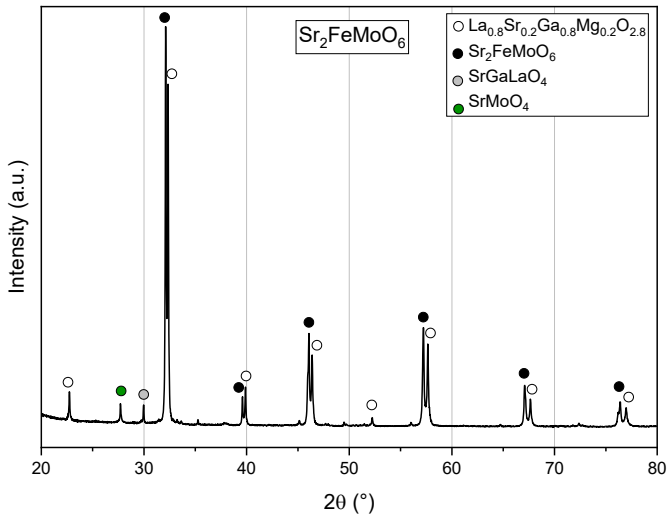

Diffractogram 6.3: XRD Diffractogram of SFM 1:1 after the compatibility test

With SFM 1.5:0.5 (*Diffractogram 6.2*) the impurities already mentioned were not observed, but a form of lanthanum oxide (La_2O_3) is evidenced. However, literature data suggest that this phase should not ruin the cell. Moreover, it was found that when La_2O_3 was added on Ni-Co films used as metallic interconnection, its presence improved the electrical performance. [75]

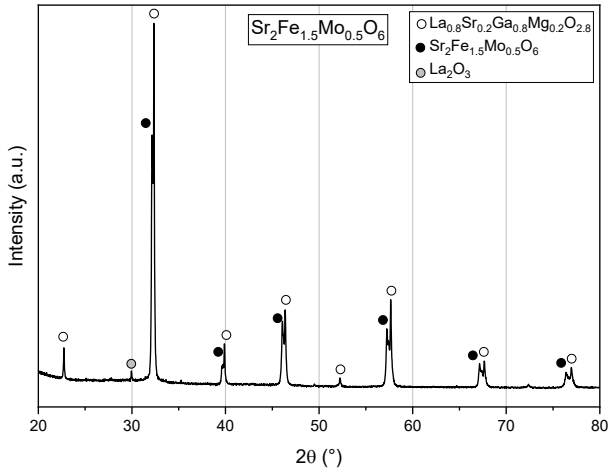

Diffractogram 6.2: XRD Diffractogram of SFM 1.5:0.5 after the compatibility test

The following steps were carried out to detailly test the reversibility of the materials and then ultimate the protocol for the preparation of the cell.

6.4. Reversibility of the materials

The test of the reversibility was made in order to verify that the electrodes do not change when they undergo the steps of deposition on the electrolyte.

The three steps are:

I. The deposition of the electrode on the electrolyte, up to 600°C in air, then up to 1000 °C in wet hydrogen
II. The drying of Au paste placed on the cell and the elimination of the potential carbonium compounds, up to 600 °C in air
III. The first step again: the deposition of the electrode on the electrolyte, up to 600 °C in air, and then up to 1000 °C in wet hydrogen. This step is made in order to verify the reversibility of the material

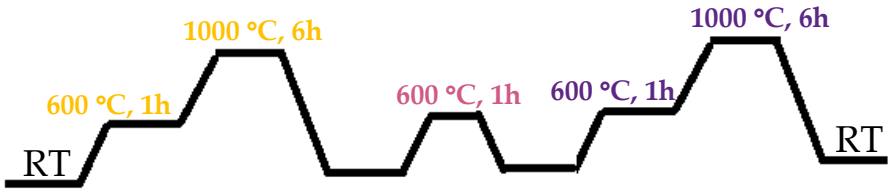

Figure 6.8: condition for reversibility test

These conditions were tested for both powders, and what comes out from the *Diffractogram 6.5* is that the materials do not change after undergoing both environments: in air (oxidative atmosphere) and in wet hydrogen (reductive atmosphere). A further confirmation is done after comparing the diffractograms of the sample at step III and before the test (*Diffractogram 6.4*).

This is surely interesting, considering that these materials will be used as both anode and cathode in reversible Solid Oxide cells (r-SOCs).

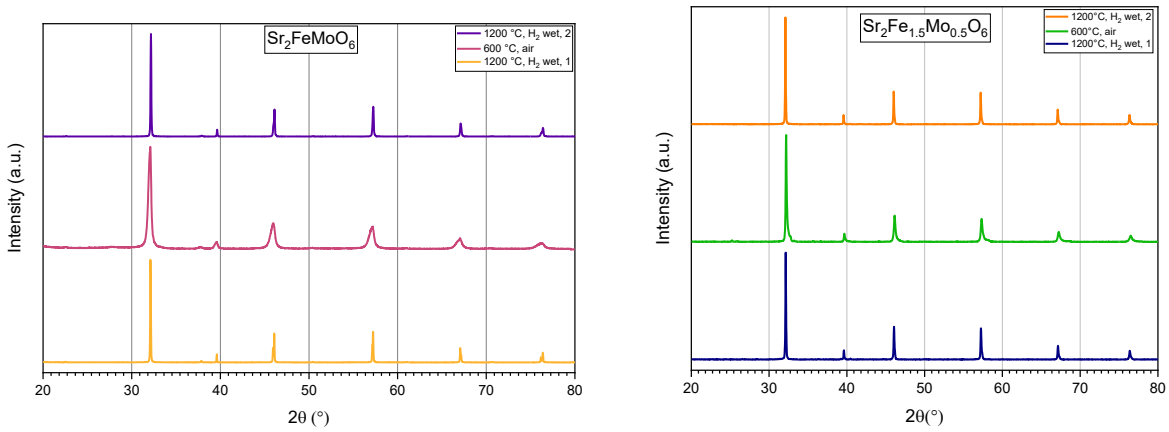

Diffractogram 6.5: XRD diffractograms of SFM 1:1 (on the left) and SFM 1.5:0.5 (on the right)

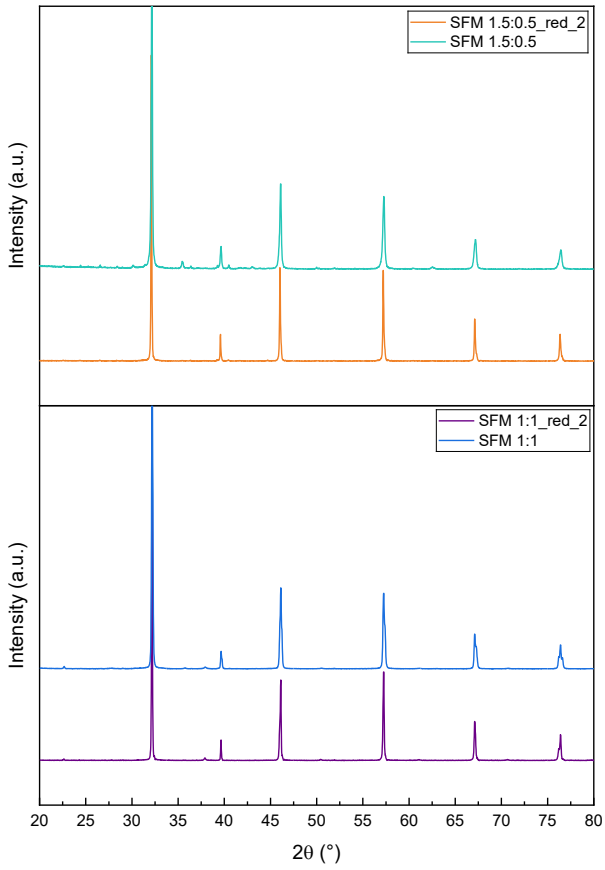

Diffractogram 6.4: a comparison of the diffractograms before the test (below) and after the III step (above). The samples are SFM 1:1 on the bottom and SFM 1.5:0.5 on the top

6.5. Cell preparation and mounting

The preparation of the cell involves four different steps:

I. Production of the pellet

2.0g of LSGM powders was uniaxially pressed into a circular pellet, with a 25 mm diameter, through a hydraulic press. The proper pressure applied was found, after several attempts, to be 3.5 tons.

The pellets were then treated in air at 1100°C (5°C/min), reaching, at 3°C/min, 1500°C for 6 hours. At this point, sintered pellets were sanded until obtaining a smooth surface and finally cleaned with ethanol in an ultrasonic bath before the electrode deposition (*Figure 6.9, on the left*). Pellets are 900 μm thick.

II. The deposition of the electrodes

The deposition of the electrodes was made through the process of tape casting (*Figure 6.9, in the centre*). Ink preparation involves in mixing powder of the synthesized materials, a polymer binder (α-terpineol) and a pore former (carbon soot) in a ratio: 2:1:0.09, in order to obtain an ink with a proper viscosity to be deposit. Two inks with the powders of SFM 1:1 and SFM 1.5:0.5 were prepared. After the coat of ink is applied, the electrodes are sintered with two steps: the first up to 600°C (in air, ramp of 3°C/min), the second until 1000°C (ramp of 3°C/min) for 6 hours, in a wet hydrogen atmosphere.

III. Coating of a layer of gold paste

The gold paste plays the role of electrons collector provided by an homogenous electrons film (*Figure 6.9, on the right*). Gold mesh was brushed on the sintered electrode and then dried at 150 °C for 10 minutes in air.

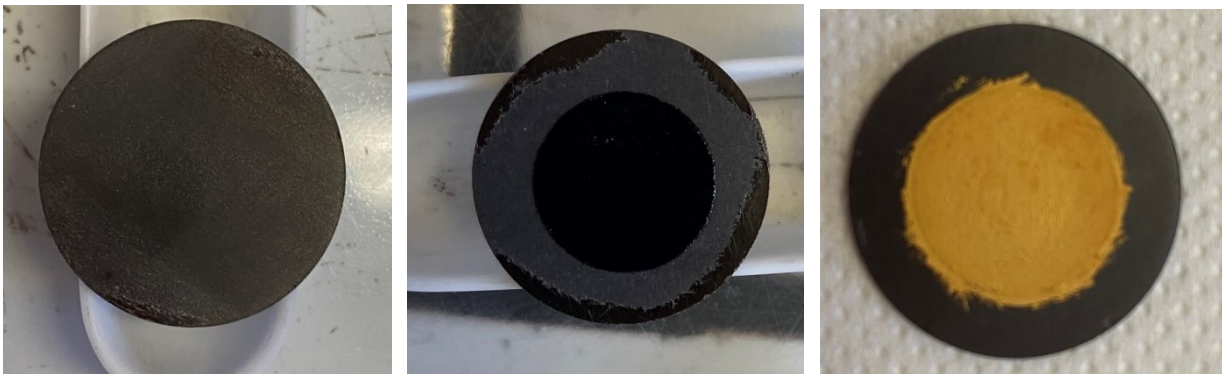

Figure 6.9: on the left, the electrolyte after the lapping, in the centre, the deposition of the electrode, and on the left, the coating of a layer of a gold paste

IV. Addition of a Au filament

The electrical connection between the cell and the external circuit and the cell prototype was ensured by gold wires, catalytically inactive for our purpose, placed as in *Figure 6.10*. They were attached to both the cell sides with a ceramic paste. A final treatment at 600 °C (ramp of 3°C/min), with a dwell time of 30 minutes, is essential for drying the paste and eliminating organic residuals present in the gold paste.

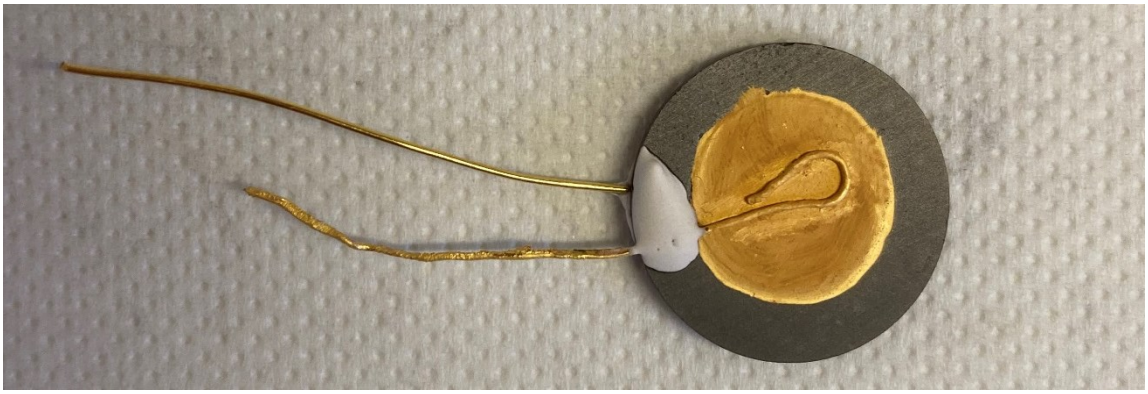

Figure 6.10: the prepared cell, with the addition of an Au filament

Once the cell is ready, it was finally mounted vertically (for a symmetrical test), in a dedicated single chamber set-up , in which the cell is supported by an α-alumina DEGUSSIT AL23 tube covered by a quartz tube to isolate the chamber.

The symmetrical tests were carried out with the aim to isolate the performance of a specific electrode material under open-circuit conditions and the cell is prepared using the same electrode (SFM 1:1 in one cell and SFM 1.5:0.5 in the other) in both sides. [76]

For the complete cell test, in contrast, the electrode/electrolyte/electrode core is mounted horizontally and sealed with a ceramic glue to separate the fuel from the air compartment. (*Figure 6.11*). The cell was then tested with linear polarization and chronopotentiometry measurements, to study its performance (e.g. Power density for SOFC or Faradic efficiency for SOEC).

The fuel, which in *Figure 6.11,* corresponds to red arrow, enters at the bottom of the set-up in case of symmetrical and complete measurements. The other flux, which in figure coincides with the green arrows, in case of complete analysis, is the air (with SOFC and SOEC modality). The blue arrows indicate the exhaust gases.

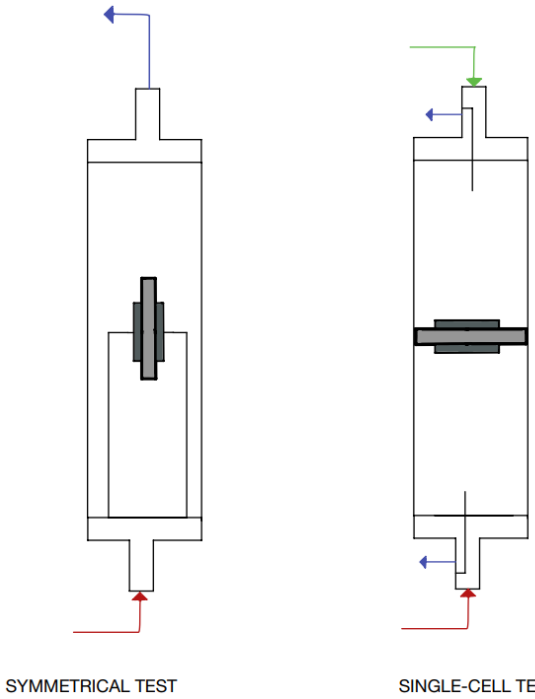

Figure 6.11: configurational set-up of the symmetrical test(on the left) and the complete test (on the right)

Figure 6.12: the experimental set-up for a symmetrical test (on the left) and a complete test (on the right)

Platinum wires present in the ceramic tube have been connected to the gold filament connected to the cell, to establish an electron pathway. A AISI 316 (austenitic stell with molybdenum alloy) oven has been used. The oven has an internal cavity, where the tube with the cell is inserted, with two K-type thermocouples, in case of the complete system. In the case of symmetrical setup, there is only K-type thermocouple.

7. ELECTROCHEMICAL CHARACTERIZATION OF the CELLS

In this chapter, the electrochemical characterization of cells made with SFM 1:1 and SFM 1.5:0.5 electrodes is accomplished and discussed.

Four different types of measurements are taken:

I. Electrochemical Impedance Spectroscopy (EIS) with SYMMETRICAL CELLS
II. Linear Polarization (LP) with SINGLE-CELLS
III. Linear Swipe Voltammetry Potentiostatic (LSVP) with SINGLE-CELLS
IV. Chrono voltammetry (CV) with SINGLE-CELLS

The analyses were performed in a single chamber device using a PGSTAT 302 Autolab Frequency Response Analyzer. The measuring facility set up was developed by IMPACT research group.

7.1. EIS measurements

Electrochemical impedance spectroscopy (EIS) is widely used and offers kinetic and mechanistic data of various electrochemical systems in SOFC and SOEC research field. EIS is based on the perturbation of an electrochemical system in equilibrium or steady state, via the application of a sinusoidal signal (AC voltage or current) over a wide range of frequencies and what is registered is the sinusoidal response of the system.

After the measurement is over, an analysis to find the values of an electrical resistance is carried out through circuit modelling software. However, since the resistance is valid only in the case of an ideal resistor and here the circuit possesses a more complex behaviour, the resistance is called impedance. Further explanations about the theory beyond EIS are provided in the Appendix.

The measurements are carried out at equilibrium conditions (OCV, Open Circuit Voltage), in the frequency range of 10^{-2}-10^{-6} Hz with a signal amplitude of 20 mV.

The calculations are then performed with ZView software, by analysing the data collected as an equivalent electrical circuit, in order to retrieve numerical values for all the components.

Each material has been tested with two different atmospheres, to reproduce the conditions of SOFC and SOEC analysis:

I. 10% H_2 diluted in Ar, to recreate the environment in a SOFC
II. 4.4% CO_2/5.6% wet H_2 (3% H_2O of the total output gases: 100 sccm, standard cubic centimetres per minute), diluted in Ar, to recreate the one of a SOEC

The necessity to produce a wet atmosphere for the SOEC measurement is carried out with the use of a bubbler. After calculations, considering the saturation vapor pressure of water, the total gas flow rate and the temperature, it is found out that the percentage of water fluxing when 100 sccm passes through a bubbler at 25°C is 3.13%.

The temperature range was between 600-850 °C, with 50°C steps in between; a stabilization of 15 minutes was necessary in every step in order to achieve the steady state required to acquire EIS data. EIS were collected by using the symmetrical cell, as previously described and schematized in *Figure 6.11*.

7.1.1. EIS results

The following sections report the Nyquist plots obtained through Zview software and the calculations for ASR (Area-Specific Resistance, $\Omega \cdot cm^2$). ASR allows to achieve important outcomes relative to the electrical resistances of the electrodes in the gas atmosphere. State-of-art Ni/YSZ electrode exhibits ASR values within the range of 0.01 $\Omega \cdot cm^2$; for what concern the material studied in this work, it is around 0.3-0.4 $\Omega \cdot cm^2$.

ASR was calculated as follows:

$$ASR = \frac{R_p \cdot A_{electrode}}{2}$$

Equation 59

Where R_P is the polarization resistance, $A_{electrode}$ is the area of the electrode and in the denominator, the value 2 is because the cell is symmetrical and has the same electrode in both sides.

EIS measurements enable the calculation of electrode polarization resistance (R_P) and the electrolyte ohmic resistance (R_o). These two values can be calculated by fitting the experimental data with the equivalent circuit. Each electrical element describes a physical

process that occurs in operating condition. In this work, the attention was focused on the electrode and the relative electrochemical processes.

7.1.1.1.H_2 -in Ar- fuel

The first series of electrochemical test is performed in a 10% H_2 wet (3% H_2O)/90% Ar gas mixture with both symmetrical cells made with SFM 1:1 and SFM 1.5:0.5 as electrodes.

The choice of working with a wet hydrogen atmosphere is due to the behaviour of the material once it is tested in only hydrogen environment. As seen in *Section 4.3.2*, the 5% H_2 atmosphere it too drastic for the sample. Then, after the reaction in SOEC takes place, the environment could be wet, as some water could have been stayed inside the compartment. Thus, these conditions are not unusual.

The two following graphs report the Nyquist plot for SFM 1:1 and SFM 1.5:0.5 symmetric cell.

The series at 650 °C was not reported for SFM 1:1 due to unforeseen instrumental problem.

Something interesting is that from a qualitative analysis of the graphs, the impedance values of SFM 1.5:0.5 are around one-tenth of SFM 1:1. This is clearly of interest concerning the performance of the cells and the comparison of two materials.

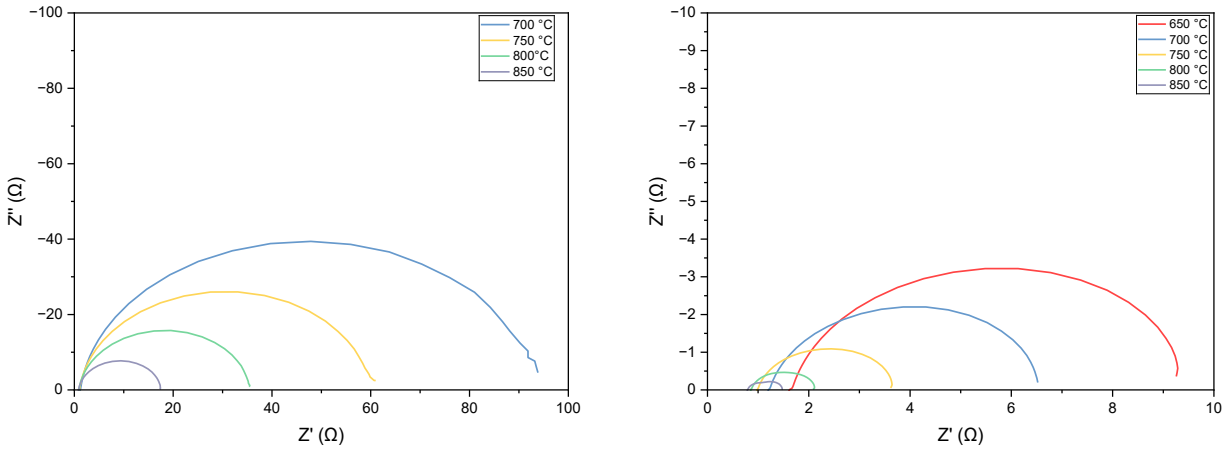

Graph 7.1: Nyquist plot of SFM 1:1 (on the left) and SFM 1.5:0.5 (on the right), in 10%H_2 wet fuel

The circuit that was utilized during the measurement is composed of a resistor, in series with two sub-circuits made of a resistance in parallel with a CPE. Every unity stands for a process, so according to the plot, two processes are supposed to happen.

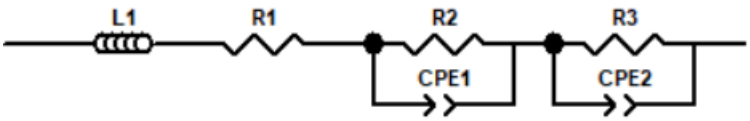

Figure 7.2: equivalent circuit utilized for the curves fitting

L_1 is the inductive impedance, which appears below the x-axis (Z' positive, -Z'' negative), it is mainly associated with the length and the positioning of the cell cables, the contacts between the cables and the electrodes, and instrumental artifacts.[77] R_1 simulate the resistance of the electrolyte and so the ohmic resistance (R_o). The two subunits are made up of a resistance (R) and a constant phase element (CPE). CPE behaves as an ideal capacitor and its origin has been widely attributed to the surface roughness of solid electrodes, which causes an uneven distribution of various properties, such as the solution resistances, interfacial capacitances, of current densities etc, across the electrode surface. [77]

The sums of the values obtained by the plot for the two subunits, provide the total polarization resistance (R_P). This parameter encompasses the resistance related to concentration polarization (an effect coming from mass-transfer or gas-diffusion phenomena), and the effective interfacial polarization resistance.

The ASR calculated through *Equation 59* are reported in the following *Table 7.1*.

As expected, the R_o are similar in both cases, since it only depends on the electrolyte and not on the materials of the electrode materials.

The behaviour of the materials are very unlike, once compared at the same temperature. Mo tends to interact with Fe via the Fe-O-Mo bridge structure and the change transfer is developed from Fe to Mo species, leading to an electron-deficient state of Fe.[66] The decreasing of the electron density of Fe, so lower electronic conductivity, is shown for the material with higher quantity of Mo, SFM 1:1.

The value of ASR for SFM 1.5:0.5 found in the literature is 0.27 $\Omega \cdot cm^2$ at 800 °C under a hydrogen wet atmosphere. The difference between the value found in literature and the one obtained from this cell stands on the thickness of the electrolyte, as in the article it was 265 μm, while for the cell used in this test, it was 900 μm. [4]

Table 7.1: R_o and ASR values for SFM 1:1 and SFM 1.5:0.5, in 10% H_2 wet

10% H_2 wet	SFM 1:1		SFM 1.5:0.5	
	R_o (Ω)	ASR (Ω·cm²)	R_o (Ω)	ASR (Ω·cm²)
650 °C	-	-	1.61	4.60
700 °C	1.17	51.1	1.20	3.13
750 °C	0.98	33.6	1.00	1.58
800 °C	0.88	19.9	0.86	0.97
850 °C	0.82	9.72	0.79	0.51

7.1.1.2. $H_2 + CO_2$ – in Ar- fuel

The second part of the cells tests has implied the change of the environment to 4.4 %CO_2+5.6 H_2% wet+90% Ar. The choice of this atmosphere is in order to recreate the SOEC environment on the fuel electrode and to test if there is, as expected, a change in the cell's performance.

As in the case of the just mentioned atmosphere, two processes take place, so the equivalent circuit remains untouched. The impedances decrease as the temperature increases, due to a boost of the process kinetics, implying that the processes are temperature dependent.

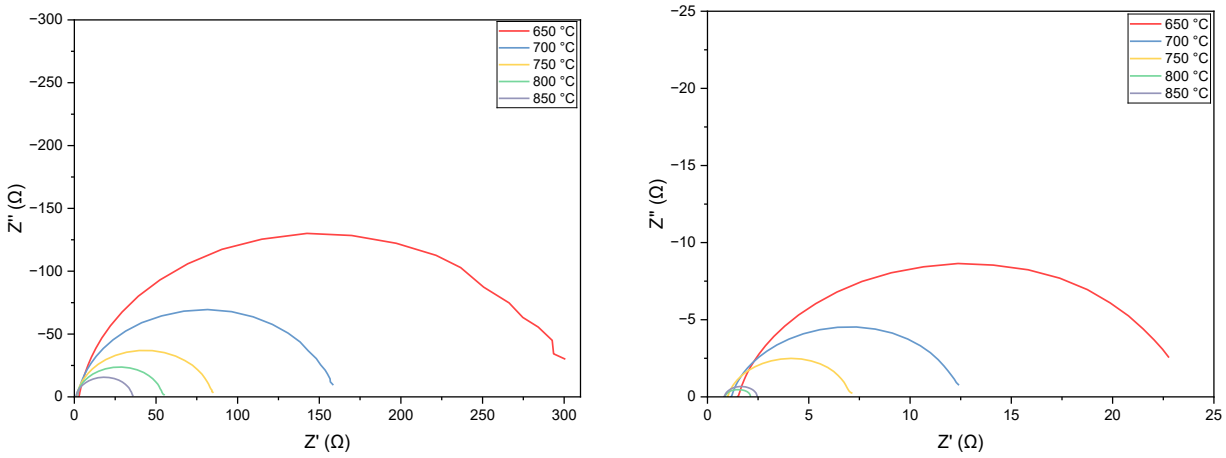

Graph 7.3: Nyquist plot of SFM 1:1 (on the left) and SFM 1.5:0.5 (on the right), in 5.6%H2 wet-4.4%CO2 fuel

The ASR values are calculated as before, with the same equivalent circuit in *Figure 7.2* and reported in *Table 7.2*.

The R_o of the two cells, in this case, are different, once they have been compared at the same temperature. This could be due to the different thickness of the electrolyte.

Table 7.2: Ro and ASR values for SFM 1:1 and SFM 1.5:0.5, in 5.6% H_2 wet-4.4%CO_2

5.6% H_2 wet +4.4 % CO_2	**SFM 1:1**		**SFM 1.5:0.5**	
	R_o (Ω)	ASR (Ω·cm^2)	R_o (Ω)	ASR (Ω·cm^2)
650 °C	2.58	166	1.48	12.5
700 °C	1.68	88.6	1.15	6.44
750 °C	1.27	47.1	0.99	3.50
800 °C	1.06	30.1	0.88	1.87
850 °C	0.95	19.7	0.82	0.94

Comparing the results of the *Tables 7.1* and *7.2*, the same trend for the materials is noticed, and in particular, SFM 1.5:0.5 has lower ASR than SFM 1:1. Moreover, a big change is made by the environment, as its change shows a redoubling of the values. This could be explained once considering the charge transfer between Fe and Mo, which leads the Fe of decreasing the electron density and increasing the surface positive charge. This has been shown to be particularly problematic in CO and H_2 environments, which are not adsorbed and hence inhibits their conversion. [66]

The activation energy calculated for LSGM through the plot of Arrhenius, are reported to be the same in both of the atmospheres and larger (1.4 eV) than what is found in literature[78] (1.1 eV, but with a different atmosphere). Unfortunately, it was not possible to make further comparisons, as the values in the literature are meagre.

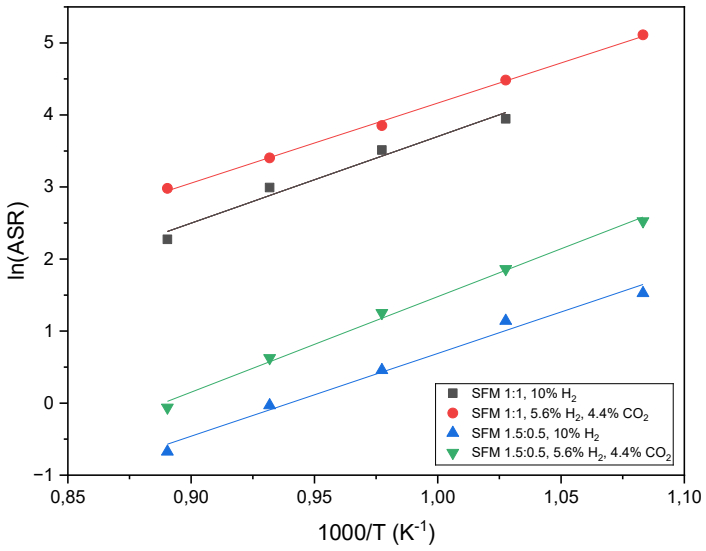

Graph 7.4: Arrhenius plot for the materials

7.2. SOFC measurements

The electrochemical cell performance during SOFC mode is performed varying the voltage applied from 0.1 to -0.8V VS OCV, with a scan rate 0.01 V/s and a step every 0.001 V, registering the change of current densities. The outcomes show the I-V characteristics and the corresponding power densities for each cell.

The choice of the voltage range has been done in order to be on the right side of the following graph (*Figure 7.5*), i.e. working in the SOFC mode, and to check eventual voltage drop. The OCV is the intercept of the straight line.

The set-up used is the one for single-cell test (*Fig. 6.11*).

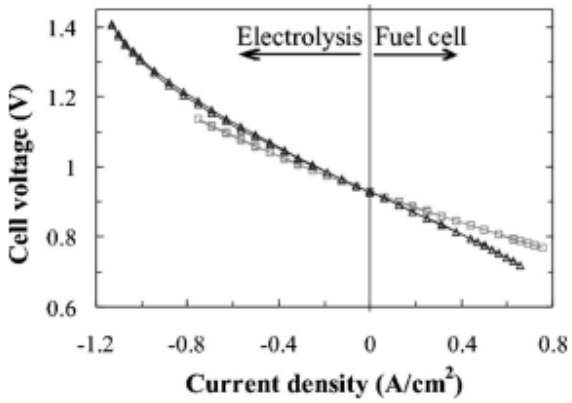

Figure 7.5: I-V graph in electrolysis (on the left) and fuel cell (on the right) modality [80]

The effect of the temperature has also been tested, analysing the cells in the range between 600-850 °C, with 50°C steps in between; a stabilization of 15 minutes was necessary in every step, in order to stabilize the flux and avoid any type of mistake because of temperature.

The analyses were performed feeding the anode compartment with a 10% H_2 wet/90% Ar atmosphere, and the cathode compartment with air.

The cells were prepared with the two materials: SFM 1:1 and SFM 1.5:0.5, as both anode and cathode.

A facsimile of I vs V and power density graph is reported in *Figure 7.6*. Normally, the fuel cells are designed to operate slightly at the left with respect to the maximum in the power density curve, in order to achieve a good compromise between cell efficiency, low capital cost and operational stability. Under these conditions, the maximum loss is due to the electrolyte ohmic polarization (R_o), and the cathode and anode activation losses are also considerable. [9]

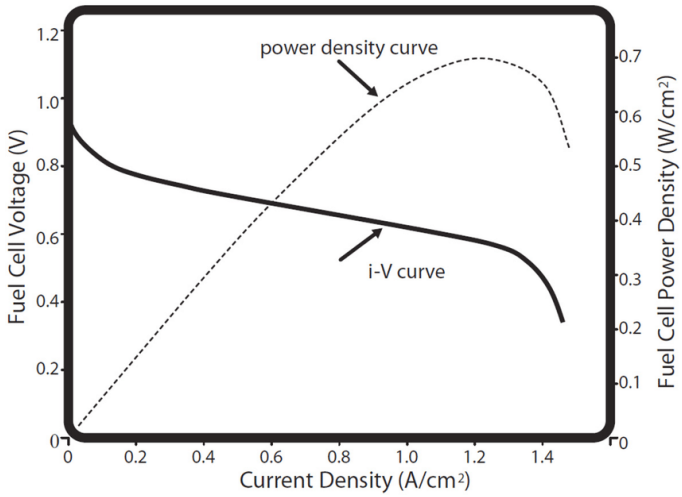

Figure 7.6: Combining I-V and Power density curves in a SOFC measurements [9]

7.3.1. SOFC data

First, the graph of SFM 1:1 is reported. The current (mA) and the power (mW) are presented as current density (mA·cm^{-2}) and power density (mW·cm^{-2}). The area used for the calculation is the one of the electrode (1.13 cm^2).

The maximum of the power density produced is summarized in *Table 7.3*:

Table 7.3: Maximum Power density for SFM 1:1, SOFC modality, 10%H_2 wet

SFM 1:1	
Temperature (°C)	Maximum Power density (mW·cm^{-2})
650	2.07
700	6.53
750	9.39
800	15.23
850	24.63

The I vs V graph shows a pseudo-linear current-voltage behaviour, especially at high temperatures. The OCV values varies between 0.85-0.95 V at 650-850 °C. The OCV values were close to the theoretical Nernst potential at the corresponding temperature, portending that the tested cells were well sealed without gas leakage.

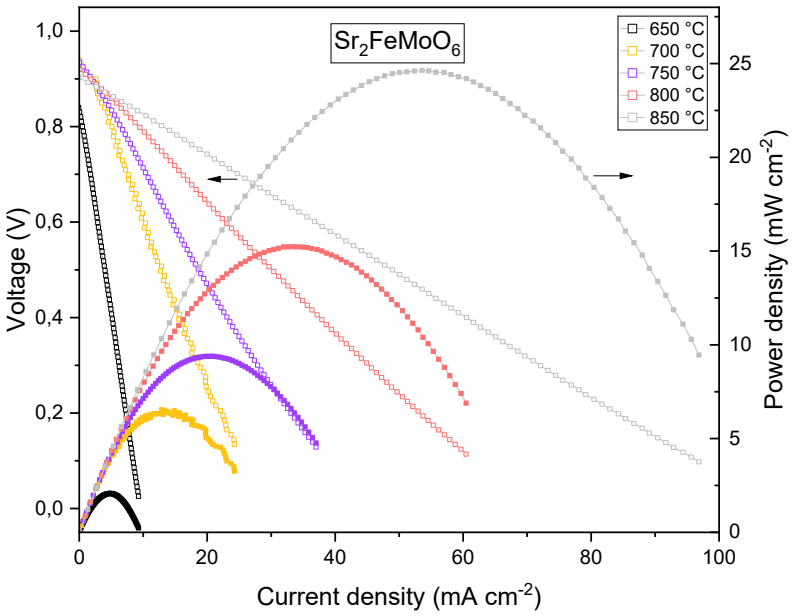

Graph 7.7: I-V and I-Power density curves for SFM 1:1, SOFC modality, 10%H_2 wet

The results obtained for SFM 1.5:0.5 are reported in *Graph 7.9*.

The maximum power densities (MPD) are higher with SFM 1.5:0.5 cell, with an increase of MPD of 50-60% with respect to SFM 1:1 at the same temperature. This is related to the fact that ASR are higher with SFM 1:1, so the cell has lower performance.

Table 7.4: Maximum Power density for SFM 1.5:0.5, SOFC modality, 10%H_2 wet

SFM 1.5:0.5	
Temperature (°C)	Maximum Power density (mW·cm^{-2})
650	7.19
700	13.88
750	24.02
800	40.13
850	58.08

The results seems promising, however comparing them with the literature[4], for a symmetrical cell SFM|LSGM|SFM, in a wet hydrogen atmosphere at 900 °C a power densities of 835 mW cm^{-2} is found. The difference in between these values is related to the

thickness of the electrolyte, as in the literature the pellet was 265 μm, while the one used in this test was around 900 μm, more than three times.

The I-V graph of SFM 1.5:0.5 is reported (*Graph 7.8*) and analysed as follows.

At high temperatures (i.e. 800°C and 850 °C), the I vs V graph is initially linear and characterized by ohmic loss but then the concentration loss increases. This loss is due to the mass transfer resistance to the flow of the reactants and the products. [79]

At lower temperatures (i.e. 650 °C and 700 °C), the graph is very different from the all the others, as from the slope of the curves, the main loss is due to the activation.

However, comparing the cells at the same temperature and atmosphere, the cell with SFM 1.5:0.5 have always a better performance compared to the other.

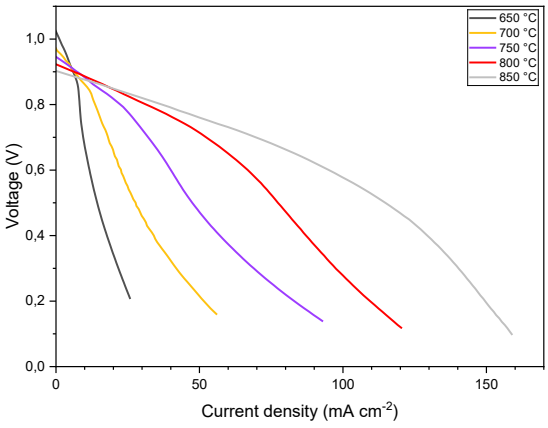

Graph 7.8: I-V curve for SFM 1.5:0.5, SOFC modality, 10%H_2 wet

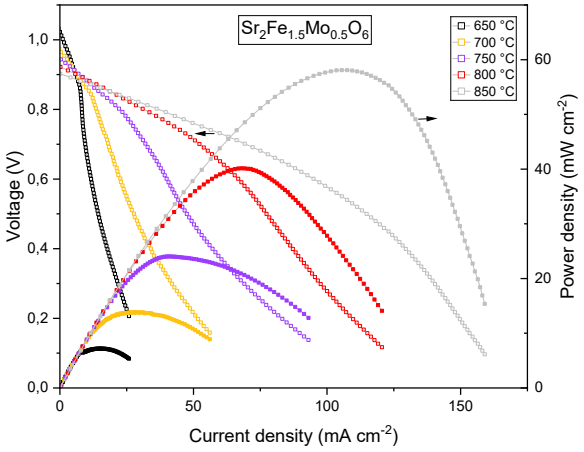

Graph 7.9: I-V and I-Power density curves for SFM 1.5:0.5, SOFC modality, 10%H_2 wet

7.3. SOEC measurements [80]

The cells are then tested in SOEC modality. Both of the cells were first used in SOFC modality and then tested in SOEC, which is doubly interesting for their use as reversible cells.

The electrochemical cell performance as SOEC was performed:

1. Varying the voltage applied from 0.0 V to 1.5V (vs OCV), with a scan rate 0.1 V/s and a step every 0.00244s and registering the change of current densities. The outcomes show the I-V characteristics. This technique is called Linear Sweep Voltammetry (LSV).

2. Applying a voltage obtained by LSV and registering the current density for a time lapse of 900s.

The choice of the voltage range of LSV was because, the work area is on the left side of *Graph 7.6.* The OCV is the intercept of the straight line.

The set-up used is the one for single-cell test (*Figure 6.11*).

The effect of the temperature has also been tested, analysing the cells in the range between 600-850 °C, with 50°C steps in between; a stabilization of 15 minutes was necessary in each step, in order to stabilize the flux and avoid any type of mistake because of temperature.

The analyses were performed feeding the cathode compartment with a 5.6% H_2 wet (3% H_2O)/4.4%CO_2/90%Ar atmosphere, and the anode compartment with the static ambient air.

7.3.1. SOEC data

Two series of measurements are collected:

I. I vs V graphs, through LSV technique
II. Chronopotentiometry

7.3.1.1. I vs V graphs

Graph 7.10 and 7.11 represent the I-V curved measured for the two materials as a function of temperature. The OCV values are reported as follows:

Table 7.5: OCV values obtained for SFM 1:1 and SFM 1.5:0.5 in 5.6%H_2 wet-4.4% CO_2 atmosphere

SFM 1:1		**SFM 1.5:0.5**	
Temperature (°C)	OCV (V)	**Temperature (°C)**	OCV (V)
650	0.290	**650**	0.962
700	0.42	**700**	0.929
750	0.792	**750**	0.900
800	0.830	**800**	0.907
850	0.850	**850**	0.894

A dissimilar behaviour has been noticed, as OCV increase when working with SFM 1:1, while is constant with SFM 1.5:0.5.

As found in literature, the growth of OCV has been noted to be related to the R_P values decreasing.[81] This means that once the temperatures rise, several side reactions could happen that can increase or decrease the real potential of the cell.

Graph 7.8 shows the typical behaviour of the I-V curve determined by the activation, ohmic and concentration polarization in SOEC. The activation term is reflected by a slight increased slope at small current densities, which is noticed in particular at 650 °C and 700°C.[82] However, the curve at higher temperatures (750-850 °C) has more linear performance compared to the other (650-750 °C). This is also probably due to the presence of ohmic losses of the cell.

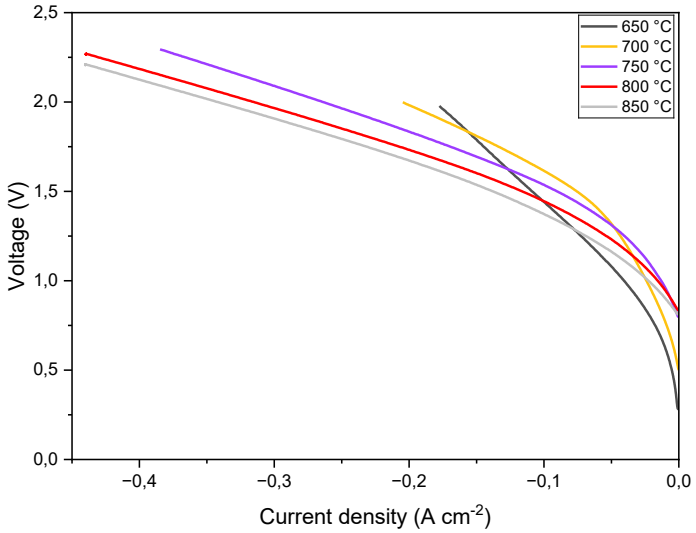

Graph 7.10: I- curve for SFM 1:1, SOEC modality, 5.6% H_2 wet-4.4% CO_2

The I-V curve of the SFM 1.5:0.5 electrode cell has a more linear behaviour to the other one with SFM 1:1 and it is probably characterized of only ohmic losses. However, the slight curving of the graphs at 650°C-700°C-750°C is probably due to activation losses.

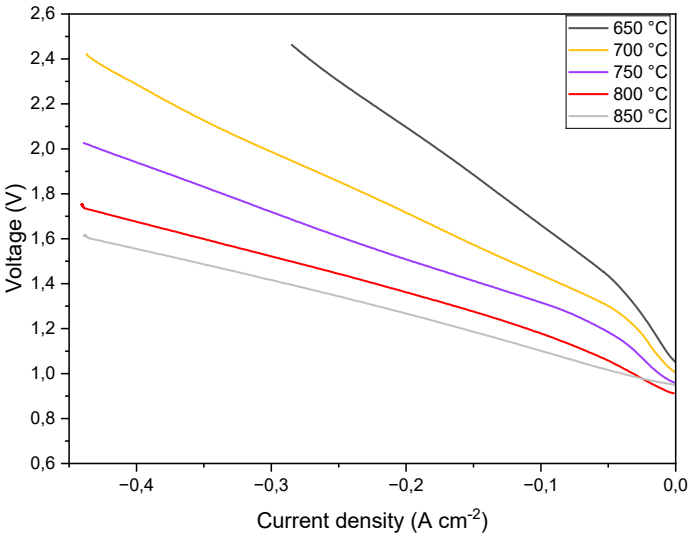

Graph 7.11: I-V curve for SFM 1.5:0.5, SOEC modality, 5.6% H_2 wet-4.4% CO_2

7.3.1.2. Chronopotentiometry

The chronopotentiometry is a galvanostatic method in which the current is held at the constant level for a given period of time. This technique is used for the characterization of the kinetics of the cell, the performance and the durability. During this thesis the test was performed for 900s, but in the literature it has been used even for more than 1000h.

The current applied is taken considering the linear behaviour found out in LSV measurements.

For SFM 1:1 complete cell, the analysis at 650 °C and 700 °C have not been performed due to unforeseen instrumental challenges. In any case, the corresponding current was chosen when the potential is around 1.5 eV, in order to be at potential higher than 1.23 eV and 1.33 V (respectively, the reversible voltage for the splitting of H_2O and CO_2, at 25°C).

For both cells it is noticed that an increase of temperature leads to a decrease of the voltage produced. This could be related to the same relationship that link the increase of the OCV with decreasing of temperature. [83]

At the same condition (0.25 A applied for SFM 1:1 and SFM 1.5:0.5 at 850 °C), the second cell produce higher voltage (0.89 V vs 0.79 V).

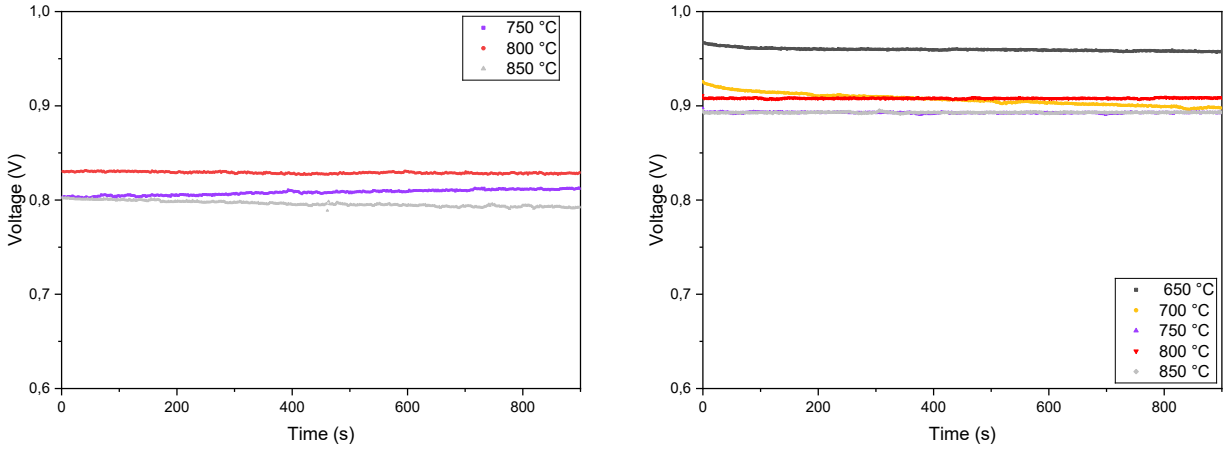

Graph 7.12: Chronopotentiometry of SFM 1:1 (on the left) and SFM 1.5:0.5 (on the right)

The outlet gases from the cathode compartment were then analysed with Agilent 990 MicroGC with Ar/He carrier, with a sampling time of 20 s and injections time of 50 ms. This is made in order to quantify the amount of CO_2 reduced and the amount of CO and H_2 produced during the applying of constant current with chronoamperometry analysis.

The feed is the same tested with LSV measurements: at the cathode compartment the mixture is 5.6% H_2 wet (3% H_2O)/4.4%CO_2/90%Ar, and the anode compartment is fed with the static ambient air.

The analyses are performed with both cells (with SFM 1.5:0.5 as anode/cathode and SFM 1:1 anode/cathode); however, the outcomes from SFM 1:1 were not collected properly due to some leakages of the tube that connected the set-up with the MicroGC.

The results of SFM 1.5:0.5 were collected and reported as follows.

The arrows point the measurements in which the current density was applied and so the electrolysis reaction was expected to take place.

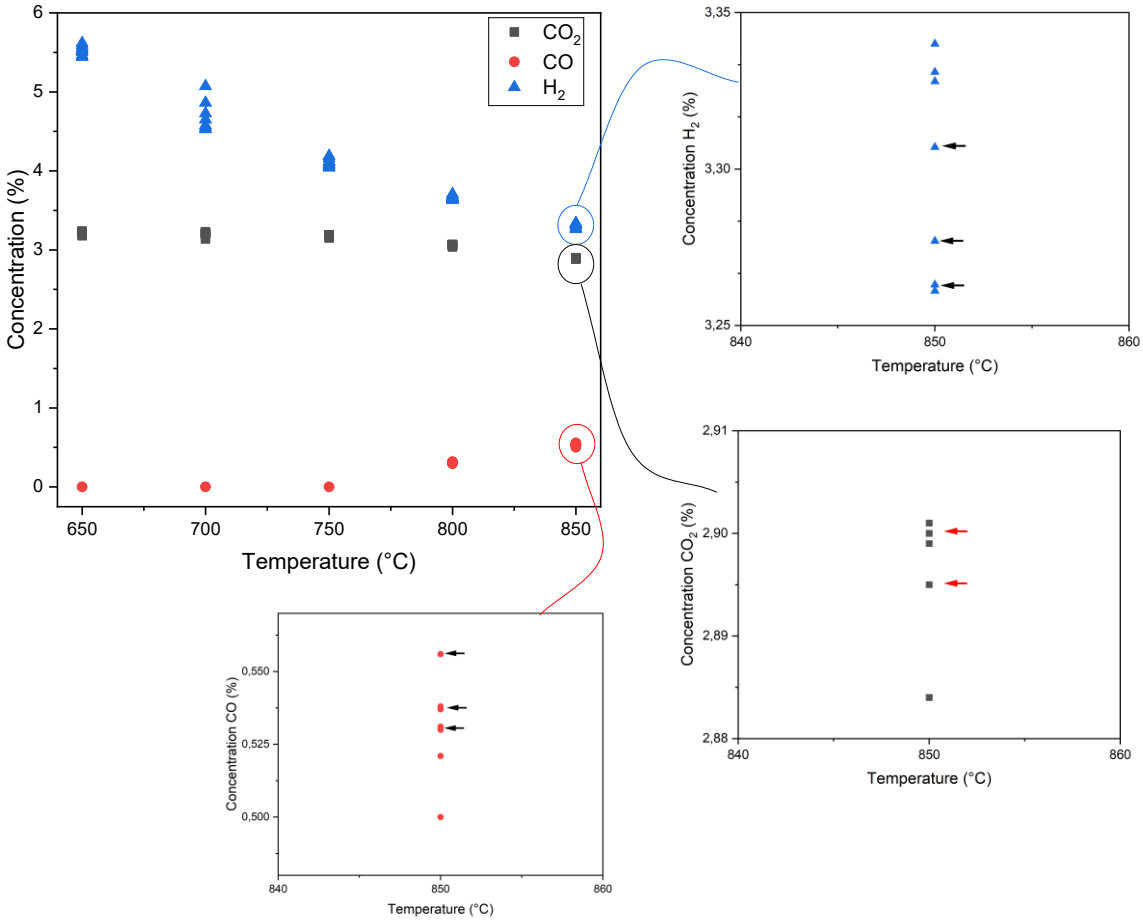

Graph 7.13: Concentration (%) vs Temperature (°C) of CO_2, CO and H_2 for SFM 1.5:0.5, in SOEC modality

The outcomes of the *Graph 7.13* are:

- CO_2 decrease with the increasing of the temperature, which could be due to the reduction of carbon dioxide by means of hydrogen, produced from hydrolysis of water or the incoming gases, or due the thermocatalytic reaction
- The quantity of CO increase, so the reduction of CO_2 takes place.
- A decreasing of H_2 has been observed, this is surely because of the reduction of CO_2. However, with that instrumental set-up is very challenging to say how much hydrogen is produced due to water hydrolysis.

The Faradaic efficiency is then calculated, with the following equation: [84]

$$FE_{CO} = \frac{e^{-} \cdot v \cdot C_{CO} \cdot F}{I \cdot A \cdot V_m} \cdot 100$$

Equation 60

Where e^- is the number of electrons involved in the reaction (2 for CO_2 reduction), v is the total gas flow rate at the inlet of the MicroGC (50 sccm), C_{CO} is the concentration of CO detected by the instrument, F is the Faraday constant (96485 C/mol), I is the actual current

density applied, A is the electrode area (1.13 cm^2), V_m is the molar volume (22.4 L/mol). The faradaic efficiency will be calculated only at 800 °C and 850 °C, as at the other temperatures, zero CO was detected.

Table 7.6: Faradaic efficiency of CO for SFM 1.5:0.5 at 800 °C and 850 °C

Temperature (°C)	**Concentration of CO (vol)**	**Current density (mA cm^{-2})**	**Faradaic efficiency CO (%)**
800 °C	0.003	285.4	6.8
850 °C	0.005	221.2	15.2

The results are different if compared to the literature, where at an applied potential of 1.4 V, the Faradaic efficiency is around 97.5% with a 100% CO_2 atmosphere.
However, the condition are rather different, so a proper comparison could have been made only with the same circumstances. Unfortunately, it was not possible to make further comparisons, as the values in the literature are meagre.

CONCLUSION

The increasing demand for renewable energies and the necessity to reduce climate change are some of the most important concerns nowadays.

This is not an individual need, but it should be shared with everybody, as climate issues are at the centre of social studies, politics and the economy.

This thesis begins with the goal of advancing renewable energy production and reducing one of the primary greenhouse gases: CO_2.

This work specifically focused on the synthesis, characterization, and lab-scale testing of perovskite-based electrodes that are stable in both reducing and oxidative atmospheres. These electrodes are designed to operate in both Solid Oxide Electrolysis Cell (SOEC) mode and Solid Oxide Fuel Cell (SOFC) mode using CO_2 and water. In SOEC mode, the cells can function as energy storage systems by producing hydrogen and carbon monoxide (syngas). In SOFC mode, they can generate energy by producing hydrogen, often referred to as the "fuel of the future" by *Forbes* and other global media. This dual-functionality system is known as reversible Solid Oxide Cells (r-SOCs).

In particular, the target material was the $Sr_2Fe_{1+x}Mo_{1-x}O_6$ (SFM, where x can be x=0, 0.5) double perovskite family, a promising electrode materials' family that has gained interest lately.

SFM has been considered a very promising anode and cathode material for reversible solid oxide cells operating with CO and CO_2.

For the synthesis of the materials, the Pechini route, a wet chemistry method, was utilized. It has been chosen to synthesize two double perovskite, one with a higher amount of Fe and lower of Mo (SFM 1.5:0.5) and the other with the same stoichiometric quantity of Fe and Mo (SFM 1:1), in order to discriminate which one works better considering the catalytic activity and the performance as SOEC and SOFC and so to understand the role played by these two cations in electrocatalysis.

XRD analysis were performed to understand which pathway (in oxidative or reductive atmosphere) can be preferred to ensure the production of the purest perovskitic phase. In

the end, the proper synthesis protocol is composed of a first step at 900 °C for 4 h in air, and a second one in 5%H_2 wet atmosphere at 900 °C for 8 h.

A H_2-TPR analysis is carried out to study the oxidation state of the cations inside the double perovskite structure, and it was found that Fe is probably the first element to reduce, with two peaks at 413°C (Fe(IV) to Fe (III)) and 503 °C (Fe(III) to Fe(II)), and a broader peak at 730 °C was ascribed to Mo (Mo(VI) to Mo(V/IV)). The reduction of Fe and Mo to metallic phases are found at around 900 °C.

Then, SEM characterization was performed, noting a coral-like structure for both of the materials at 25x magnification; however, looking closely, the particles were completely different, characterized by a more rounded shape with a lower amount of Mo (SFM 1.5:0.5), while the particles of SFM 1:1 -characterized by a higher quantity of Mo- show polyhedral and faceted shapes, typical of materials with greater amount of Mo, as found in literature.[55,60]

EDX and XPS quantitative analysis both confirmed the tendency of Fe to segregate within the first micrometres and on the surface, as the experimental values were higher compared to the nominal ones. For what concerns Sr and Mo, different behaviours were found, as Mo tends to move to the surface only in SFM 1.5:0.5 sample, while in general Sr has lower experimental values compared to the nominal ones, meaning that a lower quantity of Sr is found within the first micrometres and in the surface. The tendency of Sr or Mo to not form any other spurious compounds, other than the perovskite, is confirmed by the XPS qualitative analysis.

Finally, the SSA (Specific Surface Area) and PSD (Pore Size Distribution) are tested, confirming the presence of mesopores and the higher SSA for SFM 1:1 (4.1 m^2/g) then SFM 1.5:0.5 (3.2 m^2/g).

The catalytic performance of SFM 1.5:0.5 and SFM 1:1 is evaluated with the test of RWGS reaction. Both of the materials shows similar trend for CO_2 conversion and CO yield, however, the %CO yield is interesting to mention, as it is 51% for SFM 1:1 and 56% for SFM 1.5:0.5, meaning that the materials have different selectivity throughout the CO production. The latter-mentioned material seems more promising, even though analysing its post

reaction XRD diffractogram, several spurious phases have been found, such as $SrCO_3$, Fe_3O_4 and $SrMoO_4$. They have been also confirmed by XPS spectra, which highlight the presence of carbonates (verified even in the C1s spectra) and the broadening of the Mo peaks, emphasizing the existence of other phases.

The tendency of Sr to segregate and form carbonates for SFM 1.5:0.5 has also been noted in XPS quantitative analysis, as its experimental value increases by more than 20% compared to the starting material. Moreover, the amount of Fe decreases substantially, probably due to the segregation of other cations, i.e. Sr and Mo.

For what concerns the preparation of the cell, after the compatibility test, the electrolyte chosen was LSGM and no buffer layers were added. Moreover, the pathways include a first step of oxidative atmosphere up to 600°C, in order to eliminate the carbon compounds present, and then a wet reductive atmosphere (5% H_2/H_2O) up to 1000 °C, with a linear ramp of 3 °C/min, to deposit the electrode on the electrolyte, in an environment which is suitable for the material.

The cells were all prepared as symmetrical cells, using both for anode and cathode the SFM 1:1 and SFM 1.5:0.5 materials.

Several electrochemical tests were performed, with the aim of both studying the ohmic and polarisation resistance, and the electrochemical performance, in both of the modalities: SOEC and SOFC.

By EIS measurements, the resistances of the cell were analysed.

Very promising results were found, in particular for SFM 1.5:0.5 cell, in both of the environments (10% H_2 and 5.6% H_2 wet, 4.4% CO_2), reported in the following tables.

Table 0.1: Comparison of R_o and ASR of SFM 1.5:0.5 material in the different environments

	10% H_2 wet		**5.6% H_2 wet + 4.4%CO_2**	
	SFM 1.5:0.5		**SFM 1.5:0.5**	
	R_o (Ω)	ASR (Ω·cm²)	R_o (Ω)	ASR (Ω·cm²)
650 °C	1.61	4.60	1.48	12.5
700 °C	1.20	3.13	1.15	6.44
750 °C	1.00	1.58	0.99	3.50
800 °C	0.86	0.97	0.88	1.87
850 °C	0.79	0.51	0.82	0.94

As well as the resistance, even the MPDs (Maximum Power Densities) determined in SOFC measurement, were particularly interesting and promising, once compared with the literature. [4]

Table 0.2: Comparison of Maximum Power density for SFM 1:1 and SFM 1.5:0.5 in 10% H_2

	SFM 1:1	**SFM 1.5:0.5**
Temperature (°C)	**Maximum Power density (mW·cm^{-2})**	**Maximum Power density (mW·cm^{-2})**
650	2.07	7.19
700	6.53	13.88
750	9.39	24.02
800	15.23	40.13
850	24.63	58.08

In the end, the SOEC tests were performed. From the I vs V graphs, what was noticed is the different behaviour of the material at different temperatures, in particular, at low temperatures the curve is characterized by activation losses, while at higher temperatures, the losses are mainly ohmic.

In the meantime of the chronopotentiometry, the concentration of CO_2, CO and H_2 was detected via Micro-GC instrument. The outcomes were the production of CO and the

reduction of CO_2, as well as the amount of H_2. This behaviour is symptomatic of the probable reduction of carbon dioxide, by means of part of the hydrogen added in the inlet gases, to stabilize the material. With this setup and this initial concentration is not straightforward to understand how much the hydrogen is produced.

However, the Faradaic efficiency of CO of SFM 1.5:0.5 was then calculated at 800°C and 850 °C, and the results are 6.8% and 15.2% respectively.

Table 0.3: Faradaic efficiency of CO for SFM 1.5:0.5 at 800 °C and 850 °C

Temperature (°C)	**Concentration of CO (vol)**	**Current density (mA cm^{-2})**	**Faradaic efficiency CO (%)**
800 °C	0.003	285.4	6.8
850 °C	0.005	221.2	15.2

What's next?

The results until now collected are particularly interesting and promising for the future utilization of these materials as both anode and cathode in reversible Solid Oxide Cells (r-SOCs). However further analysis should be made in order to implement the available cells. First of all, the SFM 1.5:0.5 cell looks more encouraging than SFM 1:1, which require some adjustments to reach the performance of the lower Mo content material.

To better understand the selectivity of SFM 1.5:0.5 towards the single reaction, i.e. water splitting, CO_2 reduction, the single paths should be tested, eventually increasing the initial concentration and checking if this could help to increase also the yield.

Moreover, several articles underline the possibility of enhancing the performance and the strength of the material, via the impregnation or the ex-solution of metals, including Co, Fe and Ni, onto the oxide matrix, to improve the various energy-related catalytic reactions, including CO_2 electrolysis, water splitting, hydrogen oxidization, and so on. [85]

Focussing on the preparation of the cell, a thinner electrolyte would be fundamental. This could have been made through a lower quantity of powder of electrolyte, but then there could be some problem related to the mechanical strength of this cells. The comparison of

different realization procedures, moreover, could be interesting, as spray coating electrolyte onto a prefabricated anode support.[86] However, in this way, the cells are then anode-supported and not electrolyte-supported, with the advantages and the drawback already mentioned in *Section 6.2.*

Finally, some adjustments regarding the set-up measurements could be considered to minimize the leakages of the instruments. Thus, it could be a point to move closer, for example, the cell heater and the detection system, i.e. the MicroGC, to reduce possible losses of the products. This problem were experienced during the SOEC test of SFM 1:1 and it was the reason why it was not possible to measure the concentration of CO, and the percentage detected was not consistent with the inlet gases.

To scale up this process for cell production, certain steps could be performed *in-situ*. For instance, the electrode preparation could be adjusted by modifying the flux, facilitated by acquiring a new setup capable of exposure to different atmospheres. This approach could eliminate the need for gold paste by employing an alternative electron collector.

APPENDIX

I. XRD [87]

Powder X-ray diffraction (XRD) is a common characterization technique for materials. Analysis of a sample by powder XRD provides important information that is complementary to various microscopic and spectroscopic methods, such as phase identification, sample purity, crystallite size, and, in some cases, morphology.

This technique is composed of an incident beam (X-rays produced by the source), which interacts with a crystalline material and is diffracted by the sample and enters the detector. The Bragg's law is used to explain why the cleavage faces of crystals appear to reflect X-ray beams at certain angles of incidence (theta, θ), and it is used only when constructive interference occurs.

$$n \cdot \lambda = 2 \cdot d \cdot sin\theta$$

Equation 61

Where d is the distance between atomic layers in a crystal, λ is the wavelength of the incident X-ray beam, θ is the Bragg's angle (the angle between the beam radius and the plane).

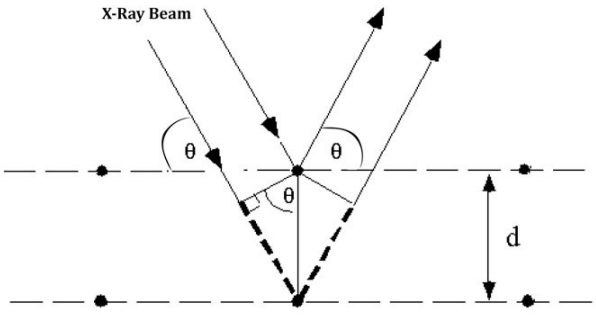

Figure 0.1: X-rays diffraction [87]

Constructive and destructive interference of X-rays diffracted from each plane generates the diffraction pattern, which is typical for each material.

In the experimental configuration used in this thesis work, the information XRD provides are related to the bulk of the material. The penetration depth of this technique depends on the angle of incidence of the X-ray beam with the surface. Usually it is around 20-100μm.

XRD was used during this thesis to find the crystal structure of an unknown material and to determine the orientation of a single crystal or grain.

It can be used to measure the size of the crystallite, through the Scherrer equation:

$$D = \frac{K\lambda}{\beta cos\theta}$$

Equation 62

Where D is the mean size of the ordered (crystalline) domain, K the shape factor (the typical value is 0.9, but varies with the actual shape of the crystallite), λ is the wavelength of the incident X-ray beam, β is the broadening of half the maximum intensity (FWHM), θ is the Bragg angle.

II. XPS [88]

XPS is used for surface analysis by irradiating a sample with monoenergetic soft X-rays (usually Mg Kα or Al Kα) and analysing the energy of the detected electrons. This technique has a penetrating depth in a solid on the order of 1-10 μm. The photons interact with atoms in the surface region, causing electrons to be emitted by photoelectric effect. The emitted electrons have measured kinetic energies given by:

$$KE = h\nu - BE - \phi_s$$

Equation 63

Where $h\nu$ is the energy of the photon, BE is the binding energy of the atomic orbital from which the electron originates, and ϕ_s is the spectrometer work function, in Koopmans' approximation.

After the electrons are emitted, there is a variety of possible final states of the ions from each type of atom, and so there is a corresponding variety of kinetic energies.

The p, d and f levels are splitted due to spin-orbit interaction: they form a doublet, which refers to the different energy levels ($d_{3/2}$ and $d_{5/2}$, for d orbital) . The spin-orbit splitting ratio is 1:2 for p levels, 2:3 for d levels and 3:4 for f levels.

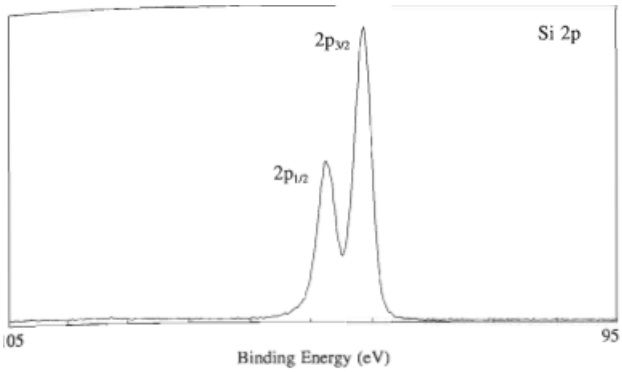

Figure 0.2: Spectrum of Si 2p[88]

Because each element has a unique set of binding energies, XPS can be used to identify and determine the concentration of the elements on the surface. Variations in the elemental binding energies (the chemical shifts) arise from differences in the chemical potential and polarizability of compounds. This chemical shift can be used to identify the chemical state of the materials being analysed.

III. EDX [89]

Energy dispersive X-ray spectroscopy (EDX) is an advanced microanalytical technique often coupled with the SEM instrument. It provides both quantitative and qualitative information on the elements present on the sample surface. In other words, elemental analysis and chemical configuration can be determined using EDX.

Primary beam electrons interact with atoms of the sample in different ways. One of the possible pathways is the ionization of atom and the formation of a core-shell hole (photoelectron). This electron vacancy is subsequently filled from an outer shell electron and the energy difference can be used by another electron to escape the atom (Auger electron). This energy can cause the emission of characteristic X-rays, which are named according to the shell where the hole was generated (the inner shell is K, the L, M, ..) and the shell where the electron that fills the hole comes from (α from the next shell, $\beta$from the after next shell, etc..).

Each element has a unique atomic structure, so a unique set of peaks on its electromagnetic emission spectrum (EDX spectrum), for this reason, it is an interesting technique to use for qualitative analysis; unlike XPS, EDX cannot give information on the oxidation state of the elements.

It can be used for quantitative analysis, measuring the intensities of the peaks and relating them to the concentration of the specific element.

The depth penetration of EDX depends on the energy of the electron beam, but working with a high energy electron beam, ~10-20 keV, it is approximately 2 μm (to be compared with the escape depth of the photoelectrons that is lower than 10 nm).

As following, the EDX spectra of SFM 1:1 is reported.

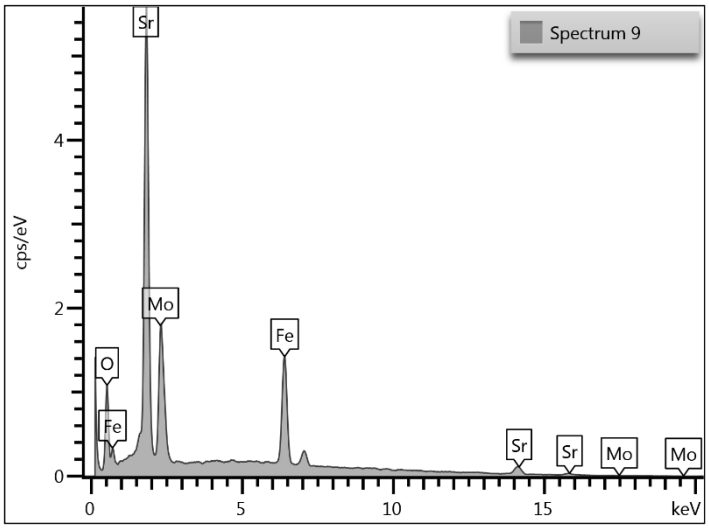

Figure 0.3: EDX graph of SFM 1:1 powder

IV. Porosity analyses [90,91]

In order to characterize the textural parameters of the samples, such as the Specific Surface Area (SSA) and Pore Size Distribution (PSD), gas adsorption analyses using nitrogen were performed, to obtain the adsorption and desorption isotherms.

The SSA was determined by employing the BET model, while the PSD was obtained using the BJH method.

During the analysis, the instrument doses a specific amount of gas inside the tube containing the sample to reach a predefined pressure, then it waits until equilibrium is reached, and finally, the amount of gas adsorbed by the sample is measured. The sample was covered with N_2 molecules in different steps, comprising the adsorption of molecules on the surface, formation of a monolayer (corresponding to the whole surface covered by a single layer of gas molecules), onset of multilayer coverage and consequent filling of the sample pores by capillary condensation.

This was done consecutively up until close to saturation pressure is reached, corresponding to relative pressure p/p^0 =0.995.

BET model [90] is used to determinate the surface area. It assumes:

- Gas molecules will physically adsorb on a solid in layers infinitely
- Gas molecules only interact with adjacent layers
- The theory can be applied to each layer

BET theory extends the Langmuir theory, which concerns only monolayers adsorption and its assumptions are: all surface sites have the same adsorption energy, adsorbates form a monolayer, and each active site can be occupied only by one particle. [91]

The BET equation is reported as follows:

$$\frac{1}{X[(P_0/P)-1]} = \frac{1}{X_m C} + \frac{C-1}{X_m C}\left(\frac{P}{P_0}\right)$$

Equation 64

A linear plot of $\frac{1}{X[\left(\frac{P_0}{P}\right)-1]}$ vs $\frac{P}{P_0}$ is traced and from the slope and the intercept, the surface area (SA) is calculated[90]:

$$SA = \frac{1}{slope + intercept} CSA$$

Equation 65

Where CSA is the cross-sectional area of the adsorbate.

The BJH model is used to calculate the pore size distribution. Once all the pores are filled, the desorption takes place and from the volume desorbed in a determined step, which is related to the pore volume, it is possible to calculate the pore radius. Moreover, the Kelvin equation it is used to estimate the average diameter of the pore and provide a pore size distribution graph.

$$\ln \frac{p}{p_{\text{sat}}} = \frac{2\gamma V_{\text{m}}}{rRT}$$

Equation 66

V. EIS [77,92]

Electrochemical impedance spectroscopy (EIS) offers kinetic and mechanistic data of various electrochemical systems and is widely used. EIS is based on the perturbation of an electrochemical system in equilibrium or steady state, via the application of a sinusoidal signal (AC voltage or current) over a wide range of frequencies and what is registered is the sinusoidal response of the system. Despite this technique being influenced by other cell components and designs, e.g. anode or cathode design, and electrolyte thickness, they are considered as the only reliable measurements applied to compare the performance of electrode materials.

After the analysis of the measurements was carried out through circuit modelling software, a value of an electrical resistance, which is the ability of a circuit element to resist the flow of electrical current, is obtained. However, it is not the so-called resistance.

Ohm's law defines resistance as the ratio between the voltage (V) and the current (I).

$$R = \frac{V}{I}$$

Equation 67

But this can be used only for one circuit element (i.e. the ideal resistor). However, real materials and devices, exhibit much more complex behaviour. Consequently, it becomes essential to move beyond the simplistic concept of resistors and adopt a more comprehensive circuit parameter: impedance.

In impedance measurements, a sinusoidal alternating current potential is applied, resulting in a sinusoid answer at the same frequency but shifted in phase. The excitation signal needs to be small to ensure a pseudo-linear cell response.

The excitation signal has the form:

$$E_t = E_0 \sin(\omega t)$$

Equation 68

Where E_t is the potential at time t, E_0 is the amplitude of the signal, and ω is the radial frequency (in rad/s).

The relationship between ω and f (in Hz) is:

$$\omega = 2\pi f$$

Equation 69

In a linear system, the response signal is shifted in phase (φ):

$$I_t = I_0 \sin(\omega t + \varphi)$$

Equation 70

In this contest, impedance (Z), acting as a resistance, can be expressed with ad analogous to Ohm's law:

$$Z = \frac{E_t}{I_t} = \frac{E_0 \sin(\omega t)}{I_0 \sin(\omega t + \varphi)} = Z_0 \frac{\sin(\omega t)}{\sin(\omega t + \varphi)}$$

Equation 71

Where Z_0 is the magnitude.

The impedance is expressed as a complex function, using the Euler's relationship (*Eq. 71*) to rewrite the potential and the current response as:

$$\exp(j\varphi) = \cos\varphi + j\sin\varphi$$

Equation 72

$$E_t = E_0 \exp(j\omega t)$$

Equation 73

$$I_t = I_0 \exp(j\omega t - \varphi)$$

Equation 74

$$Z = \frac{E}{I} = Z_0 \exp(j\varphi) = Z_0(\cos\varphi + j\sin\varphi)$$

Equation 75

From the last Equation, the expression of Z is composed of a real and an imaginary part. The Nyquist plot is used for analysing the impedance, plotting on the x-axis the real part and the imaginary part on the y-axis.

In this plot the y-axis is negative and each point on the Nyquist plot is the impedance at one frequency.

$$Z_{real} = Z_0 \cos(\varphi)$$

Equation 76

$$Z_{imaginary} = j \cdot Z_0 \sin(\varphi)$$

Equation 77

A facsimile graph of the Nyquist plot is reported in *Figure 0.3*. Note that low frequency data are on the right side of the plot and higher frequencies are on the left.

EIS plots several semicircles and from analysis through ZView software, it is possible to estimate the value of the ohmic and polarisation resistance, respectively the intercept of the curve with x-axis (R_Ω ,in *Figure 0.3*) and the difference in x values of the semicircle plotted with Nyquist plot (R_T ,in *Figure 0.3*).

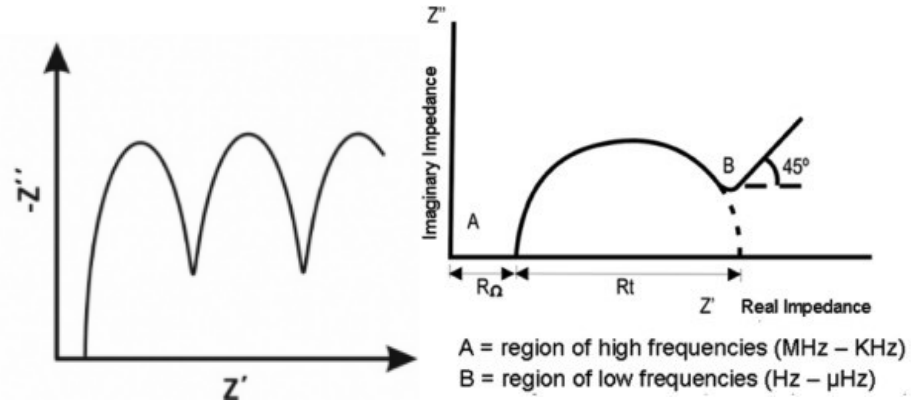

Figure 0.4: Nyquist plot, on the right the resistances and the frequencies are explicated [77,92]

BIBLIOGRAPHY

1. Ebbesen, S. D., Jensen, S. H., Hauch, A. & Mogensen, M. B. High temperature electrolysis in alkaline cells, solid proton conducting cells, and solid oxide cells. *Chemical Reviews* vol. 114 10697–10734 Preprint at https://doi.org/10.1021/cr5000865 (2014).
2. EPA. Greenhouse Gases. *https://www.epa.gov/report-environment/greenhouse-gases#importance*.
3. Shukla & Skea. *Climate Change 2022 Mitigation of Climate Change*. (2022).
4. Ruiz-Morales, J. C., Marrero-López, D., Canales-Vázquez, J. & Irvine, J. T. S. Symmetric and reversible solid oxide fuel cells. *RSC Advances* vol. 1 1403–1414 Preprint at https://doi.org/10.1039/c1ra00284h (2011).
5. Jiang, S. P. Challenges in the development of reversible solid oxide cell technologies: A mini review. *Asia-Pacific Journal of Chemical Engineering* vol. 11 386–391 Preprint at https://doi.org/10.1002/apj.1987 (2016).
6. Mogensen, M. B. *et al.* Reversible solid-oxide cells for clean and sustainable energy. *Clean Energy* vol. 3 175–201 Preprint at https://doi.org/10.1093/ce/zkz023 (2019).
7. United Nations. The Sustainable Development Goals Report. (2023).
8. Renewable Energy Agency, I. *Decarbonising Hard-to-Abate Sectors with Renewables: Perspectives for the G7*. (2024).
9. O'Hayre. Fuel cells for electrochemical energy conversion. *The European Physical Journal Conferences* (2017).
10. Hart, Jones & Cordobes. *The Fuel Cell Industry Review*. (2022).
11. Albarrak, Alshareef, Alshareef & Nahhas. *Review of Hydrogen Based Fuel Cells Energy Storage Systems*. (2022).
12. Ellis, M. W., Von Spakovsky, M. R. & Nelson, D. J. Fuel cell systems: efficient, flexible energy conversion for the 21st century. *IEEE* **89**, (2001).
13. Neergat, M. & Shukla, A. K. A high-performance phosphoric acid fuel cell. *J Power Sources* **102, 317–321**, (2001).
14. Kirubakaran, A., Jain, S. & Nema, R. K. A review on fuel cell technologies and power electronic interface. *Renewable and Sustainable Energy Reviews* **13, 2430–2440**, (2009).
15. Larminie & Dicks, A. Fuel cell systems explained. *J. Wiley* (2003).
16. *Fuel Cell Market Size, Share & Industry Analysis, By Type (Proton Exchange Membrane Fuel Cell, Solid Oxide Fuel Cell, Phosphoric Acid Fuel Cell, and Others), By Application (Transport, Stationary, and Portable), and Regional Forecast, 2024-2032 Source: Https://Www.Fortunebusinessinsights.Com/Industry-Reports/Fuel-Cell-Market-100733*. (2024).
17. H. Shi, C. Su, R. Ran, J. Cao & Z. Shao. Electrolyte materials for intermediate-temperature solid oxide fuel cells . *Progress in Natural Science: Materials International* **30, 764–774**, (2020).
18. O'Hayre, R. P. ., Cha, S.-Won., Colella, W. G. . & Prinz, F. B. . *Fuel Cell Fundamentals*. (John Wiley & Sons Inc., 2016).

19. Dwivedi, S. Solid oxide fuel cell: Materials for anode, cathode and electrolyte. *Int J Hydrogen Energy* **45**, 23988–24013 (2020).
20. Jacobson, A. J. Materials for solid oxide fuel cells. *Chemistry of Materials* vol. 22 660–674 Preprint at https://doi.org/10.1021/cm902640j (2010).
21. Raza, M. Oxygen vacancy stabilized zirconia (OVSZ); synthesis and properties.
22. Morales, M., Roa, J. J., Tartaj, J. & Segarra, M. A review of doped lanthanum gallates as electrolytes for intermediate temperature solid oxides fuel cells: From materials processing to electrical and thermo-mechanical properties. *Journal of the European Ceramic Society* vol. 36 1–16 Preprint at https://doi.org/10.1016/j.jeurceramsoc.2015.09.025 (2016).
23. Cavaliere, P. *Water Electrolysis for Hydrogen Production*. *Water Electrolysis for Hydrogen Production* (Springer International Publishing, 2023). doi:10.1007/978-3-031-37780-8.
24. Consiglio Nazionale Ingegneri. Introduzione alla produzione e metodi di impiego di idrogeno rinnovabile. in (2022).
25. IRENA. Hydrogen. (2022).
26. Atlas Copco. Your guide to electrolyzers for hydrogen production. *https://www.atlascopco.com/en-uk/compressors/wiki/compressed-air-articles/electrolyzers-as-hydrogen-production-technologies*.
27. Lin, J., Zhang, Y., Xu, P. & Chen, L. CO2 electrolysis: Advances and challenges in electrocatalyst engineering and reactor design. *Materials Reports: Energy* vol. 3 Preprint at https://doi.org/10.1016/j.matre.2023.100194 (2023).
28. Harrison, K. W., Remick, R. & Martin, G. D. Hydrogen Production: Fundamentals and Cas Study Summaries . *National Renewable Energy Laboratory* (2010).
29. Trattner, A., Höglinger, M., Macherhammer, M. G. & Sartory, M. Renewable Hydrogen: Modular Concepts from Production over Storage to the Consumer. *Chem Ing Tech* **93**, 706–716 (2021).
30. CEEW. Types of Electrolysers. *https://www.ceew.in/cef/quick-reads/explains/types-of-electrolysers*.
31. Allied Market Research. *Electrolyzer Market Size, Share, Competitive Landscape and Trend Analysis Report, by Application, by Capacity, by Product : Global Opportunity Analysis and Industry*. (2023).
32. Liu, Y., Zhou, F., Chen, X., Wang, C. & Zhong, S. Enhanced electrochemical activity and stability of LSCF cathodes by Mo doping for intermediate temperature solid oxide fuel cells. *J Appl Electrochem* (2021).
33. Liang, J. *et al.* The development of solid oxide co-electrolysis of H 2 O and CO 2 on large-size cells and stacks . *iEnergy* **2**, 109–118 (2023).
34. Shen, M., Ai, F., Ma, H., Xu, H. & Zhang, Y. Progress and prospects of reversible solid oxide fuel cell materials. (2021) doi:10.1016/j.isci.
35. Zhang, X., Song, Y., Wang, G. & Bao, X. Co-electrolysis of CO2 and H2O in high-temperature solid oxide electrolysis cells: Recent advance in cathodes. *Journal of*

Energy Chemistry vol. 26 839–853 Preprint at https://doi.org/10.1016/j.jechem.2017.07.003 (2017).
36. European Commission. COMMUNICATION FROM THE COMMISSION TO THE EUROPEAN PARLIAMENT, THE COUNCIL, THE EUROPEAN ECONOMIC AND SOCIAL COMMITTEE AND THE COMMITTEE OF THE REGIONS. (2020).
37. European Environment Agency. Greenhouse gas emissions from energy use in buildings in Europe. *https://www.eea.europa.eu/en/analysis/indicators/greenhouse-gas-emissions-from-energy* (2024).
38. Gao, J., Choo Sze Shiong, S. & Liu, Y. Reduction of CO2 to chemicals and Fuels: Thermocatalysis versus electrocatalysis. *Chemical Engineering Journal* vol. 472 Preprint at https://doi.org/10.1016/j.cej.2023.145033 (2023).
39. Viswanathan, B. & Narayanan, H. *PEROVSKITE MATERIALS-AN INTRODUCTION*. https://www.researchgate.net/publication/370100194 (2023).
40. Rehman, Wang & Yu. Electronic, Magnetic and Optical Properties of Double Perovskite Compounds: A First Principle Approach. *Crystals (Basel)* **12(11), 1597**, (2022).
41. Das, R. & Choudhary, R. N. P. Structural and electrical characteristics of double perovskite: Nd2CoMnO6. *Mater Chem Phys* **311**, (2024).
42. Skutina, L., Filonova, E., Medvedev, D. & Maignan, A. Undoped Sr2MMoO6 double perovskite molybdates (M = Ni, Mg, Fe) as promising anode materials for solid oxide fuel cells. *Materials* vol. 14 Preprint at https://doi.org/10.3390/ma14071715 (2021).
43. Kumar, D., Sagar Yadav, R., Kumar Singh, A. & Bahadur Rai, S. Synthesis Techniques and Applications of Perovskite Materials. *Intrechopen* (2020).
44. Olav, T., Sunde, L., Grande, T. & Einarsrud, M.-A. *Modified Pechini Synthesis of Oxide Powders and Thin Films*.
45. D. A. Osinkin, E. V. Zabolotskaya, D. G. Kellerman & A. Yu. Suntsov. The physical properties and electrochemical performance of Ca-doped Sr2MgMoO6-δ as perspective anode for solid oxide fuel cells. *J Solid State Electrochem* **22, 1209–1215**, (2018).
46. Y.-H. Huang, R. I. Dass, J. C. Denyszyn & J. B. Goodenough. Synthesis and Characterization of Sr2MgMoO6−δ. *J. Electrochem. Soc.* **153, A1266**, (2006).
47. Y.-H. Huang, R. I. Dass, Z.-L. Xing & J. B. Goodenough. Double Perovskites as Anode Materials for Solid-Oxide Fuel Cells,. *Science (1979)* **312, 254–257**, (2006).
48. S. Vasala, H. Yamauchi & M. Karppinen. Role of SrMoO4 in Sr2MgMoO6 synthesis. *J Solid State Chem* **184, 1312–1317**, (2011).
49. Wright, J. H., Virkar, A. V., Liu, Q. & Chen, F. Electrical characterization and water sensitivity of Sr2Fe 1.5Mo0.5O6-δ as a possible solid oxide fuel cell electrode. *J Power Sources* **237**, 13–18 (2013).
50. Yatoo, M. A. & Skinner, S. J. Ruddlesden-Popper phase materials for solid oxide fuel cell cathodes: A short review. *Mater Today Proc* **56**, 3747–3754 (2022).

51. Lee, D. & Lee, H. N. Controlling oxygen mobility in ruddlesden-popper oxides. *Materials* vol. 10 Preprint at https://doi.org/10.3390/ma10040368 (2017).
52. Suchaneck, G. & Artiukh, E. Nonstoichiometric Strontium Ferromolybdate as an Electrode Material for Solid Oxide Fuel Cells. *Inorganics* vol. 10 Preprint at https://doi.org/10.3390/inorganics10120230 (2022).
53. Kim, J., Ferree, M., Gunduz, S., Co, A. C. & Ozkan, U. S. Sr2Fe2–XMoXO6 double perovskites as electrocatalysts for oxidative dehydrogenation of ethane: Effect of B-site stoichiometry. *Electrochim Acta* **461**, (2023).
54. Zhang, S., Zhu, K., Hu, X., Peng, R. & Xia, C. Antimony doping to greatly enhance the electrocatalytic performance of Sr2Fe1.5Mo0.5O6−δperovskite as a ceramic anode for solid oxide fuel cells. *J Mater Chem A Mater* **9**, 24336–24347 (2021).
55. Liu, Q., Yang, C., Dong, X. & Chen, F. Perovskite Sr2Fe1.5Mo0.5O 6-δ as electrode materials for symmetrical solid oxide electrolysis cells. *Int J Hydrogen Energy* **35**, 10039–10044 (2010).
56. Li, H., Zhao, Y., Wang, Y. & Li, Y. Sr2Fe2-xMoxO6-δ perovskite as an anode in a solid oxide fuel cell: Effect of the substitution ratio. *Catal Today* **259**, 417–422 (2016).
57. Cernea, M. *et al.* Preparation by sol-gel and solid state reaction methods and properties investigation of double perovskite Sr2FeMoO6. *J Eur Ceram Soc* **33**, 2483–2490 (2013).
58. Angervo, I., Saloaro, M., Granroth, S., Huhtinen, H. & Paturi, P. Refined Sr2FeMoO6 interface realized with photoemission and magnetization analysis. *Appl Surf Sci* **507**, (2020).
59. Raekers, M. *et al. Investigation of Chemical and Grain Boundary Effects in Highly Ordered Sr 2 FeMoO 6 : XPS and Mössbauer Studies*. *JOURNAL OF OPTOELECTRONICS AND ADVANCED MATERIALS* vol. 8 (2006).
60. Choi, J. & Thompson, L. *XPS Study of As-Prepared and Reduced Molybdenum Oxides*. *Applied Surface Science* vol. 93 (1996).
61. NIST XPS Database (SRD20), Version 5.0.
62. Thommes, M. *et al.* Physisorption of gases, with special reference to the evaluation of surface area and pore size distribution (IUPAC Technical Report). *Pure and Applied Chemistry* **87**, 1051–1069 (2015).
63. Wang, Z., Tan, S., Xiong, Y. & Wei, J. Effect of B sites on the catalytic activities for perovskite oxides La.6Sr.4CoxFe1-xO3-δ as metal-air batteries catalysts. *Progress in Natural Science: Materials International* **28**, 399–407 (2018).
64. Meng, W. *et al.* Selectivity control between reverse water-gas shift and fischer-tropsch synthesis in carbon-supported iron-based catalysts for CO2 hydrogenation. *Chemical Engineering Journal* **489**, (2024).
65. Kharaji, A. G., Shariati, A. & Takassi, M. A. A novel γ-alumina supported fe-mo bimetallic catalyst for reverse water gas shift reaction. *Chin J Chem Eng* **21**, 1007–1014 (2013).

66. Qin, S. *et al.* Fe-Mo interactions and their influence on Fischer-Tropsch synthesis performance. *Appl Catal A Gen* **392**, 118–126 (2011).
67. Østergaard, M. B., Strunck, A. B., Boffa, V. & Jørgensen, M. K. Kinetics of Strontium Carbonate Formation on a Ce-Doped SrFeO3 Perovskite. *Catalysts* **12**, (2022).
68. Alyousef & K. Kendall. Characterization of the electrochemical performance of micro-tubular solid oxide fuel cell (SOFC). *Journal of Taibah University for Science* **2, 14–21**, (2009).
69. Ni, M., Leung, M. K. H. & Leung, D. Y. C. Technological development of hydrogen production by solid oxide electrolyzer cell (SOEC). *International Journal of Hydrogen Energy* vol. 33 2337–2354 Preprint at https://doi.org/10.1016/j.ijhydene.2008.02.048 (2008).
70. Stambouli. Solid oxide fuel cells (SOFCs): a review of an environmentally clean and efficient source of energy. *Renewable and Sustainable Energy Reviews* **6**, (2022).
71. Marrero-López, D. *et al.* Redox behaviour, chemical compatibility and electrochemical performance of Sr2MgMoO6 - δ as SOFC anode. *Solid State Ion* **180**, 1672–1682 (2010).
72. Dos Santos-Gómez, L., León-Reina, L., Porras-Vázquez, J. M., Losilla, E. R. & Marrero-López, D. Chemical stability and compatibility of double perovskite anode materials for SOFCs. *Solid State Ion* **239**, 1–7 (2013).
73. Alvarado-Flores, J. J. *et al.* Synthesis, characterization and kinetic study of the Sr2FeMoO6-δ double perovskite: New findings on the calcination of one of its precursors. *Int J Hydrogen Energy* **46**, 26185–26196 (2021).
74. Qiao, J. *et al.* The Ca element effect on the enhancement performance of Sr2Fe1.5Mo0.5O6−δ perovskite as cathode for intermediate-temperature solid oxide fuel cells. *J Power Sources* **331**, 400–407 (2016).
75. Li, J. *et al.* Diffusion behavior and electrical performance of La2O3 doped Ni-Co films and their application as metallic interconnection of solid oxide fuel cell. *Thin Solid Films* **768**, (2023).
76. Wang, Y. *et al.* Morphology and performance evolution of anode microstructure in solid oxide fuel cell: A model-based quantitative analysis. *Applications in Energy and Combustion Science* **5**, (2021).
77. Lazanas, A. C. & Prodromidis, M. I. Electrochemical Impedance Spectroscopy—A Tutorial. *ACS Measurement Science Au* vol. 3 162–193 Preprint at https://doi.org/10.1021/acsmeasuresciau.2c00070 (2023).
78. Stijepovic, I., Darbandi, A. J. & Srdic, V. V. Conductivity of Co and Ni doped lanthanum-gallate synthesized by citrate sol-gel method. *Ceram Int* **39**, 1495–1502 (2013).
79. Gebregergis, A., Pillay, P., Bhattacharyya, D. & Rengaswemy, R. Solid Oxide Fuel Cell Modeling. *IEEE Transactions on Industrial Electronics* **56**, 139–148 (2009).
80. Hauch, A., Jensen, S. H., Ramousse, S. & Mogensen, M. Performance and Durability of Solid Oxide Electrolysis Cells. *J Electrochem Soc* **153**, A1741 (2006).

81. Guo, Y. *et al.* Characterization of Sr 2 Fe 1.5 Mo 0.5 O 6-δ -Gd 0.1 Ce 0.9 O 1.95 symmetrical electrode for reversible solid oxide cells. *Ceram Int* **45**, 10969–10975 (2019).
82. Brisse, A., Schefold, J. & Zahid, M. High temperature water electrolysis in solid oxide cells. *Int J Hydrogen Energy* **33**, 5375–5382 (2008).
83. Löper, P. *et al.* Analysis of the temperature dependence of the open-circuit voltage. in *Energy Procedia* vol. 27 135–142 (Elsevier Ltd, 2012).
84. Huang, J., Wei, H., Wei, T. & Lee, Y. CO2 conversion improvement of solid-oxide electrolysis cells by inserting buffer layers between MFe2O4 (M = Ni, Cu, Co, Fe) cathode and electrolyte. *Journal of CO2 Utilization* **77**, (2023).
85. Mei, J., Liao, T. & Sun, Z. Metal exsolution engineering on perovskites for electrocatalysis: a perspective. *Mater Today Energy* **31**, (2023).
86. Perednis, D. & Gauckler, L. J. Solid oxide fuel cells with electrolytes prepared via spray pyrolysis. *Solid State Ion* **166**, 229–239 (2004).
87. Role of Bragg's law in X-Ray Diffraction studies. *https://xrd.co/role-braggs-law-x-ray-diffraction-studies/*.
88. Moulder, Stickle, Sobol & Bomben. *Handbook of X-Ray Photoelectron Spectroscopy*. (1992).
89. Bernardi, J. Energy-dispersive X-ray spectroscopy. in *Imaging Modalities for Biological and Preclinical Research: A Compendium, Volume 1: Part I: Ex vivo biological imaging* (IOP Publishing, 2021). doi:10.1088/978-0-7503-3059-6ch41.
90. Anton Paar. BET Theory. *https://wiki.anton-paar.com/it-it/teoria-bet/*.
91. Pavan & Barron. BET Surface Area Analysis of Nanoparticles. *https://chem.libretexts.org/Bookshelves/Analytical_Chemistry/Physical_Methods_in_Chemistry_and_Nano_Science_(Barron)/02%3A_Physical_and_Thermal_Analysis/2.03%3A_BET_Surface_Area_Analysis_of_Nanoparticles*.
92. Gamty Instruments. Basics of Electrochemical Impedance Spectroscopy. *https://www.gamry.com/application-notes/EIS/basics-of-electrochemical-impedance-spectroscopy/*.
93. TopTitechs. What is the Solid Oxide Fuel Cell (SOFC)?
94. Sk. Anirban, Tanmoy Paula & Abhigyan Dutta. Vacancy mediated ionic conduction in Dy substituted nanoceria: a structure–property correlation study. *RSC Adv* **5, 50186–50195**, (2015).
95. Rizwan, M., Khadija, A. & Zeba, I. First-principles investigation of structural modification, fine band gap engineering, and optical response of La1−xBaxGaO3 for optoelectronic applications. *Applied Physics* (2020).
96. Louis H. Perovskite photovoltaic nanostructured materials: device architectural design, challenges and recent progress. *Asian Journal of Green Chemistry 3* **3**, 125–287 (2018).
97. MICROLED-info. Perovskites: Illuminating the Path for Next-Gen MicroLED Displays. *https://www.microled-info.com/perovskites-illuminating-path-next-gen-microled-displays*.

98. An introduction to Perovskites. *https://www.perovskite-info.com/introduction* (2023).
99. Banerjee, Awashti, Maji & Pal. Double Perovskite Oxides Bringing a Revelation in Oxygen Evolution Reaction Electrocatalyst Design. *ChemElectroChem* **10(4)**, (2023).
100. Bove & Ubertini. Modeling solid oxide fuel cell operation: Approaches, techniques and results. *J Power Sources* **159**, (2006).
101. Ahmed, K. I. & Ahmed, M. H. Developing a Novel Design for a Tubular Solid Oxide Fuel Cell Current Collector. *Appl. Sci.* **12, 6003**, (2022).
102. D. Chen, H. He, D. Zhang, W. Hanzhi & M. Ni. Percolation Theory in Solid Oxide Fuel Cell Composite Electrodes with a Mixed Electronic and Ionic Conductor. *Energies (Basel)* **6, 1632–1656**, (2013).
103. Wolf, S. E. *et al.* Solid oxide electrolysis cells - current material development and industrial application. *Journal of Materials Chemistry A* vol. 11 17977–18028 Preprint at https://doi.org/10.1039/d3ta02161k (2023).